

Development of a Process for Converting Radiographic Images of metal into Finite Element Models: Assessing Accuracy and Validity

By

Ashish Ghanghash

Master's Thesis - STEM9100A

Submitted to Flinders University

for the degree of

MEMC Master of Engineering (Mechanical)

College of Science and Engineering

20th October 2023

TABLE OF CONTENTS

TABLE OF CONTENTS	I
ABSTRACT	III
DECLARATION	V
ACKNOWLEDGEMENTS	VI
LIST OF FIGURES	VIII
1. INTRODUCTION	1
1.1 Aim of the research.....	3
1.2 Scope of the research.....	4
1.3 Outline of the research.....	4
2. LITRATURE REVIEW	6
2.1 X-ray Technology.....	6
2.2 Radiographic Technology	7
2.3 Finite Element Models	7
2.4 FEM using Computerized Tomography.....	8
2.4.1 Diffusion of Chlorine in Concrete	8
2.4.2 Mechanical Behaviour of Asphalt Mixture	8
2.4.3 Non-Crimp Fabric-Based Fiber Composites.....	9
2.4.4 X-ray CT scan-Based Finite Element Modelling of Composites	9
2.4.5 Aluminium Foams	9
2.4.6 Glass Scaffolds.....	9
2.4.7 Wood Planks	10
2.4.8 Knee Joints.....	10
2.5 Research gaps.....	10
3. METHODOLOGY	11
3.1 Theory	11
3.2 Specimen Design.....	11
3.2.1 Notched specimen	12
3.2.2 Welded specimen	12
3.2.3 Middle cut slit specimen.....	13
3.2.4 Artificial corrosion specimen	13
3.3 Surface treatments	13
4. X-RAY EXTRACTION	15
4.1 Theory	15
4.2 Radiographic Imaging Process	16
4.3 Geometry Extraction from X-Ray image Code	17
4.4 Results	20
4.5 Discussion	22

4.6	Summary	22
5.	FINITE ELEMENT MODELLING	24
5.1	Finite Element Modelling Process (importing Geometry).....	24
5.2	Shell-Solid Comparison (Mesh Study)	26
5.3	X-Ray shell modelling	27
5.4	Summary	28
6.	DIC MEASUREMENTS	29
6.1	Process (Tensile test)	29
6.2	Results	31
6.3	Comparison	31
6.3.1	Results comparison and processing code MATLAB.....	31
6.4	Discussion	32
7.	CONCLUSION.....	34
8.	FUTURE WORK.....	36
	BIBLIOGRAPHY	37
	APPENDICES	42
A.	RESULTS: Geometry extraction from the radiographic images	42
1.	Notched Specimen	42
2.	Corrosion Specimen	44
3.	Welded Specimen.....	45
4.	Middle Cut Specimen.....	46
B.	Results Comparison plots [MATLAB Script].....	47
1.	Corrosion Specimen	47
2.	Notched Specimen	48
C.	Risk Assessment.....	1
D.	MATLAB Codes.....	1
1.	Extract pixel RGB Values.....	1
2.	Mesh Study.....	1
3.	X-ray thickness extraction	3
4.	Results Comparison.....	11
E.	Specimens Details & Engineering Drawings.....	1

ABSTRACT

The objective of this research is to develop a process that converts radiographic images into finite element models (2D) by extracting geometry data from radiographic image. The ultimate purpose of this research is to elevate radiographic imaging to a new level by enabling the assessment of structural integrity through the creation of finite element models based on x-ray images, followed by the performance of tests on these models to verify their structural integrity.

Additionally, a literature review was conducted, revealing that metals are the least utilized materials in the fabrication of a Finite Element Model (FEM). To further investigate this, four specimens with varying surface characteristics were meticulously crafted. The initial stage of this process entails conducting an X-ray analysis of the specimens. Subsequently, a MATLAB code is developed to extract the geometry data from the x-ray image, which is then imported into the finite element model using Ansys Workbench software. The results obtained from this research indicate the presence of minor errors in the extraction of specimen geometry. These errors stem from the non-uniform absorption of x-rays, primarily due to beam hardening. As a consequence, the edges of the specimen appear brighter in the x-ray image. Following the creation of the finite element model, tensile testing is conducted on the specimen within Ansys and using Instron. The resulting strain values are then compared to validate the accuracy of the process. Given that this process is relatively new, there are opportunities for improvement. One potential avenue for enhancement involves utilizing x-ray intensity values instead of absorption values, as this has the potential to enhance the overall accuracy of the process.

Despite these minor limitations, the developed process offers several advantages. Notably, it is a fast and efficient method that does not require significant computational power. Moreover, it demonstrates promising potential for success in the future. In light of these findings, further research could focus on refining the process and exploring additional applications for this innovative method.


In conclusion, this research successfully develops a process for converting radiographic images into finite element models by extracting geometry data from x-ray contrast. The process is verified through tensile testing on specimens. Although minor errors are present in the extraction of specimen geometry, the process shows potential for improvement, such as utilizing x-ray intensity values. Overall, this process offers speed, efficiency, and

promising possibilities for future success. Further research can build upon these findings to enhance the process and explore its wider applications.

DECLARATION

I certify that this thesis:

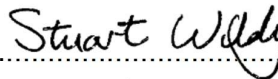
1. does not incorporate without acknowledgment any material previously submitted for a degree or diploma in any university
2. and the research within will not be submitted for any other future degree or diploma without the permission of Flinders University; and
3. to the best of my knowledge and belief, does not contain any material previously published or written by another person except where due reference is made in the text.

Signature of student:

Print name of student: Ashish Ghanghash

Date: 20th October 2023

I certify that I have read this thesis. In my opinion it is/is not (please circle) fully adequate, in scope and in quality, as a thesis for the degree of <Degree Name>. Furthermore, I confirm that I have provided feedback on this thesis and the student has implemented it minimally/partially/fully (please circle).

Signature of Principal Supervisor:

Print name of Principal Supervisor: Dr. Stuart Wildy

Date: 20th October 2023

ACKNOWLEDGEMENTS

I would like to take this opportunity to express my profound gratitude to the individuals who have provided unwavering support and invaluable guidance throughout the entire process of completing this thesis. Their contributions have been instrumental in shaping the outcome of this research work, and for that, I am sincerely appreciative.

First and foremost, I would like to extend my heartfelt thanks to my esteemed supervisor, Dr. Stuart Wildy, whose expertise, and constructive feedback have played a pivotal role in the development and execution of this study. His unwavering support and encouragement have been crucial in navigating the challenges and complexities that arose during this research journey.

Additionally, I am deeply grateful for the mentorship and support of Dr. John Codrington, Mr. Michael Russo, and Mr. Tim Hodge. Their guidance and involvement have been invaluable in my academic growth and have provided me with the necessary tools and knowledge to successfully complete this thesis. Their dedication and commitment to my development as a researcher has been truly commendable.

I would also like to acknowledge the support and camaraderie of my colleagues and friends. The discussions and interactions with them have greatly contributed to my growth as a professional and have provided me with different perspectives and insights. Their presence and involvement have been an invaluable source of inspiration and motivation throughout this journey.

Furthermore, I am deeply grateful to my family for their unwavering love, belief in my abilities, and constant encouragement. Their support has been a constant source of strength and motivation, and I am forever indebted to them for their unwavering belief in my potential.

Lastly, I would like to express my appreciation for the work of authors, researchers, and scholars whose contributions have expanded the boundaries of knowledge in this field. Their dedication and commitment to their respective fields have laid the groundwork for the successful completion of this thesis. I am truly grateful for their involvement and belief in the importance of advancing knowledge in this area.

In conclusion, I am immensely grateful for the involvement and belief of all those mentioned above. Their support, guidance, and encouragement have been pivotal in achieving this significant milestone in my academic journey.

LIST OF FIGURES

Figure 1 Notched dogbone specimen with radius 225mm (up) and notched dimensions (down)....	12
Figure 2 Artificially corroded specimen with uneven shape (side view and front view)	13
Figure 3 The surfaces of all four prepared specimens are in their original condition prior to testing.	14
Figure 4 The captured x-ray images viewed using Sonic DiacomViewer: (a). Slit and notched specimen with supports. (b). Welded and artificially corroded specimen with supports. (c). Slit and notched specimen without any support. (d). Artificial corrosion and welded specimen without any support.....	17
Figure 5 Extracted pixel values in RGB form of the middle cut specimen.....	17
Figure 6 As part of the thickness extraction process, the X-ray image is rectified and a plot is generated to visualize the contrast values.....	18
Figure 7 Extracted targeting section of the x-ray image and centre line in red (left) with the geometry data (right) along the centre line [x-z axis]	19
Figure 8 The extracted data from the notched specimen geometry includes three plots. (a) Surface thickness plot, (b) Line thickness plot, (c) Thickness error plot.....	21
Figure 9 The extracted data from the artificially corroded specimen geometry includes three plots. (a) Surface thickness plot, (b) Line thickness plot, (c) Thickness error plot.	22
Figure 10 The figure illustrates the flow of the shell model and solid model development in Ansys Workbench. It also showcases the integration of an imported shell model with x-ray thickness data.	24
Figure 11 Shell model (FEM 2D) with Mesh in Ansys of artificial corrosion (left) and notched (right) [Ansys Classic]	25
Figure 12 Shell model (FEM 2D) in Ansys of notched normal (left) and X-ray model (right) [Ansys Workbench].....	25
Figure 13 Solid model (FEM 3D) with Mesh in Ansys of artificial corrosion (left) and notched (right)	25
Figure 14 Stress distribution in artificial corrosion (left) and notched (right) specimen [Solid model (FEM 3D)]	26
Figure 15 Shell vs solid model of Notched and artificially corroded specimen shows the secondary bending affect of the solid model.....	26
Figure 16 Mesh study graphs of shell and solid modes with different samples. [notch and corrosion]	27
Figure 17 Shell vs solid model of Notched and artificially corroded specimen.....	28
Figure 18 Tensile testing setup showing a DIC and Instron with their arrangements.....	30
Figure 19 DIC machine results for the notch specimen facing the camera	31
Figure 20 Strain results of notch specimen's comparison of shell, solid and real specimen (x-ray).....	32
Figure 21 Raw X-ray image of a normal and a Nitched dog bone specimen viewed in a Sonic DiacomViewer.....	42
Figure 22 Targeted specimen area (left) and the extracted centreline x-ray contrast data (right).	42

Figure 23 Smoothened contrast values of the x-ray (left) and the relation to the geometry after calculating the geometry (right) 43

Figure 24 Comparison of the extracted geometry with the actual geometry of the specimen 43

Figure 25 The error plot observed after comparing the extracted geometry with the actual geometry (left) and the geometry plot of the specimen (right) 43

Figure 26 Improved geometry values after removing the errors i.e., >6mm 44

Figure 27 Targeted specimen area (left) and the extracted centreline x-ray contrast data (right). 44

Figure 28 Smoothened contrast values of the x-ray (left) and the relation to the geometry after calculating the geometry (right) 44

Figure 29 Geometry distribution (left) compared with the centreline geometry (right) 45

Figure 30 Improved Geometry distribution (left) compared with the centreline geometry (right) 45

Figure 31 Targeted specimen area (left) and the extracted centreline x-ray contrast data (right). 45

Figure 32 Smoothened contrast values of the x-ray 46

Figure 33 Targeted specimen area (left) and the extracted centreline x-ray contrast data (right). 46

Figure 34 Smoothened contrast values of the x-ray 46

Figure 35 Comparison of shell, solid and X-ray finite element models (left) and the strain plot received from DIC machine (right) 47

Figure 36 Z position surface plot (left) and the deformation surface plot (right) 47

Figure 37 Deformation plots 47

Figure 38 W deformation vs Y position plot (left) and Deformation vs position plot of the initial position before and final position after (right) 48

Figure 39 Comparison of shell, solid and X-ray finite element models (left) and the strain plot received from DIC machine (right) 48

Figure 40 Z position surface plot (left) and the deformation surface plot (right) 48

Figure 41 Deformation plots 49

Figure 42 W deformation vs Y position plot (left) and Deformation vs position plot of the initial position before and final position after (right) 49

1. INTRODUCTION

Non-destructive testing (NDT) refers to the utilization of methods that evaluate the structural integrity, surface imperfections, or metallurgical condition of materials without causing harm or compromising their intended use (Dwivedi et al., 2018). It plays a critical role in upholding high standards of product quality and ensuring the dependable operation of components across various industries. By enabling the detection and measurement of defects, stresses, and alterations in the material's microstructure, NDT provides essential insights to designers and maintenance personnel.

Through the application of non-intrusive techniques, NDT facilitates thorough assessment and evaluation of materials without causing any damage. This comprehensive approach to quality assurance and maintenance empowers stakeholders to make well-informed decisions, implement necessary repairs or modifications, and safeguard the overall integrity and lifespan of components in service. The knowledge obtained through NDT findings is invaluable for guiding decisions pertaining to product design and maintenance schedules, ultimately guaranteeing the reliability and performance of the components (Raj, 2001). The NDT method can be characterized by five key factors: the energy source used for probing, the nature of the resulting signals or images, the means of detecting and sensing the signals, the means of indicating and recording the signals, and the basis for interpreting the results (Bossi, 2019).

Radiographic testing is a non-destructive testing method that relies on the attenuation of penetrating radiation by the test object. This radiation can be in the form of electromagnetic waves or particles such as X-rays, gamma rays, and neutrons. Variations in density, thickness, and composition of the test object cause different amounts of radiation to be absorbed. The unattenuated radiation that passes through the object can be detected and monitored using radiation-sensitive film, radiosopic sensors, or computed tomography. Radiographic testing is commonly used in industrial applications to ensure the absence of internal discontinuities in castings and weldments. It can also be applied to forgings and mechanical assemblies, although it is typically limited to testing for conditions and proper component placement. This method is effective in detecting voids, leak paths, inclusions, cracks, corrosion, porosity, missing or incomplete components, lack of fusion, and debris. (Bossi, 2019)

The use of X-ray computed tomography (CT) for non-destructive volumetric analysis of samples has attracted interest from various disciplines. While obtaining CT images has become easier, interpreting these 3D images remains challenging. Manual interpretation by subject matter experts (SMEs) is subjective and prone to errors, and the increasing size of image data and the need to identify smaller features which makes the manual extraction impractical. Computer vision (CV) techniques have been used for automated feature extraction but struggle with image noise. Machine learning (ML) algorithms offer a promising solution but require large amounts of labelled data. (Konnik et al., 2021)

The Finite Element Method (FEM) is widely used in computational tools for Computer Aided Engineering (CAE) and is considered one of the most powerful tools available to engineering professionals and students. By virtually testing product designs, Finite Element Analysis (FEA) allows users to gain a better understanding of their designs and make necessary changes early in the product development process. The increasing adoption of FEA in the design cycle is driven by market pressure, as it offers numerous benefits such as improved product quality, reduced development costs, and shorter time-to-market. FEM can be applied to solve mathematical models for various engineering problems, including stress analysis of structures, dynamic responses of vehicles under different loading conditions, and more. There are numerous applications of FEA across industries such as automotive, aerospace, defence, consumer products, energy, transportation, and construction (Chen et al., 2018). Finite Element Analysis (FEA) is a numerical method used for analysing structures and systems. It involves the use of different element types categorized into 1D, 2D, and 3D. 1D elements are suitable for slender structures, 2D elements for structures with large surface areas, and 3D elements for structures with significant thickness. While 3D elements provide the most accurate representation, they can be computationally expensive (Wai et al., 2013). An analyst must choose the appropriate element type based on the problem, available resources, and desired accuracy level. Combining different element types is common for accurate representation.

In recent years, FEA has also been extended to emerging fields like materials science, biomedical engineering, and geophysics. Several commercial programs have been developed for conducting FEA, with ANSYS® Workbench being a popular and user-friendly platform that seamlessly integrates with ANSYS, Inc.'s suite of advanced engineering simulation technology (Chen et al., 2018). Workbench offers a bidirectional connection to major CAD systems and is designed to improve productivity and ease of use for engineering

teams. It has become an indispensable tool for product development in many companies across diverse engineering fields (Chen).

X-ray and finite element modelling are established and cost-effective methods that have been widely utilized in the field of non-destructive testing (NDT) for several years. These methods have proven to be reliable and have gained significant popularity within the industry. The selection of this research to develop a new method was driven by these reasons.

1.1 Aim of the research

The aim of this research is to develop a method for transferring geometric data from an x-ray image to a 2D finite element model, while also incorporating mechanical properties such as Young's modulus (Nirajkumar Patel, another master's student). This will allow for the creation of an accurate virtual representation FEM of the x-rayed structure, which can then be subjected to tensile testing using a universal testing machine and comparing the strain results with the FEM to verify the process.

To attain the desired outcome, a set of objectives was established. These objectives encompass:

- Designing specimens with diverse surface characteristics for testing purposes.
- Determining the optimal x-ray settings for achieving high-quality imaging of the selected metal (steel A516 grade 70).
- Developing a MATLAB code to accurately extract specimen geometry and save it in a file format compatible with creating a finite element model.
- Creating a 2D or shell model and importing the extracted geometry.
- Conducting tensile testing on the finite element model using Ansys and collecting resulting data.
- Validating the accuracy of the method by performing tensile testing on prepared specimens and measuring strain results using a digital image correlation (DIC) machine.
- Comparing and meticulously analysing the results from both tests, with a specific focus on the strain data.

By achieving these objectives, the research aims to establish a reliable method for transferring geometric data from x-ray images to a finite element model, which can be

utilized for assessing structural integrity. Additionally, this process will prioritize minimizing computational power usage.

1.2 Scope of the research

The existing methods for creating finite element models of built structures are limited and often time-consuming, lacking the necessary standardization (Cordon, 2019). This research focuses specifically on relating the geometry of a structure to a finite element model using radiographic imaging. The determination of mechanical properties and their correlation with the x-ray image is not within the scope of this research, as it will be addressed by my colleague, Nirajkumar Patel, in a separate study.

During the development of this method, four types of surfaces will be investigated: welded, notched, horizontal slit (middle cut 1.8mmx10mm), and an artificial corrosion surface. The parameters considered in this investigation will include extracting the geometry of the specimen and establishing its relationship with the x-ray image. Subsequently, a shell model will be created using the obtained geometry data, followed by conducting tensile testing on the model.

By focusing on these specific objectives, this research aims to provide a more efficient and standardized method for creating finite element models of built structures, specifically by utilizing radiographic imaging to relate the structure's geometry to the model.

If feasible, the structure can be modelled without considering its material properties. The objective is to compare the results with the actual geometry, aiming for a close resemblance. Furthermore, an analysis of the errors between the two compared items will be conducted based on the x-ray absorption values.

1.3 Outline of the research

This thesis primarily focuses on the advancements in creating finite element models using x-ray images. It explores the progress made in x-ray technology, radiographic techniques, and the application of these developments in finite element modelling. The thesis also discusses the utilization of these technologies in various fields and the materials employed in constructing finite element models through x-ray imaging. However, it should be noted that the specific steps involved in creating these models are not extensively covered, as there are alternative approaches beyond the methodology described in this research. The

study identifies gaps in existing research and presents a comprehensive methodology along with corresponding results. A detailed discussion and potential future directions for further exploration will be included.

The process commences with the extraction of thickness data from the radiographic image, which is then utilized and imported into an Ansys shell model. The primary objective of this thesis is to construct a shell model by leveraging the geometry data exported from the x-ray image. Subsequently, a thorough validation of the developed process is conducted to ensure its accuracy and reliability.

2. LITERATURE REVIEW

This literature review examines the widespread acceptance of x-ray usage across various fields, focusing on the advancements in radiographic imaging and improvements in finite element analysis. The utilization of computed tomography (CT) for creating Finite Element Models (FEM) is a prevalent practice within the medical field. However, there is a lack of established standards in this regard, with a predominant focus on using bones as specimens. Consequently, additional research has been conducted to explore the application of different materials in FEM creation. The primary objective of these studies was to evaluate the feasibility and accuracy of finite element analysis in characterizing these materials, while also investigating the specific approaches utilized to create the finite element models using x-ray images.

2.1 X-ray Technology

X-ray technology, developed in Germany on November 8, 1895, caused a sensation due to its see-through properties in both the scientific community and the press (Berger 1995). Early advancements in X-ray non-destructive testing were made globally, with notable work in the United Kingdom and Germany (Halmshaw 1988; Krüger & Weeber 1983). In the United States, Horace Lester's research at the Watertown Arsenal laid the foundation for the present use of radiography (Lester 1922; Lester 1923). Lester's work demonstrated the ability of X-rays to detect internal discontinuities in castings, welds, and other metal forms, which could lead to premature failure (Wenk 1969; Norton 1986).

Prior to Lester's research, significant work had already been done in radiographic non-destructive testing in the United States. A comprehensive review of early X-ray non-destructive testing was presented in a 1929 paper by Fink and Archer, which cited the research of Wheeler R. Davey at the General Electric Research Laboratory (Fink & Archer 1929). Davey's contributions to radiographic non-destructive testing were also acknowledged in the field (Heidt 1994).

During a lecture attended by Lester and Davey, Lester discussed the increasing use of steel forgings and welded structures, believed to be free from hidden defects and more reliable than castings. However, Lester's work at Watertown Arsenal disproved this assumption (Lester 1922). Davey made a comment emphasizing the limited economic sense of using radiography for 100% inspection, a sentiment previously emphasized by Lester (Fink &

Archer 1929). It was in this economic context that the American Society for Non-destructive Testing (ASNT) was established.

2.2 Radiographic Technology

Advancements in technology and techniques related to radiation safety (Morgan 1971), gamma radiography (Moore 1985; Briggs 1981; Bell 1984), high-voltage radiography (Straw 1984b; Straw 1984c; O'Connor & Cunningham 1949), portable X-ray machines (Hovland 1985; Bell 1984), and nucleonic gauging (Davis 1989) were observed during the period from 1935 to 1960 (Bossi 2019). These developments led to the expansion of radiographic testing in various industries, including shipbuilding (Lutts 1954), metals (Henry 1989) and aviation (Itoh 1982; Straw 1984a; Hagemaiier 1985).

While the fundamental method of radiographic testing remains similar to Röntgen's approach from a century ago, the twenty-first century has witnessed significant advancements in the understanding of image quality factors such as scatter and unsharpness, detectors, and x-ray sources. This progress has resulted in the availability of a wide range of techniques, such as digital radiography, computed tomography, computed radiography, laminography, dual energy, microradiography, backscatter imaging, flash techniques, and in-motion radiography (Bossi, 2019).

Looking ahead, technology will continue to advance in the field of non-destructive testing and X-ray technology. Promising directions include the increasing use of automated testing, computerized instrumentation, and the greater utilization of non-destructive test techniques in process control applications.

2.3 Finite Element Models

A recent account of the development of the Finite Element Method (FEM) and computational mechanics in general was provided by Zienkiewicz (2004). The foundation of FEM can be traced back to the early 1940s when Courant first developed the concept. The stiffness method, which served as a precursor to FEM, was introduced by Turner et al. (1956). The term "finite element" was coined by Clough in 1960. The computer implementation of FEM programs began to emerge in the early 1970s. Over time, FEM has evolved into one of the most widely used and versatile analysis techniques. Some notable milestones include; in 1943, Courant made significant contributions to the development of FEM by introducing variational methods that laid the foundation for this technique. In 1956, Turner, Clough, Martin, and Topp further advanced FEM with the introduction of the stiffness method. It was

in 1960 that Clough coined the term "Finite Element" and successfully solved plane problems using this approach. During the 1970s, FEM applications were primarily carried out on mainframe computers. The 1980s saw the advent of microcomputers and the development of pre- and postprocessors with graphical user interfaces (GUI). In the 1990s, FEM was employed for analysing large structural systems, as well as for tackling nonlinear and dynamic problems (Chen 2018; Liu 2022). In the 2000s, FEM expanded its capabilities to include the analysis of multiphysics and multiscale problems.

2.4 FEM using Computerized Tomography

In the following sections, we will delve into an extensive examination of the various methodologies used for generating finite element models (FEM) through the application of Computerized Tomography (CT). This exploration will encompass a wide range of materials, including concrete, asphalt mixture, non-crimp fabric-based fibre composites, aluminium foams, glass scaffolds, wood planks, and knee joints. Each material will be briefly discussed, providing valuable insights into their respective FEM creation processes. Furthermore, these research were studies to get a better understanding of the behaviour of various materials when subjected to x-ray imaging.

2.4.1 Diffusion of Chlorine in Concrete

Razmjoo (2013) attempted to create a 3D FEM for studying the precise forecasting of chlorine diffusion in concrete. However, several challenges were encountered during the creation of the FEM from Quantitative Computed Tomography (QCT) scan images. The CT scanner failed to identify fine aggregates within the structure, resulting in a uniform rather than detailed captured matrix. Moreover, the large size of the 3D model, with over 52 million elements and nodes, made it computationally impractical. To overcome these limitations, a 2D image modelling approach was chosen, and a smaller sample was cut from the structure for scanning. Abaqus software was then used to create a 2D FEM with 3 million elements. Although the final model was not precise, it provided valuable insights into the diffusion of chlorine in concrete.

2.4.2 Mechanical Behaviour of Asphalt Mixture

Huang (2016) employed FEM to study the mechanical behaviour of asphalt mixture. Multiple CT scans were conducted on the asphalt mixture, and a grey unit net matrix was created in Abaqus software. The resulting images were segmented using Otsu's method, and the voxel-based numerical model was established by transferring the x-ray data to the Abaqus

matrix. This FEM approach allowed for a comprehensive analysis of the mechanical properties of the asphalt mixture.

2.4.3 Non-Crimp Fabric-Based Fiber Composites

Jespersen (2018) presented a procedure for importing a fibre bundle structure of a non-crimp fabric-based fibre composite, obtained through X-ray CT scans, into a solvable 3D FEM in Abaqus software. The X-ray images were segmented in AVIZO software, followed by surface smoothing and filtering in geomagic wrap software. The final step involved meshing and modelling the 3D FEM in Abaqus. However, the segmentation of the X-ray data sets proved time-consuming, suggesting the need for future automation to improve efficiency and mesh quality.

2.4.4 X-ray CT scan-Based Finite Element Modelling of Composites

Auenhammer (2021) developed a comprehensive method for creating finite element models of non-crimp fabric-reinforced composites using X-ray CT scan data. The proposed X-ray computer tomography aided engineering (XAE) process encompassed image capture, automatic segmentation, meshing, and mapping. The thresholding segmentation method was employed, but the nearly automated single bundle segmentation was abandoned due to complexity. Avizo software expertise was necessary to determine appropriate parameters based on the composite design and fibre-matrix contrast. The hardware and software used in this approach were expensive, limiting its accessibility.

2.4.5 Aluminium Foams

Amani (2018) utilized X-ray tomography images of open-cell aluminium foams to model their behaviour using FEM. High-resolution scans were used to identify local intermetallic particles, while low-resolution scans were employed to assess deformation. Both heterogeneous and homogeneous FEM models were created, with the former effectively identifying possible fracture zones. However, the homogeneous model outperformed the heterogeneous model in predicting global stress-strain curves. This method can be applied to other architecture materials requiring consideration of both macroscopic and microstructural features.

2.4.6 Glass Scaffolds

Farina (2021) employed micro-CT-based FEM to explore the mechanical characteristics of 3D-printed glass scaffolds produced via robocasting. Voxel type meshing was utilized, and the results were compared with previous research on the same material. However, the

computational strategy had limitations, and the sample size was restricted due to the micro-scale nature of the model.

2.4.7 Wood Planks

Huber (2022) aimed to evaluate the bending stiffness and strength of wood planks by creating FE models from CT scans. Both 1D and 3D FE models were developed using the voxel approach for mesh generation. The study concluded that 1D FE models were equally precise in estimating the modulus of elasticity compared to 3D FE models.

2.4.8 Knee Joints

Jahangir (2022) developed a finite element model of knee joints using X-ray and MRI-based images. Anatomical dimensions were measured from both imaging modalities, and the FE model was morphed to closely resemble the actual knee specimen. By comparing the data from the atlas of 21 subjects, a more accurate FE model was obtained. Although the resulting model was not exact, it provided valuable insights into knee joint behaviour.

The studies reviewed in this report demonstrate the application of FEM in materials characterization using CT scans. Despite the challenges encountered, such as computational limitations and time-consuming segmentation processes, these studies have provided valuable insights into the mechanical behaviour and diffusion properties of various materials. Future research should focus on automation and cost reduction to enhance the accessibility and accuracy of FEM-based modelling techniques from CT.

2.5 Research gaps

Upon reviewing the literature pertaining to the extraction of geometry and other properties of tested specimens, it is apparent that the practice of utilizing x-ray imaging to obtain the geometry and subsequently develop a 2D finite element model in Ansys software has been largely overlooked. There is a lack of research demonstrating the utilization of radiography to create a finite element model (FEM) from x-ray images. Additionally, the extraction of data from x-ray images has predominantly been carried out using various software, with limited utilization of MATLAB software for this purpose. These methods have proven to be time-consuming and costly, often requiring multiple images of the material, further contributing to the overall time required. However, recent advancements in both MATLAB and Ansys offer the capability to perform most, if not all, of the necessary steps with greater accuracy and efficiency, thereby minimizing both time and cost, ultimately making the process more applicable to industry needs.

3. METHODOLOGY

This section will provide an in-depth explanation of the x-ray process and the method by which images are obtained from the x-rays. It will also discuss the development of a process that extracts the geometry from x-ray images, as well as the verification method used to validate this process.

3.1 Theory

Non-destructive testing using X-rays plays a crucial role in defect identification and measurement. Therefore, a comprehensive understanding of the linear attenuation coefficient of X-rays is essential (Dorobantu, 2004). The linear attenuation coefficient measures the rate at which X-rays lose intensity as they pass through a material, and it is influenced by factors such as the energy of the X-rays, the atomic composition of the material, and the thickness of the material.

In the case of steel, which is a dense material, X-rays are primarily absorbed rather than scattered. The density values in steel can be readily observed through x-ray analysis, while other metals such as aluminium require additional calibration to determine their density. Furthermore, aluminium poses a fatigue issue, making it unsuitable for use in car manufacturing. The interactions between X-rays and the atoms in the material, specifically through the photoelectric effect and Compton scattering, determine the linear attenuation coefficient in steel (Dorobantu, 2004).

The theory surrounding the thickness dependence of the linear attenuation coefficient often involves mathematical models or empirical relationships. These models aim to describe how the attenuation coefficient changes as the thickness of the steel increases, considering factors such as the energy of the X-rays, the atomic composition of the steel, and the physical properties of the material.

3.2 Specimen Design

The specimens used in this study were created using Steel A516 grade 70. This choice was made because steel is a commonly used structural material and is often used in the manufacturing of high-pressure vessels (Loginow, 1975). To ensure accuracy and consistency, the specimens were designed following the ASTM E8/E8M-13a standards, with dimensions of 450mmx50mmx6mm. Four different types of specimens were designed to

investigate how any uneven shape of the metal would appear in an x-ray image. Further details regarding the specimens will be discussed in sections 3.2.x.

The method of cutting the samples from the steel plate was carefully considered to minimize any impact on the material's properties. Laser cutting, although precise, was avoided due to potential alterations in the mechanical properties. Instead, water jet cutting was used to ensure that there would be no changes in the steel specimen's mechanical properties during the manufacturing process.

To ensure the specimens could withstand high loads without tearing or damage during tensile testing, the gripping space and holes were designed accordingly. The fixtures for the Instron were also designed based on the specifications of the specimens. The length of the specimen was intentionally selected as 450mm, in order to eliminate any potential issues with boundary conditions along the edges of the specimen.

3.2.1 Notched specimen

One of the surfaces of the specimens featured a notched specimen as seen in Figure 1, which was cut in a circular shape with a radius of 225mm. The cut was made by using a CNC cutting machine at a distance of 223mm from the surface of the specimen, resulting in a notch with a depth of 2mm. This specific design was chosen to gain insight into the challenges that may arise in radiographic imaging when dealing with varying thicknesses of specimens. Additionally, when constructing a Finite Element Method (FEM) model, it is necessary to modify the neutral axis to accurately capture secondary bending effects within the FEM.

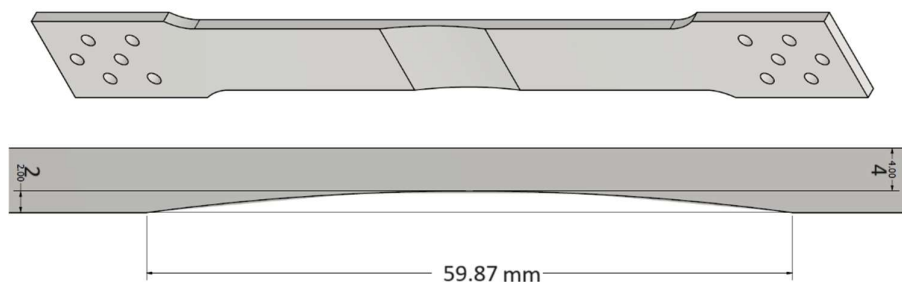


Figure 1 Notched dogbone specimen with radius 225mm (up) and notched dimensions (down)

3.2.2 Welded specimen

The subsequent specimen in this study was a welded specimen that underwent MIG welding at the centre of a plate. Following the welding process, the surface was carefully ground,

and any excess welded material was removed to ensure a flat surface. This preparation was vital for obtaining accurate observations of how the weld would appear under radiographic imaging. After the weld had cooled, the plate underwent post-manipulation techniques such as pressing and peening of the weld material to maintain its flatness. Finally, the specimen was precisely cut from the centre of the plate using water jet cutting. This systematic approach allowed for comprehensive examination of the weld's characteristics during radiographic imaging.

3.2.3 Middle cut slit specimen

The subsequent specimen featured a horizontally cut slit with dimensions measuring 1.8x10 mm. Initially, the intention was to create a narrower slit, but the water jet cutting machine used has a minimum cut accuracy for material removal is 0.9mm.

3.2.4 Artificial corrosion specimen

The following sample was referred to as an artificially corroded sample, which exhibited an irregular shape as depicted in the figure 2. This specific shape was achieved through the utilization of a CNC cutting machine.

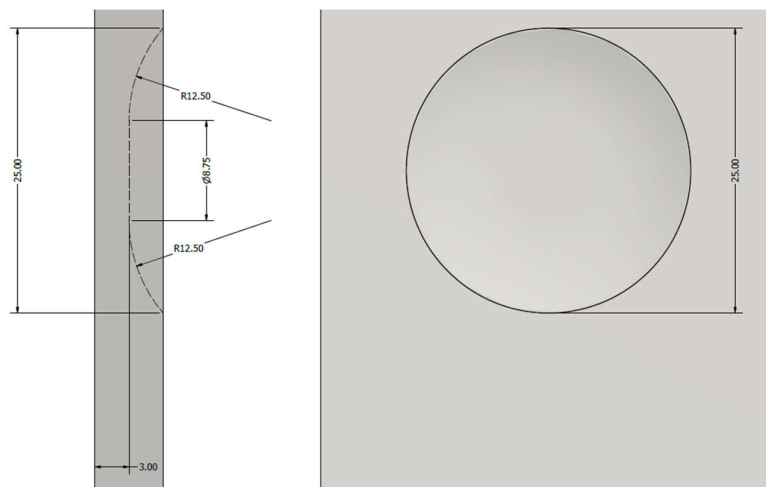


Figure 2 Artificially corroded specimen with uneven shape (side view and front view)

3.3 Surface treatments

Once all the specimens were prepared, they underwent sandblasting to safeguard against corrosion, considering that they were cut using water. Following the sandblasting process, the specimens were coated with white paint, and a speckle pattern was created by spraying black paint into the air onto the specimens. This speckle pattern served the purpose of

facilitating the measurement of strain values using Digital Image Correlation (DIC) techniques. As the specimens were created, corresponding fixtures were also designed to securely hold them during the tensile testing process using an Instron machine. All four prepared specimens' surfaces, which are ready for testing, can be observed in figure 3.



Figure 3 The surfaces of all four prepared specimens are in their original condition prior to testing.

4. X-RAY EXTRACTION

This section provides an explanation of the underlying concept of how X-ray works and how it will be utilized to extract the thickness value. Additionally, it discusses the rationale behind studying notched and artificially corroded specimens, as well as the decision to avoid welded and middle cut specimens.

4.1 Theory

The fundamental principle of X-ray techniques involves determining the remaining incident radiation after passing through a material. The relationship between the incident intensity (I_0) and the intensity after traversing the material (I) is defined by,

$$I(x) = I_0 e^{-\mu x}, \quad (1)$$

where x is the material thickness and μ represents the linear attenuation factor or absorption factor of the material. The absorption process is encapsulated in μ . By comparing expressions for intensity and the refractive index, the linear attenuation coefficient (μ) can be derived (Dorobantu 2004). Here, the absorption factor (μ) is dependent on thickness (t) by $\mu = a * t + b\sqrt{t}$. The attenuation of X-rays primarily arises from the photoelectric effect, Compton effect, and electron-positron pair production.

Regarding the thickness dependence, the linear attenuation coefficient (μ) is defined for monochromatic radiation, but X-rays are polychromatic due to the de-excitation process of highly excited atomic states. As a result, the absorption of X-rays can be expressed as a sum of contributions from all components of the beam. Taking the logarithm of this expression reveals that the linear attenuation coefficient is dependent on the thickness (x) of the material and is defined by (Dorobantu, 2004),

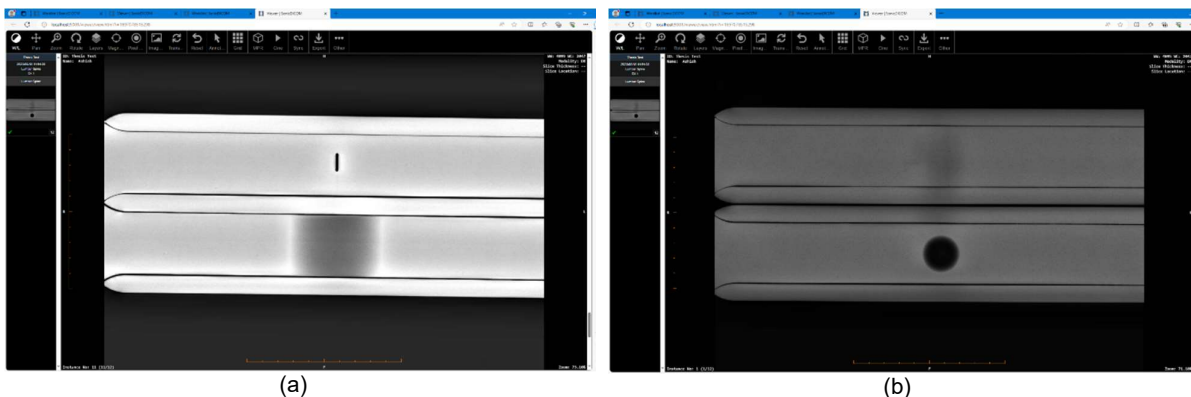
$$\mu(x) = a + \frac{b}{\sqrt{x}}, \quad (2)$$

where a and b are material-dependent constants. Further expansions and evaluations demonstrate that the linear attenuation coefficient of electromagnetic waves decreases as the thickness increases.

4.2 Radiographic Imaging Process

During the radiographic procedure, the specimen is subjected to a passage of x-ray beams. As the x-rays travel through the specimen, a certain portion of them is either absorbed or scattered by its internal structure. The resulting x-ray pattern, which consists of the remaining x-rays, is then transmitted to a detector. Subsequently, the image (formed based on the amount of x-ray absorbed by the specimen) is recorded and stored for later evaluation. The prescribed measurement parameters dictate that the x-ray machine is to be operated at a voltage of 130 kV and a current of 5 mA. The distance between the x-ray source and the detector (imaging plate), known as the source-to-detector distance, is set at 600 mm (Bayu 2018). Additionally, the exposure time for capturing the x-ray image is set at 45 seconds.

The x-ray procedure involved the use of the Philips Digital Diagnost Direct Radiography / DigitalDiagnost 4.1 device, configured with the aforementioned settings. Both the front and back of the specimens were x-rayed, and to prevent any ghosting artifacts, a blank shot was captured after each x-ray image. Furthermore, a support system was employed to mitigate the edge effect, resulting in the elimination of brighter edges in the specimen's x-ray images. A total of 16 images, each acquired with different settings, were compiled onto a CD, and subsequently viewed using the Sonic DIACOM Media Viewer. The captured images are seen in figure 4.



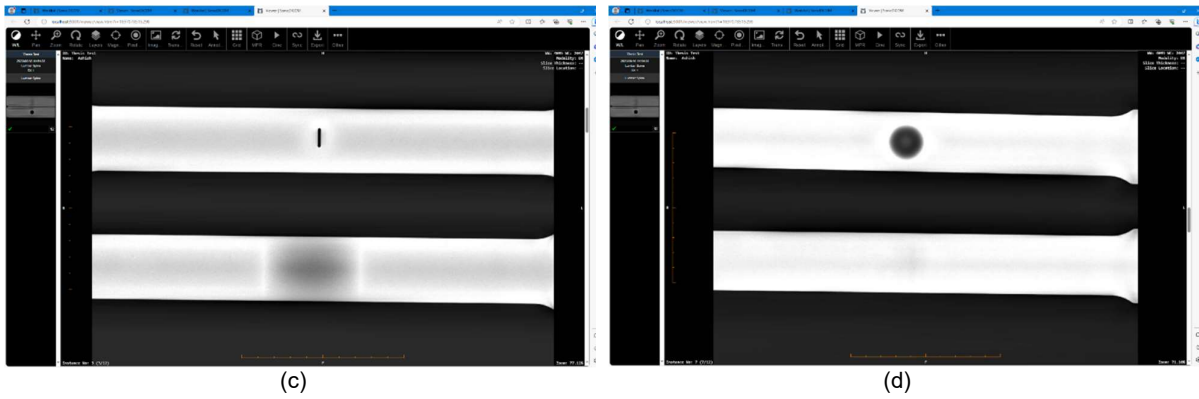


Figure 4 The captured x-ray images viewed using Sonic DiacomViewer: (a). Slit and notched specimen with supports. (b). Welded and artificially corroded specimen with supports. (c). Slit and notched specimen without any support. (d). Artificial corrosion and welded specimen without any support.

The captured x-ray images are stored in the .DIACOM file format, which can be converted to .jpeg using the Sonic DIACOM Media Viewer. MATLAB can then be used to extract the RGB (red green blue) pixel values from the images. By zooming in on the image, the RGB values can be examined more closely and extracted into a .csv or Excel file.

Row	Col 1	Col 2	Col 3	Col 4	Col 5	Col 6	Col 7	Col 8	Col 9	Col 10	Col 11	Col 12	Col 13	Col 14	Col 15	Col 16	Col 17	Col 18	Col 19	Col 20	Col 21	Col 22	Col 23	Col 24	Col 25	Col 26	Col 27	Col 28	Col 29	Col 30	Col 31	Col 32	Col 33	Col 34	Col 35	Col 36	Col 37	Col 38	Col 39	Col 40	Col 41	Col 42	Col 43	Col 44	Col 45	Col 46	Col 47	Col 48	Col 49	Col 50	Col 51	Col 52	Col 53	Col 54	Col 55	Col 56	Col 57	Col 58	Col 59	Col 60	Col 61	Col 62	Col 63	Col 64	Col 65	Col 66	Col 67	Col 68	Col 69	Col 70	Col 71	Col 72	Col 73	Col 74	Col 75	Col 76	Col 77	Col 78	Col 79	Col 80	Col 81	Col 82	Col 83	Col 84	Col 85	Col 86	Col 87	Col 88	Col 89	Col 90	Col 91	Col 92	Col 93	Col 94	Col 95	Col 96	Col 97	Col 98	Col 99	Col 100																																																																																																																																																																																																																																																																																																																																																																																																																																																																																																																																																																																																																																																																																																																																																																																																																																																				
37	0.1002	0.1014	0.1022	0.1027	0.1031	0.1034	0.1037	0.1039	0.1041	0.1043	0.1045	0.1047	0.1049	0.1051	0.1053	0.1055	0.1057	0.1059	0.1061	0.1063	0.1065	0.1067	0.1069	0.1071	0.1073	0.1075	0.1077	0.1079	0.1081	0.1083	0.1085	0.1087	0.1089	0.1091	0.1093	0.1095	0.1097	0.1099	0.1101	0.1103	0.1105	0.1107	0.1109	0.1111	0.1113	0.1115	0.1117	0.1119	0.1121	0.1123	0.1125	0.1127	0.1129	0.1131	0.1133	0.1135	0.1137	0.1139	0.1141	0.1143	0.1145	0.1147	0.1149	0.1151	0.1153	0.1155	0.1157	0.1159	0.1161	0.1163	0.1165	0.1167	0.1169	0.1171	0.1173	0.1175	0.1177	0.1179	0.1181	0.1183	0.1185	0.1187	0.1189	0.1191	0.1193	0.1195	0.1197	0.1199	0.1201	0.1203	0.1205	0.1207	0.1209	0.1211	0.1213	0.1215	0.1217	0.1219	0.1221	0.1223	0.1225	0.1227	0.1229	0.1231	0.1233	0.1235	0.1237	0.1239	0.1241	0.1243	0.1245	0.1247	0.1249	0.1251	0.1253	0.1255	0.1257	0.1259	0.1261	0.1263	0.1265	0.1267	0.1269	0.1271	0.1273	0.1275	0.1277	0.1279	0.1281	0.1283	0.1285	0.1287	0.1289	0.1291	0.1293	0.1295	0.1297	0.1299	0.1301	0.1303	0.1305	0.1307	0.1309	0.1311	0.1313	0.1315	0.1317	0.1319	0.1321	0.1323	0.1325	0.1327	0.1329	0.1331	0.1333	0.1335	0.1337	0.1339	0.1341	0.1343	0.1345	0.1347	0.1349	0.1351	0.1353	0.1355	0.1357	0.1359	0.1361	0.1363	0.1365	0.1367	0.1369	0.1371	0.1373	0.1375	0.1377	0.1379	0.1381	0.1383	0.1385	0.1387	0.1389	0.1391	0.1393	0.1395	0.1397	0.1399	0.1401	0.1403	0.1405	0.1407	0.1409	0.1411	0.1413	0.1415	0.1417	0.1419	0.1421	0.1423	0.1425	0.1427	0.1429	0.1431	0.1433	0.1435	0.1437	0.1439	0.1441	0.1443	0.1445	0.1447	0.1449	0.1451	0.1453	0.1455	0.1457	0.1459	0.1461	0.1463	0.1465	0.1467	0.1469	0.1471	0.1473	0.1475	0.1477	0.1479	0.1481	0.1483	0.1485	0.1487	0.1489	0.1491	0.1493	0.1495	0.1497	0.1499	0.1501	0.1503	0.1505	0.1507	0.1509	0.1511	0.1513	0.1515	0.1517	0.1519	0.1521	0.1523	0.1525	0.1527	0.1529	0.1531	0.1533	0.1535	0.1537	0.1539	0.1541	0.1543	0.1545	0.1547	0.1549	0.1551	0.1553	0.1555	0.1557	0.1559	0.1561	0.1563	0.1565	0.1567	0.1569	0.1571	0.1573	0.1575	0.1577	0.1579	0.1581	0.1583	0.1585	0.1587	0.1589	0.1591	0.1593	0.1595	0.1597	0.1599	0.1601	0.1603	0.1605	0.1607	0.1609	0.1611	0.1613	0.1615	0.1617	0.1619	0.1621	0.1623	0.1625	0.1627	0.1629	0.1631	0.1633	0.1635	0.1637	0.1639	0.1641	0.1643	0.1645	0.1647	0.1649	0.1651	0.1653	0.1655	0.1657	0.1659	0.1661	0.1663	0.1665	0.1667	0.1669	0.1671	0.1673	0.1675	0.1677	0.1679	0.1681	0.1683	0.1685	0.1687	0.1689	0.1691	0.1693	0.1695	0.1697	0.1699	0.1701	0.1703	0.1705	0.1707	0.1709	0.1711	0.1713	0.1715	0.1717	0.1719	0.1721	0.1723	0.1725	0.1727	0.1729	0.1731	0.1733	0.1735	0.1737	0.1739	0.1741	0.1743	0.1745	0.1747	0.1749	0.1751	0.1753	0.1755	0.1757	0.1759	0.1761	0.1763	0.1765	0.1767	0.1769	0.1771	0.1773	0.1775	0.1777	0.1779	0.1781	0.1783	0.1785	0.1787	0.1789	0.1791	0.1793	0.1795	0.1797	0.1799	0.1801	0.1803	0.1805	0.1807	0.1809	0.1811	0.1813	0.1815	0.1817	0.1819	0.1821	0.1823	0.1825	0.1827	0.1829	0.1831	0.1833	0.1835	0.1837	0.1839	0.1841	0.1843	0.1845	0.1847	0.1849	0.1851	0.1853	0.1855	0.1857	0.1859	0.1861	0.1863	0.1865	0.1867	0.1869	0.1871	0.1873	0.1875	0.1877	0.1879	0.1881	0.1883	0.1885	0.1887	0.1889	0.1891	0.1893	0.1895	0.1897	0.1899	0.1901	0.1903	0.1905	0.1907	0.1909	0.1911	0.1913	0.1915	0.1917	0.1919	0.1921	0.1923	0.1925	0.1927	0.1929	0.1931	0.1933	0.1935	0.1937	0.1939	0.1941	0.1943	0.1945	0.1947	0.1949	0.1951	0.1953	0.1955	0.1957	0.1959	0.1961	0.1963	0.1965	0.1967	0.1969	0.1971	0.1973	0.1975	0.1977	0.1979	0.1981	0.1983	0.1985	0.1987	0.1989	0.1991	0.1993	0.1995	0.1997	0.1999	0.2001	0.2003	0.2005	0.2007	0.2009	0.2011	0.2013	0.2015	0.2017	0.2019	0.2021	0.2023	0.2025	0.2027	0.2029	0.2031	0.2033	0.2035	0.2037	0.2039	0.2041	0.2043	0.2045	0.2047	0.2049	0.2051	0.2053	0.2055	0.2057	0.2059	0.2061	0.2063	0.2065	0.2067	0.2069	0.2071	0.2073	0.2075	0.2077	0.2079	0.2081	0.2083	0.2085	0.2087	0.2089	0.2091	0.2093	0.2095	0.2097	0.2099	0.2101	0.2103	0.2105	0.2107	0.2109	0.2111	0.2113	0.2115	0.2117	0.2119	0.2121	0.2123	0.2125	0.2127	0.2129	0.2131	0.2133	0.2135	0.2137	0.2139	0.2141	0.2143	0.2145	0.2147	0.2149	0.2151	0.2153	0.2155	0.2157	0.2159	0.2161	0.2163	0.2165	0.2167	0.2169	0.2171	0.2173	0.2175	0.2177	0.2179	0.2181	0.2183	0.2185	0.2187	0.2189	0.2191	0.2193	0.2195	0.2197	0.2199	0.2201	0.2203	0.2205	0.2207	0.2209	0.2211	0.2213	0.2215	0.2217	0.2219	0.2221	0.2223	0.2225	0.2227	0.2229	0.2231	0.2233	0.2235	0.2237	0.2239	0.2241	0.2243	0.2245	0.2247	0.2249	0.2251	0.2253	0.2255	0.2257	0.2259	0.2261	0.2263	0.2265	0.2267	0.2269	0.2271	0.2273	0.2275	0.2277	0.2279	0.2281	0.2283	0.2285	0.2287	0.2289	0.2291	0.2293	0.2295	0.2297	0.2299	0.2301	0.2303	0.2305	0.2307	0.2309	0.2311	0.2313	0.2315	0.2317	0.2319	0.2321	0.2323	0.2325	0.2327	0.2329	0.2331	0.2333	0.2335	0.2337	0.2339	0.2341	0.2343	0.2345	0.2347	0.2349	0.2351	0.2353	0.2355	0.2357	0.2359	0.2361	0.2363	0.2365	0.2367	0.2369	0.2371	0.2373	0.2375	0.2377	0.2379	0.2381	0.2383	0.2385	0.2387	0.2389	0.2391	0.2393	0.2395	0.2397	0.2399	0.2401	0.2403	0.2405	0.2407	0.2409	0.2411	0.2413	0.2415	0.2417	0.2419	0.2421	0.2423	0.2425	0.2427	0.2429	0.2431	0.2433	0.2435	0.2437	0.2439	0.2441	0.2443	0.2445	0.2447	0.2449	0.2451	0.2453	0.2455	0.2457	0.2459	0.2461	0.2463	0.2465	0.2467	0.2469	0.2471	0.2473	0.2475	0.2477	0.2479	0.2481	0.2483	0.2485	0.2487	0.2489	0.2491	0.2493	0.2495	0.2497	0.2499	0.2501	0.2503	0.2505	0.2507	0.2509	0.2511	0.2513	0.2515	0.2517	0.2519	0.2521	0.2523	0.2525	0.2527	0.2529	0.2531	0.2533	0.2535	0.2537	0.2539	0.2541	0.2543	0.2545	0.2547	0.2549	0.2551	0.2553	0.2555	0.2557	0.2559	0.2561	0.2563	0.2565	0.2567	0.2569	0.2571	0.2573	0.2575	0.2577	0.2579	0.2581	0.2583	0.2585	0.2587	0.2589	0.2591	0.2593	0.2595	0.2597	0.2599	0.2601	0.2603	0.2605	0.2607	0.2609	0.2611	0.2613	0.2615	0.2617	0.2619	0.2621	0.2623	0.2625	0.2627	0.2629	0.2631	0.2633	0.2635	0.2637	0.2639	0.2641	0.2643	0.2645	0.2647	0.2649	0.2651	0.2653	0.2655	0.2657	0.2659	0.2661	0.2663	0.2665	0.2667	0.2669	0.2671	0.2673	0.2675	0.2677	0.2679	0.2681	0.2683	0.2685	0.2687	0.2689	0.2691	0.2693	0.2695	0.2697	0.2699	0.2701	0.2703	0.2705	0.2707	0.2709	0.2711	0.2713	0.2715	0.2717	0.2719	0.2721	0.2723	0.2725	0.2727	0.2729	0.2731	0.2733	0.2735	0.2737	0.2739	0.2741	0.2743	0.2745	0.2747	0.2749	0.2751	0.2753	0.2755	0.2757	0.2759	0.2761	0.2763	0.2765	0.2767	0.2769	0.2771	0.2773	0.2775	0.2777	0.2779	0.2781	0.2783	0.2785	0.2787	0.2789	0.2791	0.2793	0.2795	0.2797	0.2799	0.2801	0.2803	0.2805	0.2807	0.2809	0.2811	0.2813	0.2815	0.2817	0.2819	0.2821	0.2823	0.2825	0.2827	0.2829	0.2831	0.2833	0.2835	0.2837	0.2839	0.2841	0.2843	0.2845	0.2847	0.2849	0.2851	0.2853	0.2855	0.2857	0.2859	0.2861	0

for the extracted geometry. Following this, the user selects the relevant x-ray .diacom file from which the geometry data needs to be extracted.

The code then proceeds to identify the thickest section of the specimen by selecting the brightest location in the image. This section of the code was designed to adjust the contrast of the image in order to improve visibility. Occasionally, a pixel would be significantly different, resulting in a dark and difficult-to-see image. If the x-ray image is not aligned with the specimen, the code allows for image rotation to ensure accurate data extraction. This is achieved by clicking on two points along the edge of the desired specimen section.

Next, the user defines the area of analysis by clicking on four points in the image. Additionally, the entire width and length of the specimen were carefully chosen during this process. Figure 6 employs a dashed box to visually depict the area of analysis. The dimensions of this area were evaluated based on the known width of the specimen. This ensures that only the relevant section of the specimen is considered for geometry extraction.

Once this is done, a straight image of the section is obtained, the x-ray image with straightened orientation and enhanced contrast values is visible in Figure 6.

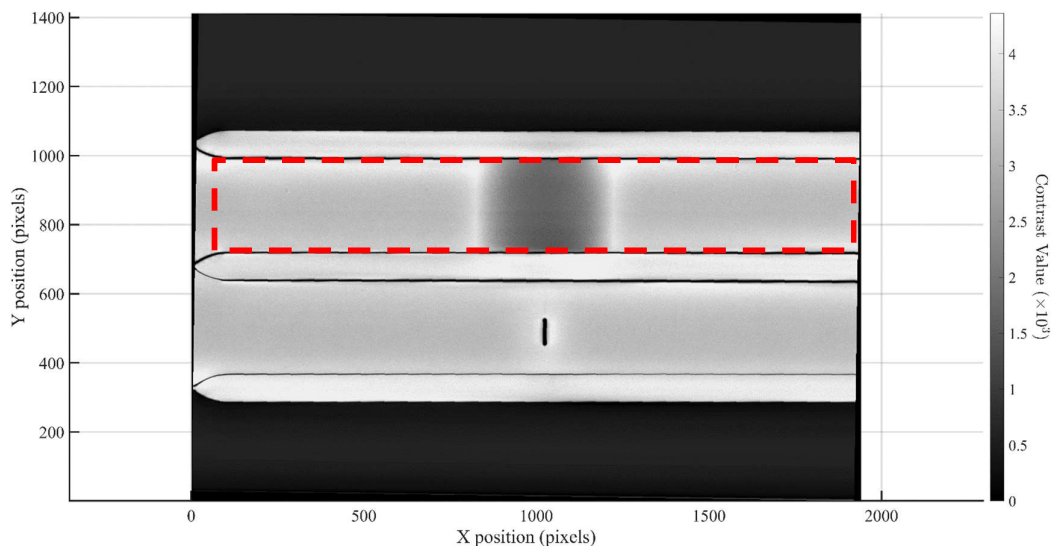


Figure 6 As part of the thickness extraction process, the X-ray image is rectified and a plot is generated to visualize the contrast values.

The MATLAB code was designed to extract the geometry data and create a graph depicting the central geometry. Initially, the plot contained a significant amount of noise, as evident in the Figure 7.

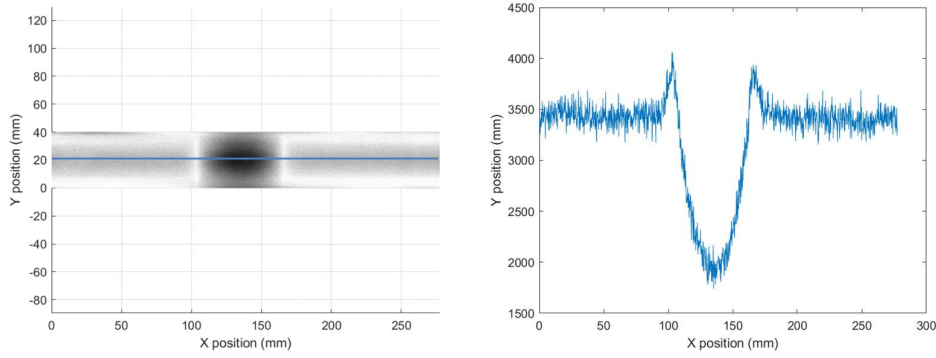


Figure 7 Extracted targeting section of the x-ray image and centre line in red (left) with the geometry data (right) along the centre line [x-z axis]

To obtain smooth geometry results, the MATLAB code was modified by averaging the data over 1 mm. This adjustment was made to reduce the noise and achieve the desired outcome. After selecting the area of analysis, the X-ray contrast data was averaged over a 1 mm mesh. This step aimed to minimize noise and expedite the computation time required for thickness calculations.

To evaluate the thickness, the constants a and b needed to be evaluated from Equation (2). In practical application, it is necessary to utilize calibration blocks of the material with different thicknesses to evaluate the values of a and b . Unfortunately, this requirement was identified late in the project, leaving insufficient time to produce the calibration blocks and conduct the necessary additional tests. To achieve this, the values of a and b were solved at 6 mm and at the reduced section of the specimen's geometry change. This involved simultaneously solving Equation (1) for the contrast values at both the original material thickness and the minimum of the reduced section in the geometry. For the notched specimen, the constants a and b were solved using the following simultaneous equations:

$$I_0 - C(6 \text{ mm}) = I_0 * e^{(a * (6 \text{ mm}) + b * \sqrt{6 \text{ m}})}$$

$$I_0 - C(4 \text{ mm}) = I_0 * e^{(a * (4 \text{ mm}) + b * \sqrt{4 \text{ m}})}$$

where I_0 is the initial X-ray contrast intensity and $C(t)$ is the contrast absorption for a specific thickness of the material. Once a and b had been evaluated the contrast values can be converted to thickness by solving for thickness of,

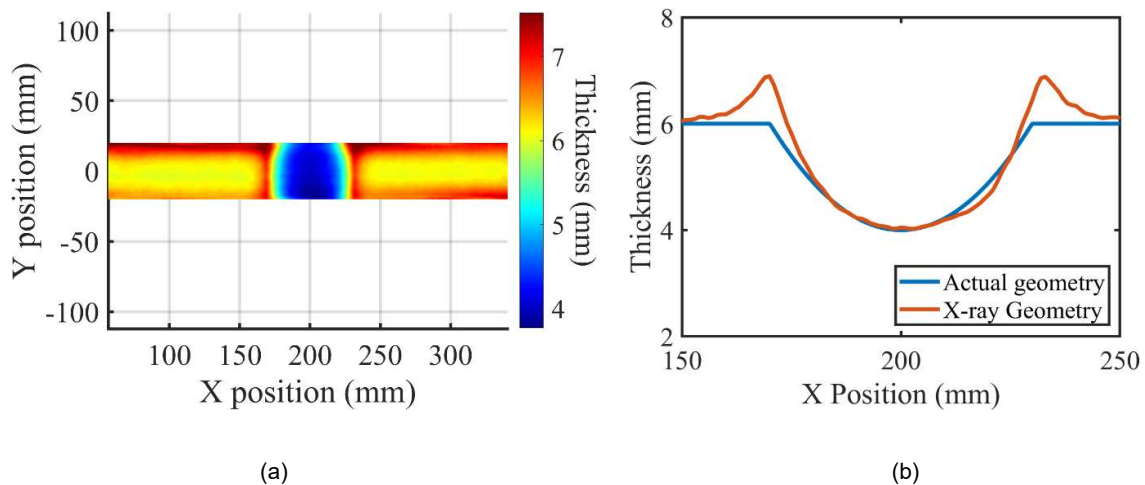
$$a * t + b * \sqrt{t} - \log_e \left(\frac{(I_0 - C)}{I_0} \right) = 0$$

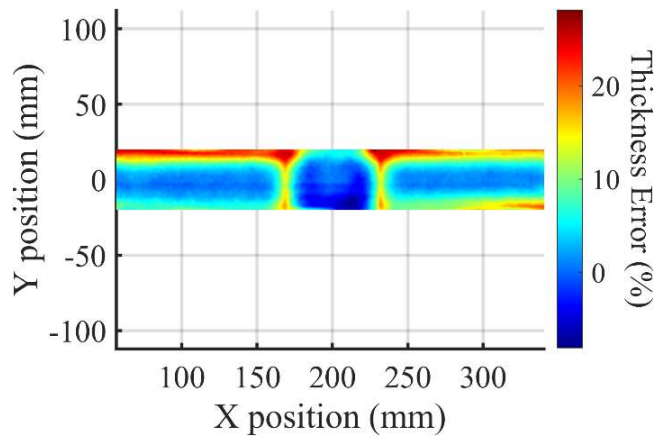
A graph is then generated to display the geometry data along the length of the specimen, highlighting the centreline geometry extraction and the associated error percentage. A geometry file was generated specifically for importing into your Finite Element Analysis (FEA) model.

4.4 Results

The first plot (Figure 8a) illustrates the distribution of thickness across the designated area of the specimen. The second plot (8b) displays the geometry graph of the centre of the specimen in the longitudinal direction. Additionally, a comparison between the original geometry and the extracted geometry is plotted. The results indicate that the edges of the specimen appear thicker than the original shape, which may be attributed to the edge effect of the x-ray on the metal specimen. This effect, known as beam hardening, causes the image to appear brighter near the edges (Park 2015).

Furthermore, Figure 8c is depicting the error in the captured radiographic image is presented. The graph reveals that the error at the edges is approximately 20%, while the accuracy improves towards the centre. However, the error percentage still increases with changes in the shape. Notably, the top side of the image exhibits more error, likely due to the specimen not being positioned centrally to the x-ray tube. This emphasizes the significance of the x-ray tube's position in determining the accuracy of the extracted geometry values. Finally, the last plot illustrates the thickness values extracted from the x-ray image, as shown in the Figure 8.

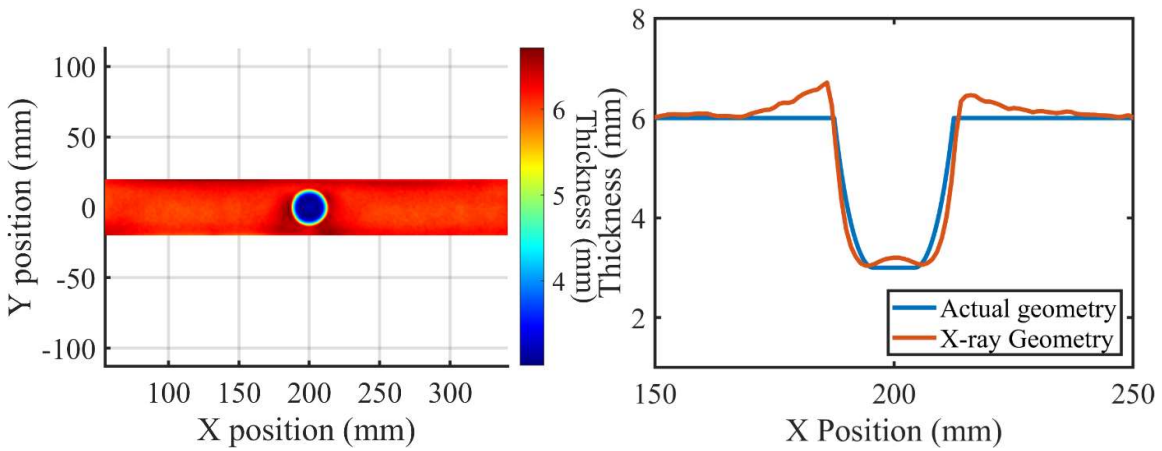




(c)

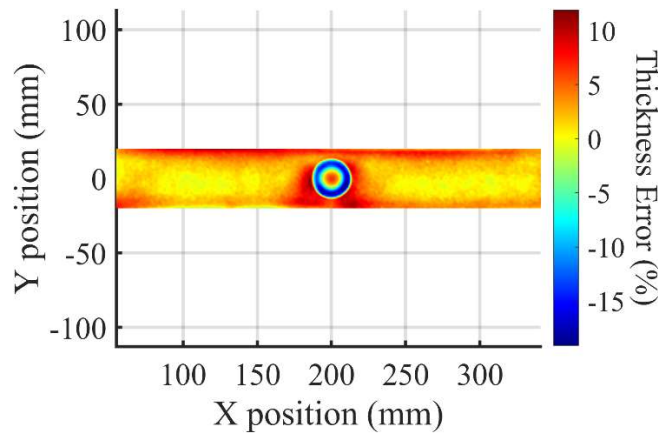
Figure 8 The extracted data from the notched specimen geometry includes three plots. (a) Surface thickness plot, (b) Line thickness plot, (c) Thickness error plot.

During the data extraction process from the artificially corroded specimen, a similar edge effect caused by beam hardening is observed in the extracted geometry. Efforts were made to minimize errors caused by noise and the beam hardening effect by comparing pixel values with the actual geometry. However, it is worth noting that the extracted geometry from the corroded specimen is more accurate compared to the notch specimen. Figure 9 also depicts the same plots for thickness extraction and error percentage analysis for the artificially corroded specimen.



(a)

(b)



(c)

Figure 9 The extracted data from the artificially corroded specimen geometry includes three plots. (a) Surface thickness plot, (b) Line thickness plot, (c) Thickness error plot.

4.5 Discussion

It is apparent that radiographic images do not offer precise geometric information about the specimen, but they do provide a general indication of its shape. Therefore, the exported geometry to ANSYS has been altered in a way that any thickness values exceeding 6 mm have been adjusted to 6 mm. It is also evident that the absorption values obtained from a single x-ray image are insufficient for extracting the exact geometry of the specimen. This limitation is attributed to the beam hardening effect, which has been identified as the primary cause of errors. Mitigating these errors would require reducing the beam hardening effect of the x-ray. Despite this limitation, radiographic imaging yields accurate results when the surface being examined is uniform.

The analysis of the centreline geometry extraction in the welded specimen reveals that it is unable to accurately define the specimen's geometry due to the presence of welded material that differs from the steel A516. This discrepancy is evident in Appendix A, Section 3. Similarly, the slit (middle cut section) in Appendix A, Section 4 also exhibits the same issue. As a result, these specimens necessitate the use of x-ray intensity values with absorption values. Consequently, these specimens are unsuitable for validating the developed process.

4.6 Summary

In summary, this section outlines the process and methodology of radiography. The extraction of geometry from an x-ray image involves comparing the contrast of the image

with the known thickness. By comparing the highest pixel values with the maximum thickness, the geometry of the specimen can be determined. In subsequent x-ray shots, there will be no need for inputting the thickness as the contrast values are already available at the same x-ray settings. The percentage of error in this process is also calculated, and efforts are made to minimize this error to obtain the most accurate geometry possible. The X-ray image's extracted data is subsequently utilized in the FE shell model.

5. FINITE ELEMENT MODELLING

5.1 Finite Element Modelling Process (importing Geometry)

The development of finite element models for the specimens involved the utilization of Ansys Workbench. To ensure symmetry, the finite element model was created as half of the specimen, taking into account the symmetrical surface patterns. Both shell and solid models were generated for the specimens. It is crucial to emphasize that the geometry of the shell models in the Finite Element Modelling section was imported into ANSYS from the extracted geometry obtained from the x-ray. ANSYS then adjusts the thickness at the nodes of each shell element to align with the imported geometry. This process ensures an accurate representation of the shell models in the analysis. The Ansys Workbench screen displays the solid and shell models, as well as the flow of the developed finite element method (FEM), as depicted in Figure 10.

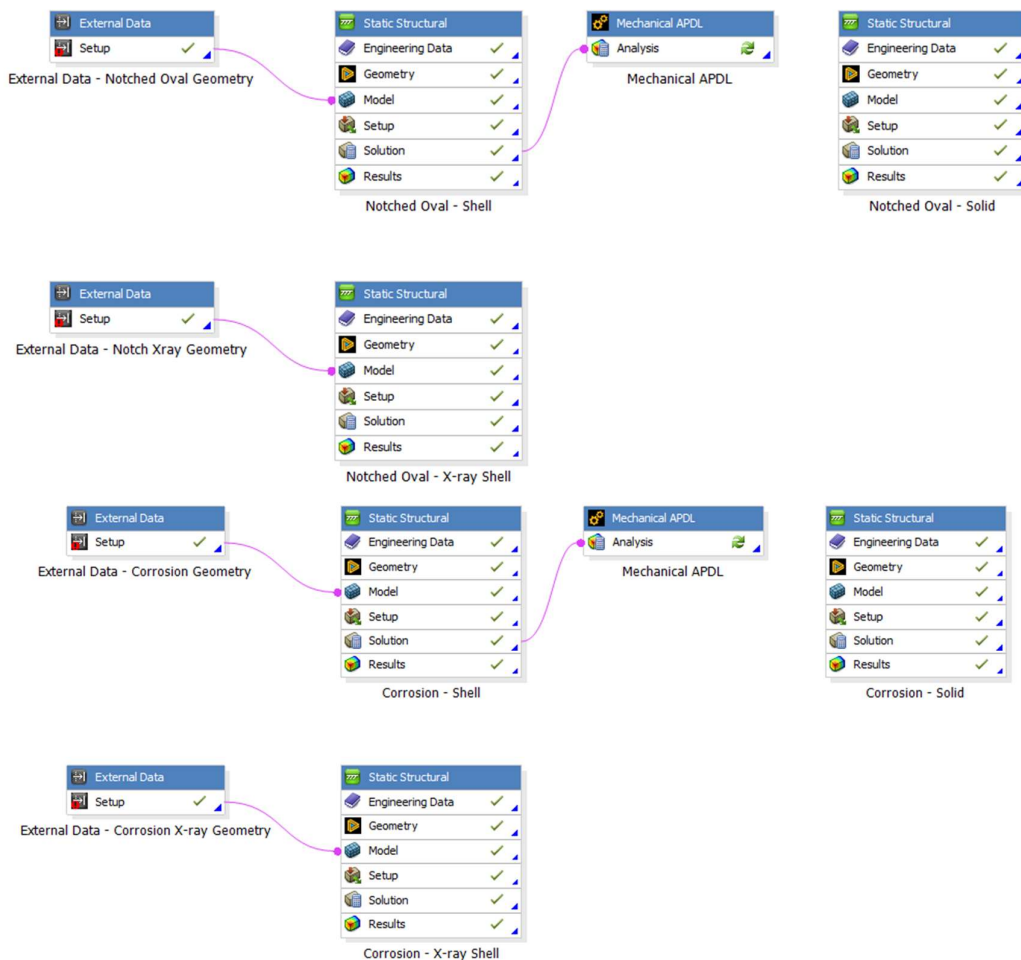


Figure 10 The figure illustrates the flow of the shell model and solid model development in Ansys Workbench. It also showcases the integration of an imported shell model with x-ray thickness data.

The shell and solid models were generated to facilitate a comparison between the results of the 2D and 3D models, thereby providing evidence of the effectiveness of 2D FEM. The mesh size of the specimens was set at 1mm, as evident in Figure 11 & 13.

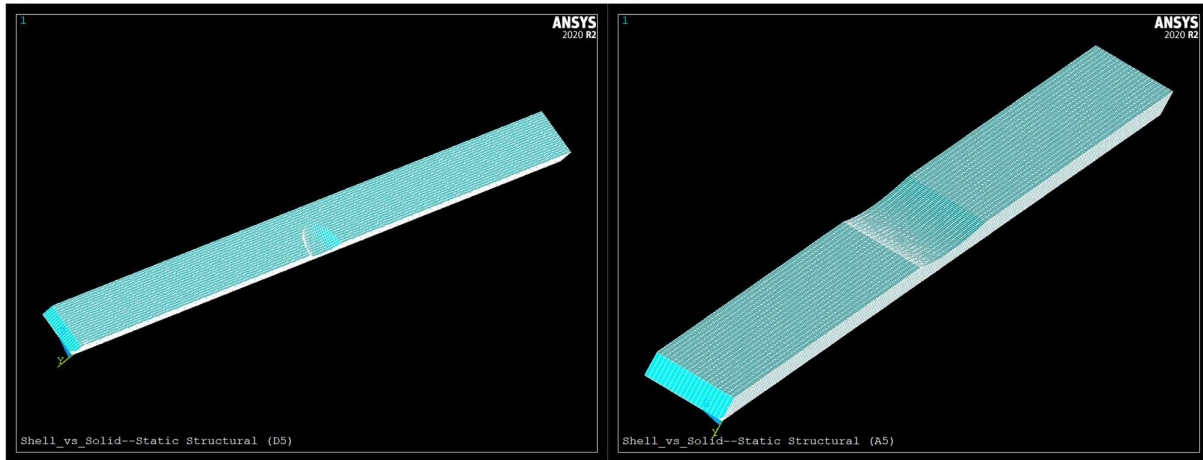


Figure 11 Shell model (FEM 2D) with Mesh in Ansys of artificial corrosion (left) and notched (right) [Ansys Classic]

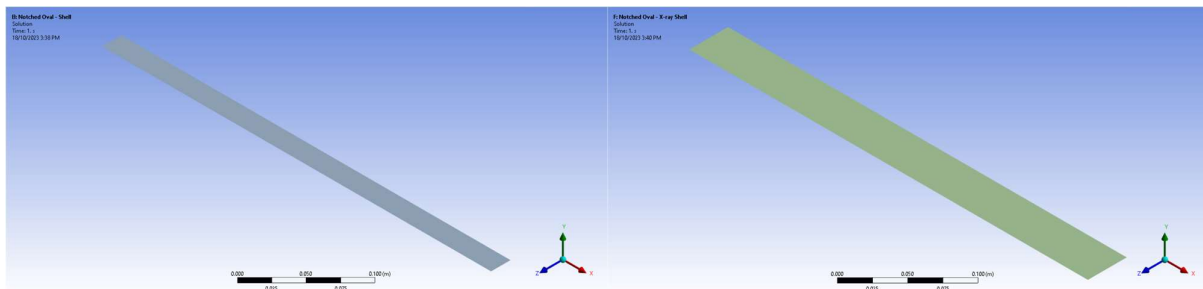


Figure 12 Shell model (FEM 2D) in Ansys of notched normal (left) and X-ray model (right) [Ansys Workbench]

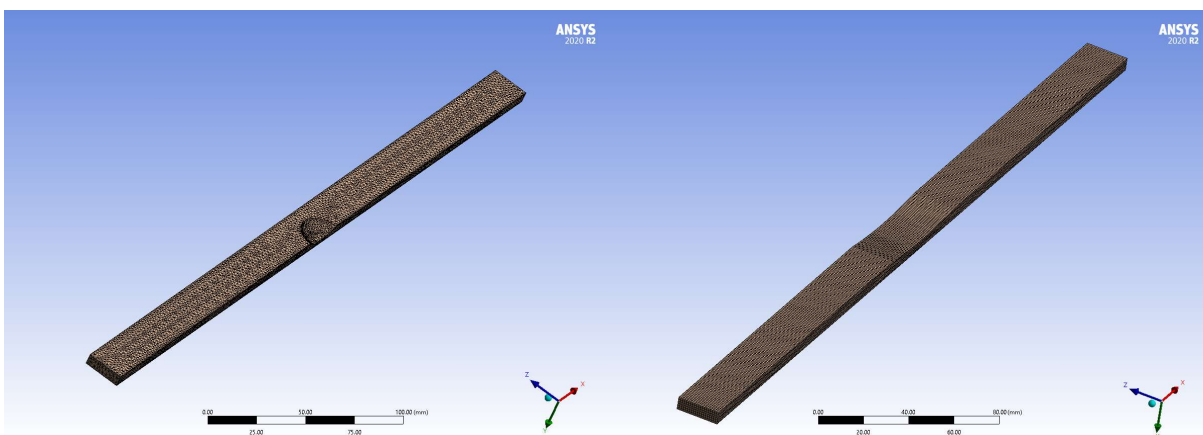


Figure 13 Solid model (FEM 3D) with Mesh in Ansys of artificial corrosion (left) and notched (right)

The geometry data obtained from the x-ray contrast will be utilized to define the specimen's geometry in the ANSYS model. Additionally, a Modulus of Elasticity of 230 GPa, derived from the results of tensile testing conducted by my colleague, NirajKumar Patel, has been incorporated into this ANSYS model. The parameters established for the tensile testing are identical to those employed in the verification test conducted with the Instron machine.

5.2 Shell-Solid Comparison (Mesh Study)

The stress distribution analysis was conducted on both the notched and artificially corroded specimens, and the results are depicted in the Figure 14. Additionally, strain values were recorded from the test and compared with the strain values obtained from both the 2D and 3D finite element models. It is observed in Figure 15 that the solid model exhibits a secondary bending phenomenon that is absent in the shell model. This discrepancy is attributed to the fact that a shell model, being a 2D representation, lacks the capability to account for changes in the neutral axis.

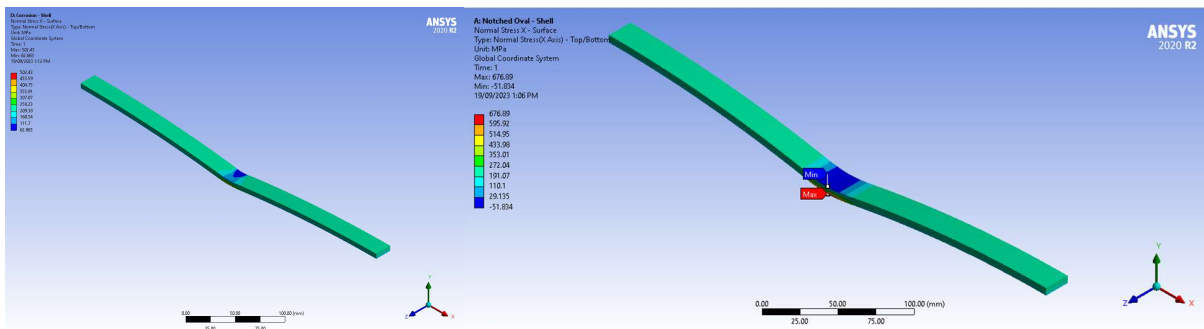


Figure 14 Stress distribution in artificial corrosion (left) and notched (right) specimen [Solid model (FEM 3D)]

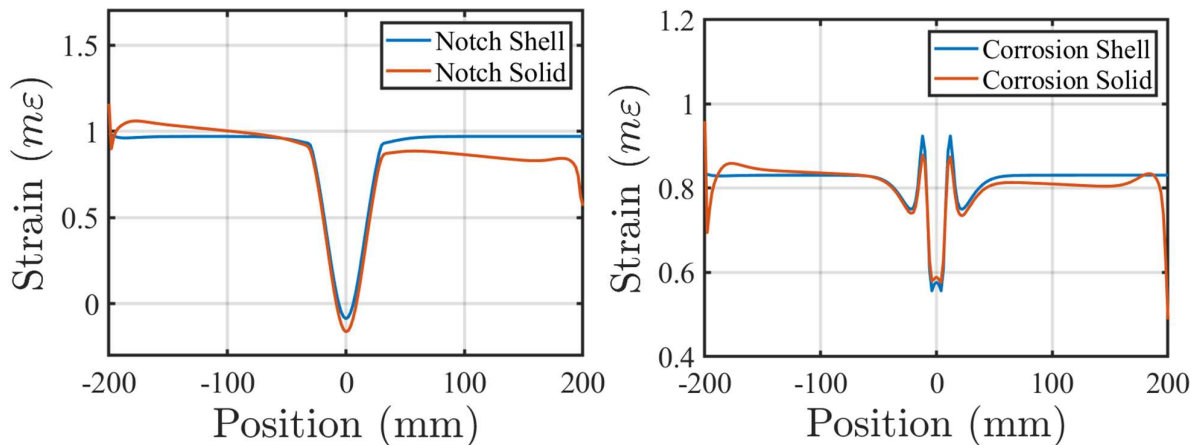


Figure 15 Shell vs solid model of Notched and artificially corroded specimen shows the secondary bending affect of the solid model.

A subsequent mesh study was undertaken to determine the appropriate mesh size for the finite element analysis, yielding more precise results. A particular point within the specimen was chosen, and various mesh sizes were employed in the study (Satriawan et al., 2023). As the mesh size decreased, convergence was observed, eventually reaching a point where the graph exhibited greater stability. This initial stabilized point could be considered the ideal mesh size for the finite element analysis which is 1mm. The mesh study results for the shell and solid models of the notch and corrosion specimens are depicted in Figure 16.

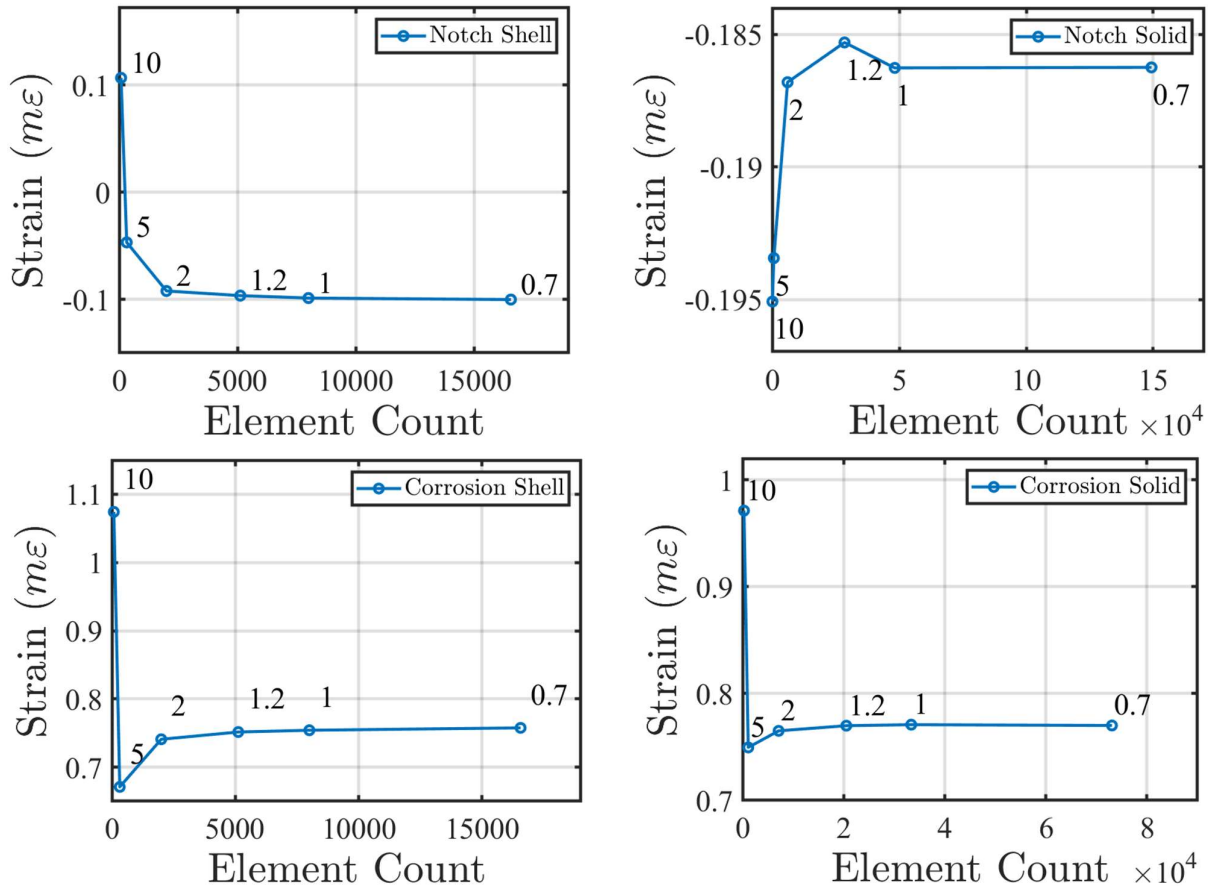


Figure 16 Mesh study graphs of shell and solid modes with different samples. [notch and corrosion]

5.3 X-Ray shell modelling

In the specific shell model being discussed, the geometric data that is derived from the radiographic image is imported and incorporated into the finite element model. This crucial step can be observed and identified as the second block within the Ansys finite element workflow in Figure 10. The x-ray shell model is depicted on the right-hand side of Figure 12. The strain comparisons of the FEM for the notched and corroded specimens are depicted

in the plots displayed in Figure 17. The obtained results exhibit a significant level of similarity, which serves as a strong indication of their accuracy.

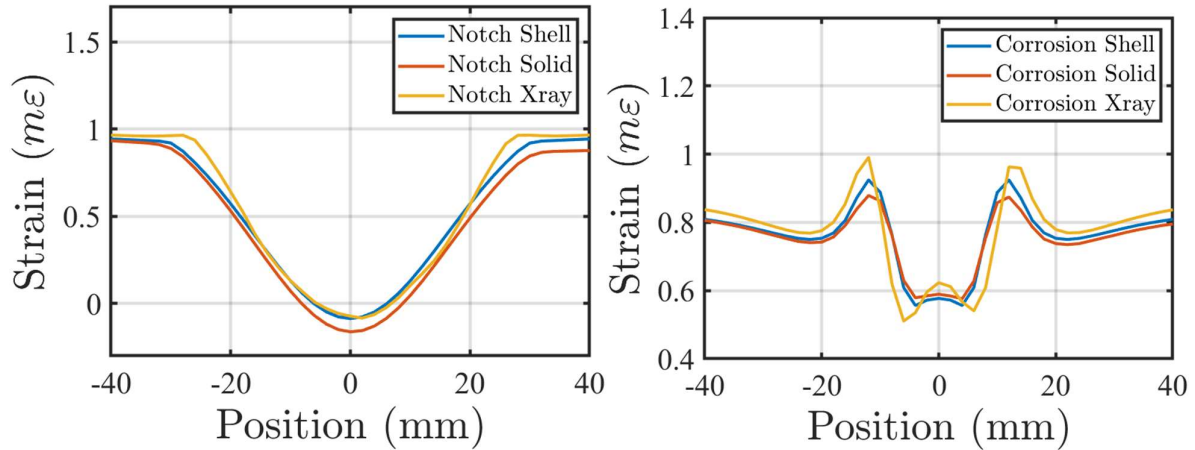


Figure 17 Shell vs solid model of Notched and artificially corroded specimen

5.4 Summary

Within this chapter, the creation of the finite element model is detailed, including the process of importing the geometry into the specimen. Furthermore, a comprehensive analysis is conducted to compare the shell model with the solid model, to determine if the shell model adequately verifies the structural integrity. Subsequently, a meticulous mesh study is performed to ascertain the optimal mesh size for the model.

6. DIC MEASUREMENTS

6.1 Process (Tensile test)

The tensile testing was conducted using an Instron 5969 (series 5700) universal testing machine as shown in Figure 18. Custom fixtures were designed specifically for the Instron to securely hold the specimen during testing as shown in Appendix E. A testing profile was created, specifying the test instructions.

The test profile included the initial application of a 1kN load at a speed of 1mm/minute. This load was applied to ensure proper specimen grip and alignment with the fixtures, allowing for the capture of an initial image using the DIC camera. The load was maintained at 1kN for 30 seconds to provide sufficient time for capturing the speckle image for strain measurements.

The load was then gradually increased up to the maximum capacity of the testing machine, reaching 45kN at a load cell speed of 0.0167mm/second. Once the load reached 45kN, it was held for 15 minutes to facilitate accurate strain measurements.

The dimensions of the tested specimen were saved within the test profile, enabling the Instron to measure specimen extension and stress values. Proper transducer settings were crucial for smooth testing, with the proportional gain set at -55dB to ensure precise real-time load measurement. The test profile was saved using the Bluehill®3 software, which controlled the Instron machine and displayed the test data on-screen.

After saving the test profile, the dog bone specimen was placed in the fixtures and secured with nuts and bolts. The distance between the load cell of the Instron and the specimen was adjusted slightly larger than the specimen size. The specimen was then mounted on the Instron, with the load cell lowered and pins inserted for proper alignment.

Once the specimen was securely mounted, the DIC machine was set up perpendicular to the surface of the dog bone specimen. Lights were positioned on both sides of the DIC machine to provide adequate illumination for the targeted specimen area. The lids of the DIC cameras were removed, and the camera height was adjusted by modifying the tripod height on which the cameras were placed. The camera lens focus was set to ensure clear visibility of the targeting area in the images for precise strain measurement. Adjustments in

lighting were made by observing the specimen in the VIC 3.0 software to avoid any appearance of red dots, which could lead to false results due to excessive exposure.

The calibration process involved selecting the calibration option in the software and placing the stereoscopic vision sensor near the specimen. By capturing images with the sensor visible and ensuring proper allocation of dot points by the cameras, approximately 40 images were used for calibration. The VIC software displayed a score for each image and a total score after calibration, with a minimal green score indicating negligible error.

The tensile test was initiated on the Instron by executing the test profile. Images were captured at the 1kN and 45kN load stages, with a 10-minute waiting period after reaching 45kN to capture the second speckle image. The first and second images were compared to obtain strain results, with the subset values set to 51 with a filter size of $m=30$ corresponds to a filter length of 61 data points. The results were exported to a .csv file for comparison with the FEM results. The strain results were also compared with the extension results calculated by the Instron. The test setup can be observed in Figure 18.

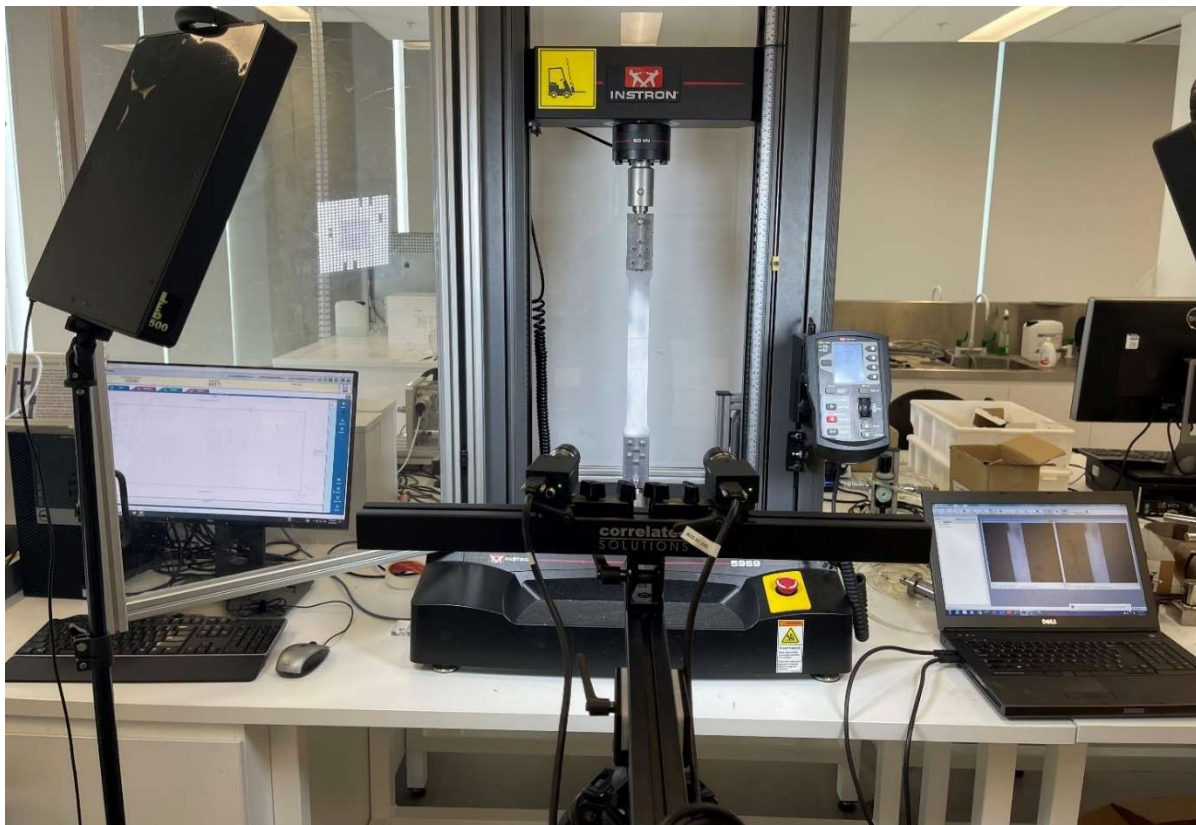


Figure 18 Tensile testing setup showing a DIC and Instron with their arrangements

6.2 Results

The figure 19 illustrates the results obtained from the Digital Image Correlation (DIC) machine for the notch section. These results include the strain values, which are clearly visible. It is important to note that the results were calculated by positioning the notch in a manner that ensures more accurate values. Specifically, the notch was oriented towards the DIC camera, as positioning it in the opposite direction would yield less precise notch values.

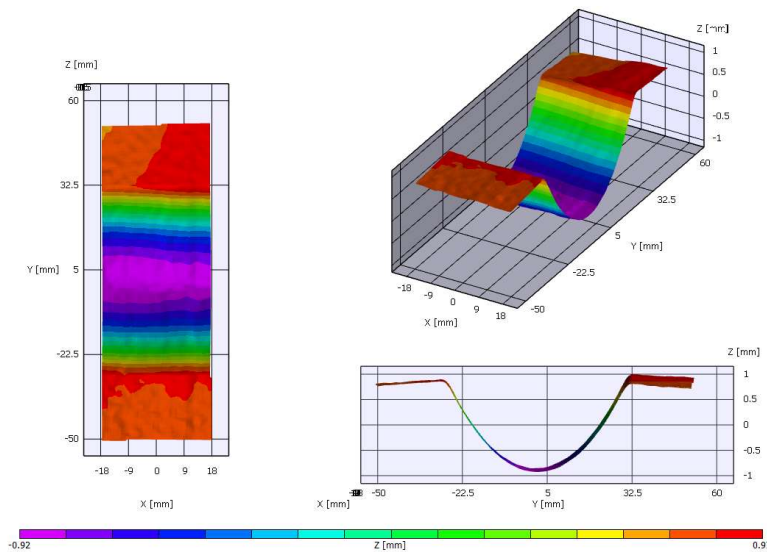


Figure 19 DIC machine results for the notch specimen facing the camera

Following the strain analysis using Digital Image Correlation (DIC), the obtained strain results were meticulously recorded and subsequently saved in the format of a comma-separated file (CSV) for further comparison with the FEA results.

6.3 Comparison

6.3.1 Results comparison and processing code MATLAB

The final version of the MATLAB code has been developed to compare the results obtained from the Finite Element Method (FEM) and the Digital Image Correlation (DIC) machine. Upon executing the code, the FEM data is selected from the collected data, while the DIC machine data is retrieved from its saved location on the computer.

Following this, a section selection prompt will appear, requiring the input of the corresponding section number in the dialogue box. Subsequently, the code will proceed to compare the results and generate various plots. The list of plots includes:

- Deformation vs position (mm).
- V Deformation (YX-axis).
- Z – Position surface plot.
- W Deformation.
- W Deformation vs Y position.
- Deformation Surface plot.
- FEA Strain Shell vs Solid.

Please take note that the preceding descriptions serve as a concise overview of the plots generated by the code, which are accessible in Appendix B.

6.3.2 Strain Comparison

After obtaining the strain values from both the Digital Image Correlation (DIC) and Finite Element Method (FEM), a comparison was performed by plotting all the strain values on the same plot. The resulting comparison of the strain results is depicted in figure 20. The trends observed in the DIC results exhibit similarities, but there are also errors present, which could potentially be attributed to noise present in the images.

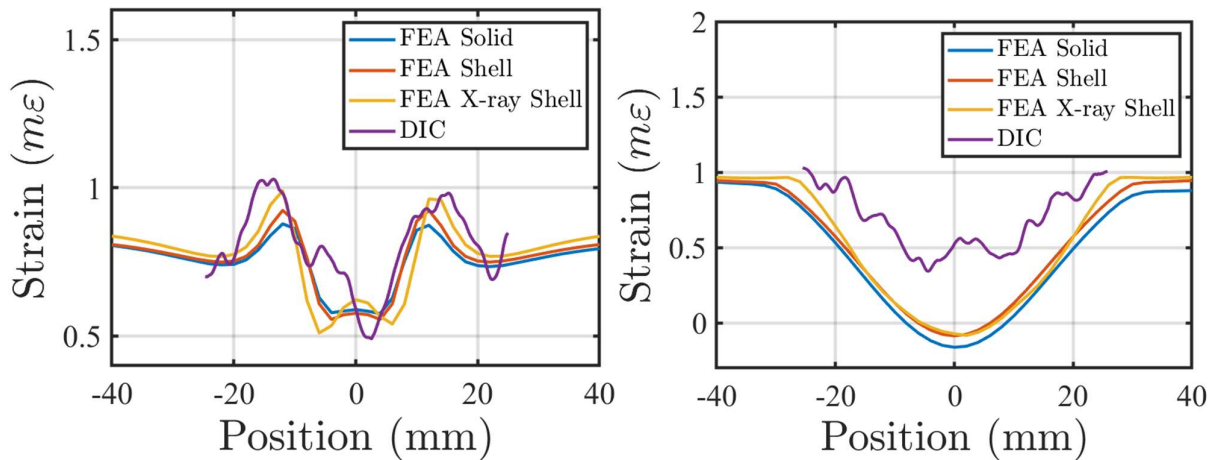


Figure 20 Strain results of notch specimen's comparison of shell, solid and real specimen (x-ray)

6.4 Discussion

The results obtained from the Digital Image Correlation (DIC) technique were obtained through manual measurements. To ensure accuracy, the DIC cameras were calibrated with

a calibration score of 0.024, indicating a high level of precision. However, despite these efforts, some data was missing during calibration, and errors were introduced due to noise.

As a consequence of these limitations, the level of strain measured using DIC was slightly lower compared to the strain measured using Finite Element Method (FEM). Nevertheless, the pattern of the strain distribution remained consistent with the FEM results.

Another contributing factor to the observed discrepancy is the relatively small strain value in the specimen. This can be attributed to the low load applied during testing, which was limited by the load capacity of the Instron machine utilized in the experiments.

7. CONCLUSION

In conclusion, the research process undertaken in this study has been developed and thoroughly analysed, leading to the identification of several areas for improvement. One of the primary areas of improvement lies in the acquisition of x-ray images. The current x-ray machine utilized for this purpose provides absorption values, which, although informative, are insufficient for accurately calculating the geometry of the specimens. This limitation becomes apparent when examining welded specimens, where the presence of different materials within the welded part results in varying levels of absorption and, subsequently, a distorted shape. However, it is worth noting that if the entire structure were composed of the same materials, the calculated thickness would exhibit a somewhat correct value. This discrepancy in absorption arises due to the non-uniform penetration of x-rays through the specimen at different angles, with this effect being particularly pronounced at the edges. To mitigate this error, the establishment of a relation between the extra absorption and the normal absorption values of the specimen is crucial, considering the specific x-ray absorption capability of the material.

Moreover, enhancing the extraction of geometric information can be achieved by incorporating the intensity of the x-rays into the geometry extraction procedure. The relationship between thickness and x-ray intensity is further detailed in chapter 4 of the study. Additionally, adjusting the settings of the x-ray machine based on the size of the specimen can contribute to more accurate results. By establishing a correlation between x-ray contrast and material thickness, considering the settings at which the x-ray image was captured, a comprehensive database can be created for the same type of material. This database would prove invaluable in saving computational time when determining the geometry. Furthermore, the contrast range of x-rays at a normal resolution, ranging from 0 to 4×10^3 , can be effectively utilized to accurately calculate the geometry of even thicker specimens.

It is important to acknowledge that the x-ray machine employed in this study was relatively outdated and designed primarily for clinical purposes. Consequently, the data obtained from this machine was limited to absorption values, lacking x-ray intensity data.

Moving forward, the next step in the research involved importing the extracted data into the shell model, a process facilitated by the use of Ansys software. Subsequently, a comparison between the shell model and the solid model was conducted to determine the suitability of

the former for testing structural integrity, given its lower computational requirements. The comparison revealed that the primary difference between the two models arises in asymmetrical specimens, where the neutral axis differs from that of the symmetrical specimens. Consequently, the shell model does not account for the bending effect observed in the solid model. To ensure accurate strain results, a mesh size of 1mm was employed.

Furthermore, strain results were obtained using a DIC machine, which measured the strain resulting from the tensile testing conducted using UTM. However, multiple iterations of strain data extraction were necessary due to data point loss and challenges in capturing all data points accurately. While there were slight variations in the level of strain between the DIC and FEA results, the overall trends in strain were consistent. It is important to note that the DIC results exhibited more errors when attempting to cover a larger area for strain measurements. Moreover, the applied load of 45kN may have been insufficient to obtain highly accurate strain results that are easily comparable. Nevertheless, the matching trends in strain between the DIC and FEA results demonstrate the feasibility of creating finite element models from radiographic imaging in metals. The initial trial conducted using steel A516 has provided valuable insights that will undoubtedly contribute to the future improvement of the process.

Additionally, the MATLAB code employed in this study can be refined to ensure its applicability to a broader range of metals. This refinement would enhance the usability and versatility of the code across different materials.

In summary, this research has opened new opportunities for radiographic imaging to reach its next level of advancement. The findings and recommendations presented in this study provide a solid foundation for further research and improvement in the field.

8. FUTURE WORK

In future work, the process will be improved by implementing a bolometer to measure the intensity of x-rays on both sides of the surface. This will provide us with precise values for the geometry. Additionally, x-rays will be taken from various angles and calibrated to obtain the exact geometry of the specimen. However, this calibration process will require more computational power.

Furthermore, the relationship between the settings of the x-ray machine and its impact on contrast will be thoroughly studied. The x-ray contrast is closely tied to the current and voltage provided. A database will be created to store the thickness values of different materials based on their corresponding RGB pixel values at specific x-ray machine settings. This database will expedite the calibration process by eliminating the need to calculate thickness values; instead, it will retrieve pre-calculated values from the database.

Moreover, a comparison between the shell model and the solid model will be conducted using the extracted geometry data from the radiographic image. This analysis will reveal the positive and negative aspects of the shell model. Based on these findings, a decision can be made regarding the suitability of the shell model for testing the structural integrity of the structure.

Furthermore, there is potential for the automation and standardization of this process, making it the first of its kind to be developed for metals and standardized. While similar work has been conducted in the medical field for a considerable period, there is still a lack of a universally accepted standard process.

BIBLIOGRAPHY

Amani, Y., Dancette, S., Maire, E., Adrien, J., & Lachambre, J. (2018). *Two-scale tomography based finite element modelling of plasticity and damage in aluminium foams*. Materials, 11(10), 1984.

Auenhammer, R. M., Mikkelsen, L. P., Asp, L. E., & Blinzler, B. J. (2021). *Automated X-ray computer tomography segmentation method for finite element analysis of non-crimp fabric reinforced composites*. Composite Structures, 256, 113136.

Bayu, A., Harun, A. R. R., & Firliyani, R. N. (2018). *Measurement of metal thickness using X-ray computed radiography*.

Bell, R., (1984). *Field Radiography-Images from the past*. Materials Evaluation, 42(7), 849-851.

Berger, H. (1995). *100 years of X-rays: industrial use of NDT and the role of ASNT*. Materials evaluation, 53(11), 1253-1260.

Blair Henry, E. (1989). *The role of non-destructive testing in the production of pipe and tubing*. Materials evaluation, 47(6), 714-724.

Briggs, C. W. (1976). *Developments in gamma ray radiography 1928 to 1941. II. A history of non-destructive testing*. Steel Founders Society of America, Cleveland.

Chen, X., & Liu, Y. (2018). *Finite element modelling and simulation with ANSYS Workbench*. CRC press.

Davis, R. S. (1989). *Early development of process automation with nucleonic measurement gages*. Materials Evaluation;(USA), 47(10).

Dorobantu, V. (2004). *X rays linear attenuation coefficient in steel. I. Thickness dependence*. Journal of Non-destructive Testing, 9(12).

Dwivedi, S. K., Vishwakarma, M., & Soni, A. (2018). *Advances and researches on non-destructive testing: A review*. Materials Today: Proceedings, 5(2), 3690-3698.

Farina, E., Gastaldi, D., Bains, F., Vernè, E., Massera, J., Orlygsson, G., & Vena, P. (2021). *Micro computed tomography based finite element models for elastic and strength properties of 3D printed glass scaffolds*. *Acta Mechanica Sinica*, 37, 292-306.

Fink, W. L., & Archer, R. S. (1929). *Radiography as a tool in the metal industry*. *Transact Am Soc Steel Treating*, 16, 551-599.

H. Bossi, R. and Cordon, T. (2019). *Non-destructive Testing Handbook*, Vol. 3 Radiographic Testing (RT). Fourth ed. ASNT, pp.3–36.

Hagemaijer, D. J. (1985). *Aerospace radiography: The last three decades*. *Materials evaluation*, 43(10), 1262-1283.

Halmshaw, R. (1988) "A History of Industrial Radiography in the UK." *British Journal of Non-Destructive Testing*. Vol. 30, No. 5. Northampton, United Kingdom: British Institute of Non-Destructive Testing (September 1988): p 325-331.

Heidt, H. *Private communication*. Weimar, Germany (1994).

Hovland, H. (1985). *Developments in field X-radiography 1931-1962*. *Materials evaluation*, 43(11), 1386-1390.

Huang, W., Zhang, X., & Yin, Y. (2016). *An image-based finite element approach for simulating viscoelastic response of asphalt mixture*. *Advances in Materials Science and Engineering*, 2016.

Huber, J. A., Broman, O., Ekevad, M., Oja, J., & Hansson, L. (2022). *A method for generating finite element models of wood boards from X-ray computed tomography scans*. *Computers & Structures*, 260, 106702.

Itoh, G. (1982). *A review of the history of non-destructive testing in Japan*. *Materials Evaluation*, 40, 1138.

Jahangir, S., Mohammadi, A., Mononen, M. E., Hirvasniemi, J., Suomalainen, J. S., Saarakkala, S., ... & Tanska, P. (2022). *Rapid X-Ray-Based 3-D Finite Element Modelling of Medial Knee Joint Cartilage Biomechanics During Walking*. *Annals of Biomedical Engineering*, 50(6), 666-679.

Jespersen, K. M., Asp, L. E., Hosoi, A., Kawada, H., & Mikkelsen, L. P. (2018). *X-ray tomography based finite element modelling of non-crimp fabric-based fibre composite*. In 18th European conference on composite materials, Athens, Greece.

Konnik, M., Ahmadi, B., May, N., Favata, J., Shahbazi, Z., Shahbazmohamadi, S., & Tavousi, P. (2021). *Training AI-based feature extraction algorithms, for micro-CT images, using synthesized data*. *Journal of Non-destructive Evaluation*, 40, 1-13.

Krüger, G., & Weeber, H. (1983). *Entwicklung der technischen Durchstrahlungsprüfung in Deutschland*.

Lester, H.H. (1922) "*Radiography of Metals*." Army Ordnance. Vol. 3 (1922): p 210-215

Lester, H.H. (1969) "*X-Ray Examination of Steel Castings*." *Chemical and Metallurgical Engineering*. Vol. 28, No. 6. New York, NY: McGraw-Hill (February 7, 1923). Reprint in Wenk, S.A. "The Past Perfect." *Materials Evaluation*. Vol. 27, No. 1. Columbus, OH: American Society for Non-destructive Testing (January 1969): p 1-10

Liu, W. K., Li, S., & Park, H. S. (2022). *Eighty years of the finite element method: Birth, evolution, and future*. *Archives of Computational Methods in Engineering*, 29(6), 4431-4453.

Loginow, A. W., & Phelps, E. H. (1975). *Steels for seamless hydrogen pressure vessels*. *Corrosion*, 31(11), 404-412.

Lutts, C.G. (1954) "*Ten Years' Cooperation between the Society for Non-destructive Testing and the American Society for Metals*." *Non-destructive Testing*. Vol. 12, No. 1. Columbus, OH: American Society for Non-destructive Testing (January-February 1954): p 31-36.

Moore, P. (1985). *A Gamma-Radiographer of pipeline welds*. *Materials Evaluation*, 43(9), 1084.

Morgan, K.Z. (1971) "*History of Radiation Protection*." *Materials Evaluation*. Vol. 29, No. 3. Columbus, OH: American Society for Non-destructive Testing (March 1971): p 19A–20A, 22A, 24A–27A, 32A.

Norton, M. (1986). *The founder of industrial radiography-personal notes on Lester, Horace, H. Materials Evaluation*, 44(4), 408-410.

O'Connor, D.T., and B.G. Cunningham. (1949) "*Installation of the Flexible 10 MeV Betatron.*" *Non-Destructive Testing*. Vol. 7, No. 4. Columbus, OH: American Society for Non-destructive Testing (Spring 1949): p 20-23.

Park, H. S., Hwang, D., & Seo, J. K. (2015). *Metal artifact reduction for polychromatic X-ray CT based on a beam-hardening corrector*. *IEEE transactions on medical imaging*, 35(2), 480-487.

Peng, C., Liu, C., Liao, Z., Yang, B., Tang, L., Yang, L., & Jiang, Z. (2022). *Automatic 3D image based finite element modelling for metallic foams and accuracy verification of digital volume correlation*. *International Journal of Mechanical Sciences*, 235, 107715.

Razmjoo, A. (2013). *Application of image processing and finite element analysis in modelling chloride diffusion in concrete* (Doctoral dissertation, Clemson University).

Rummel, W. D. (2013). *Quest for Reliable Non-destructive Testing*. *Materials Evaluation*, 71(5).

Satriawan, C. Y. G., Harwijayanti, W., Ridwan, R., Prabowo, A. R., Fajri, A., Cho, J. H., & Do, Q. T. (2023). *Nonlinear analysis of an idealized I-beam member: An investigation of mesh size on the structural behaviors using FE approach*. *Procedia Structural Integrity*, 48, 50-57.

Straw, R. (1984). *If I Had a Million!*, *the Early Years of High-Energy Radiography*. *Mater. Eval.*, 42(3), 264-268.

Straw, R. (1984). *Voices in the air- The early days of aircraft NDT*. *Materials Evaluation*.

Straw, R. (1984) "*If I Had Ten Million!*" *A Man and His Laboratory.*" *Materials Evaluation*. Vol. 42, No. 4. Columbus, OH: American Society for Non-destructive Testing (April 1984): p 374-375.

Turner, M. J., Clough, R. W., Martin, H. C., & Topp, L. J. (1956). *Stiffness and deflection analysis of complex structures*. *journal of the Aeronautical Sciences*, 23(9), 805-823.

Wai, C. M., Rivai, A., & Bapokutty, O. (2013, December). *Modelling optimization involving different types of elements in finite element analysis*. In IOP Conference Series: Materials Science and Engineering (Vol. 50, No. 1, p. 012036). IOP Publishing.

Wang, D., & Chen, X. (2021). *Closed-loop high-fidelity simulation integrating finite element modelling with feedback controls in additive manufacturing*. Journal of Dynamic Systems, Measurement, and Control, 143(2), 021006.

Wenk, S.A. (1969) "*The Past Perfect.*" Materials Evaluation. Vol. 27, No. 1. Columbus, OH: American Society for Non-destructive Testing (January 1969): p 1-10.

Zienkiewicz, O. C. (2004). *The birth of the finite element method and of computational mechanics*. International journal for numerical methods in engineering, 60(1), 3-10.

APPENDICES

A. RESULTS: Geometry extraction from the radiographic images

1. Notched Specimen

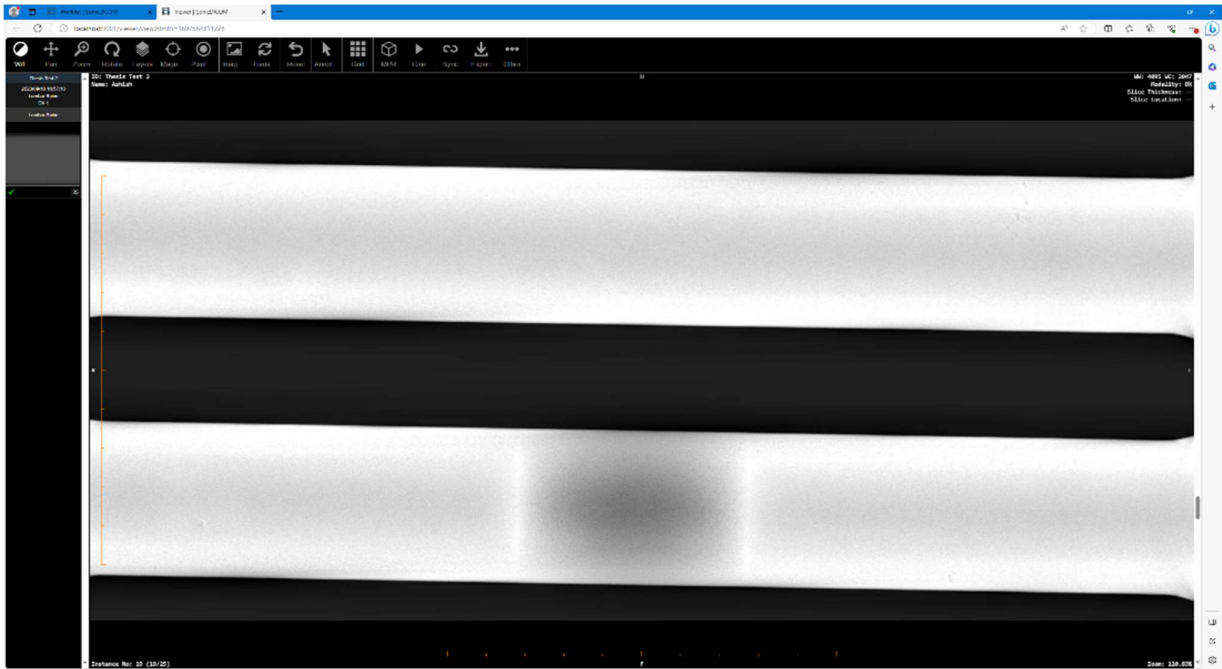


Figure 21 Raw X-ray image of a normal and a Nitched dog bone specimen viewed in a Sonic DiacomViewer

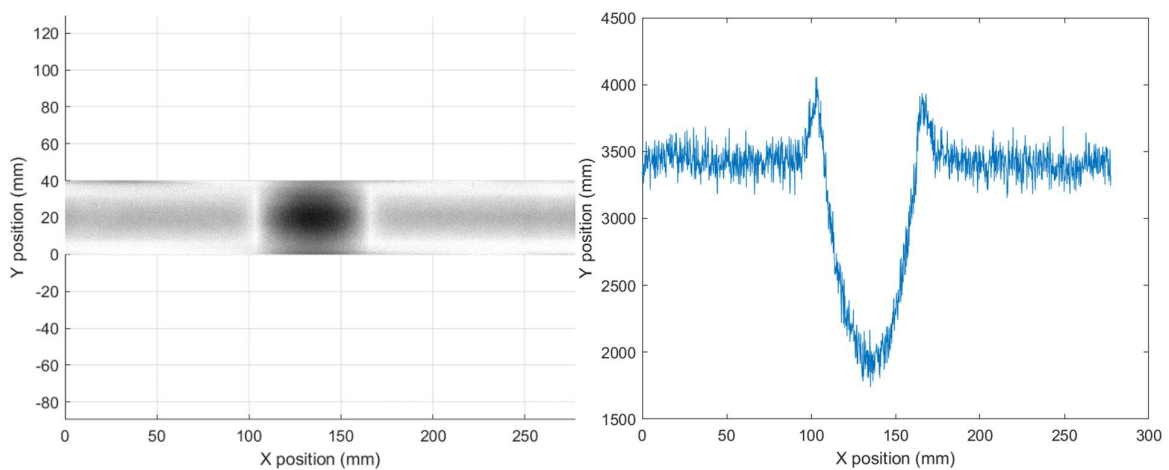


Figure 22 Targeted specimen area (left) and the extracted centreline x-ray contrast data (right)

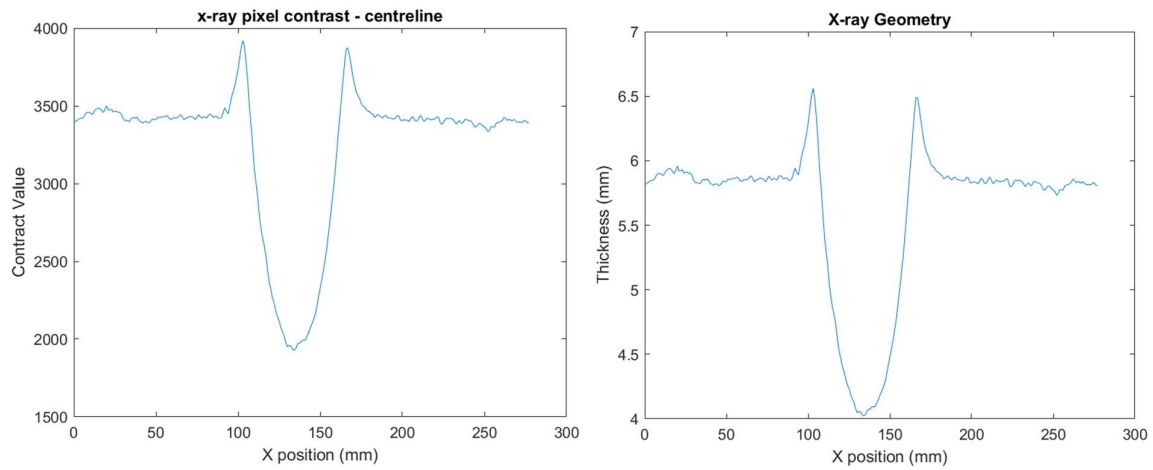


Figure 23 Smoothened contrast values of the x-ray (left) and the relation to the geometry after calculating the geometry (right)

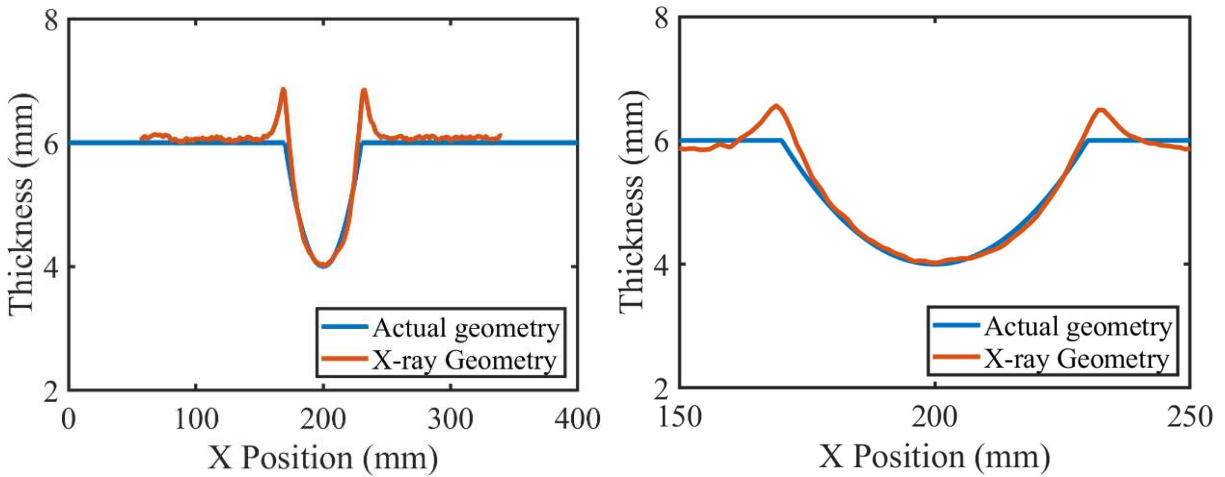


Figure 24 Comparison of the extracted geometry with the actual geometry of the specimen

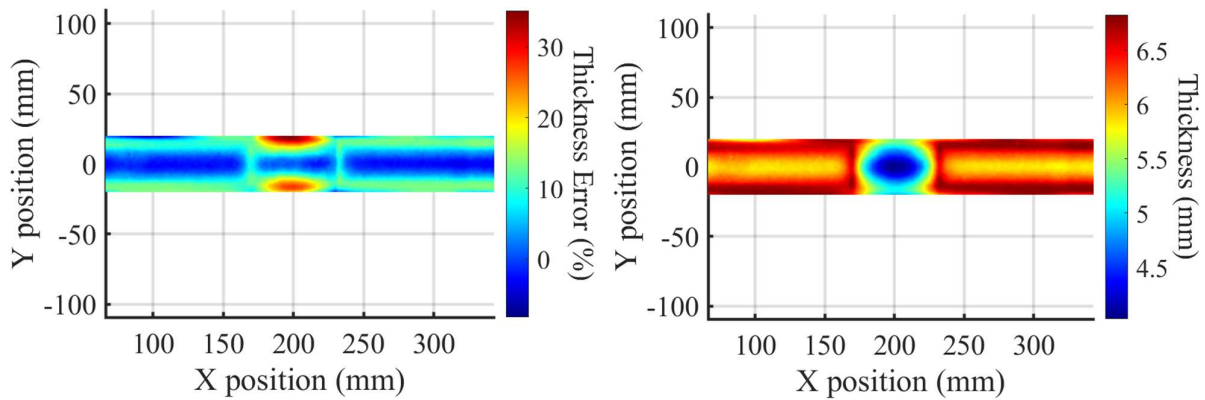


Figure 25 The error plot observed after comparing the extracted geometry with the actual geometry (left) and the geometry plot of the specimen (right)

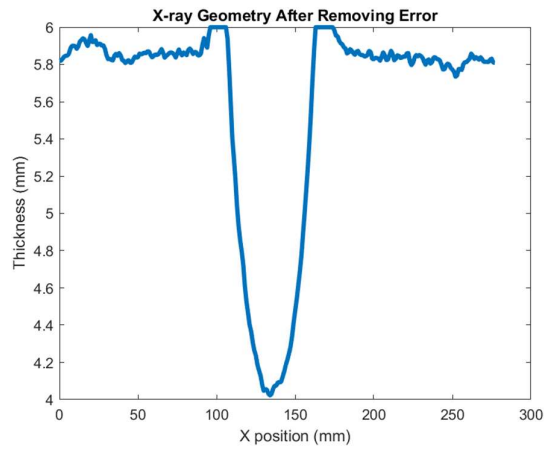


Figure 26 Improved geometry values after removing the errors i.e., >6mm

2. Corrosion Specimen

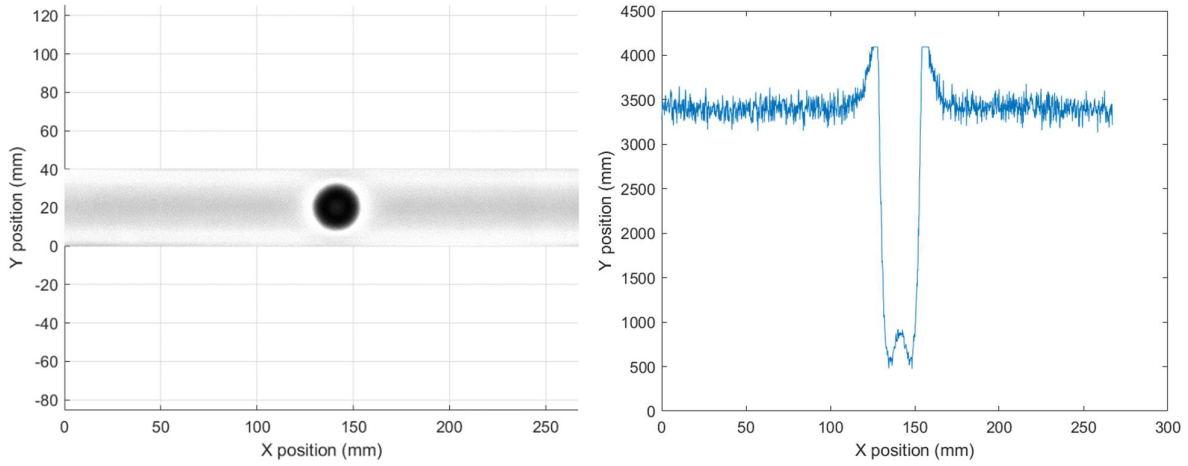


Figure 27 Targeted specimen area (left) and the extracted centreline x-ray contrast data (right)

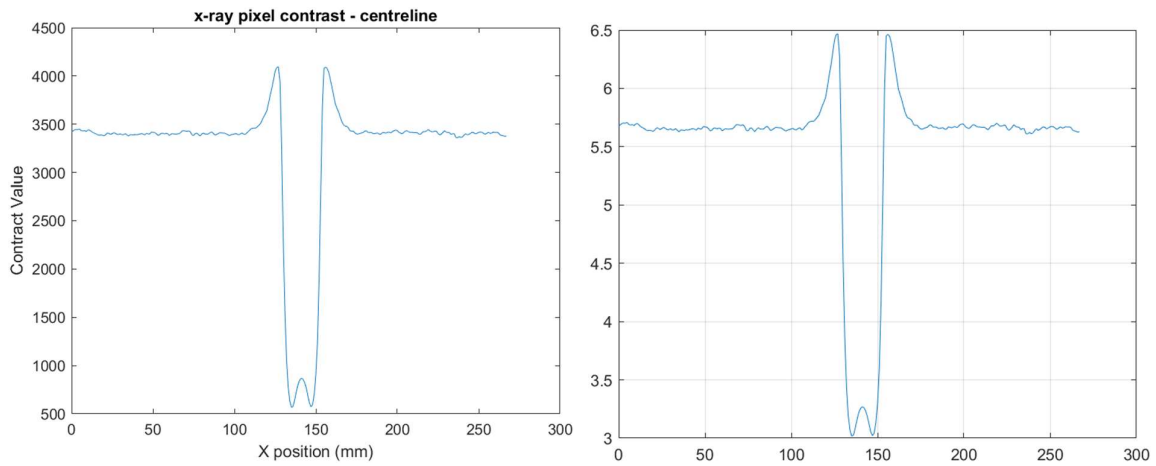


Figure 28 Smoothened constrast values of the x-ray (left) and the relation to the geometry after calculating the geometry (right)

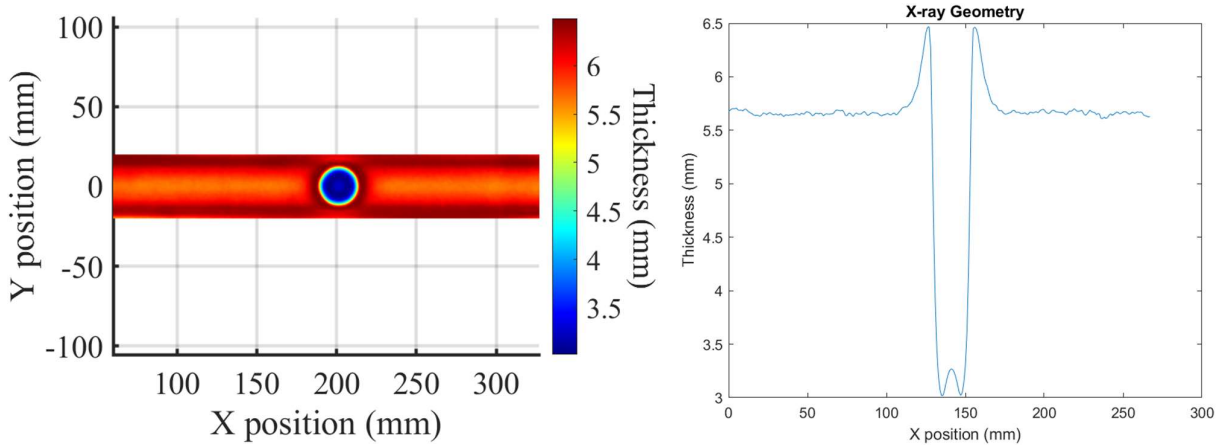


Figure 29 Geometry distribution (left) compared with the centreline geometry (right)

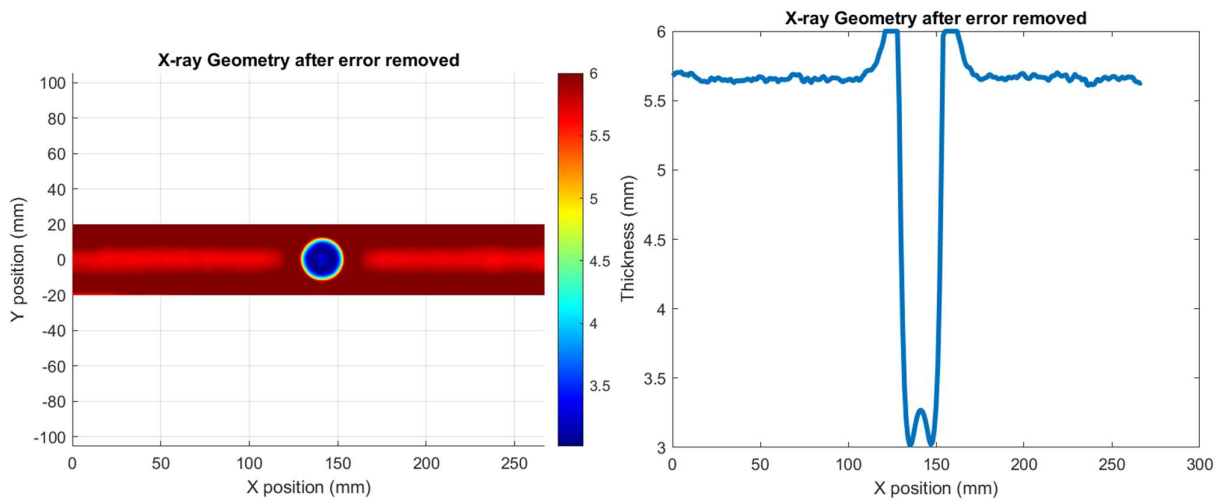


Figure 30 Improved Geometry distribution (left) compared with the centreline geometry (right)

3. Welded Specimen

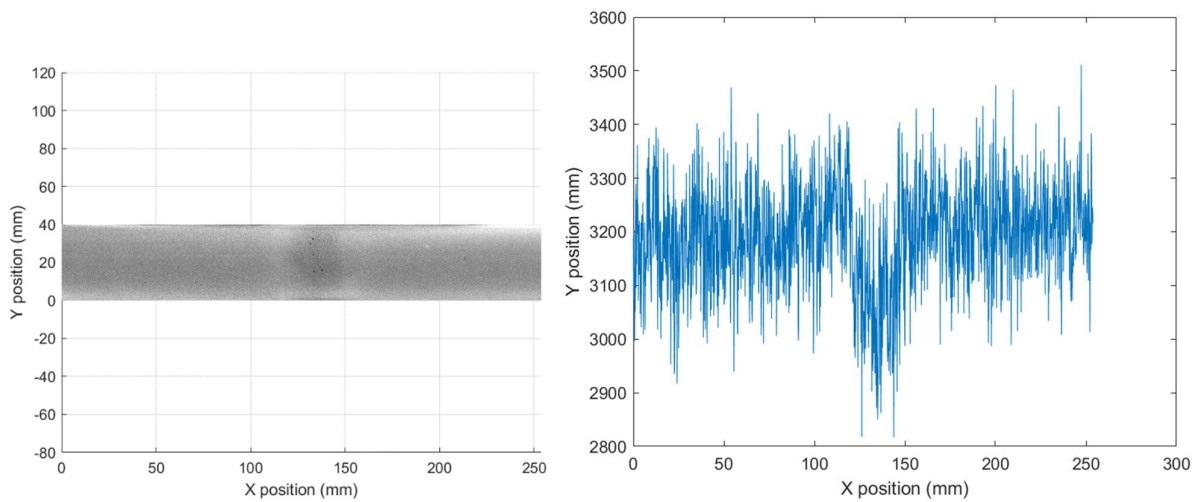


Figure 31 Targeted specimen area (left) and the extracted centreline x-ray contrast data (right)

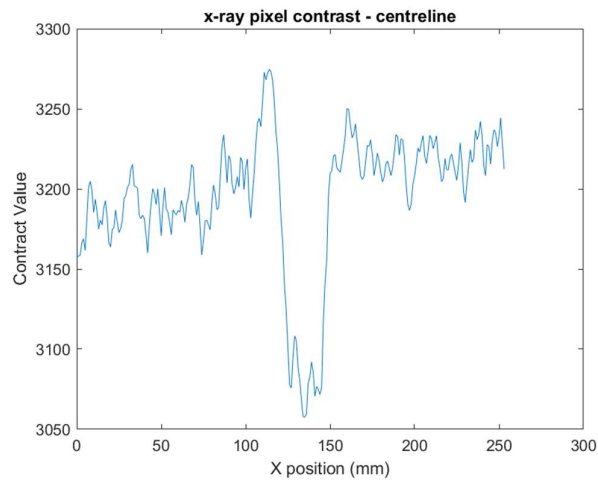


Figure 32 Smoothened constrast values of the x-ray

4. Middle Cut Specimen

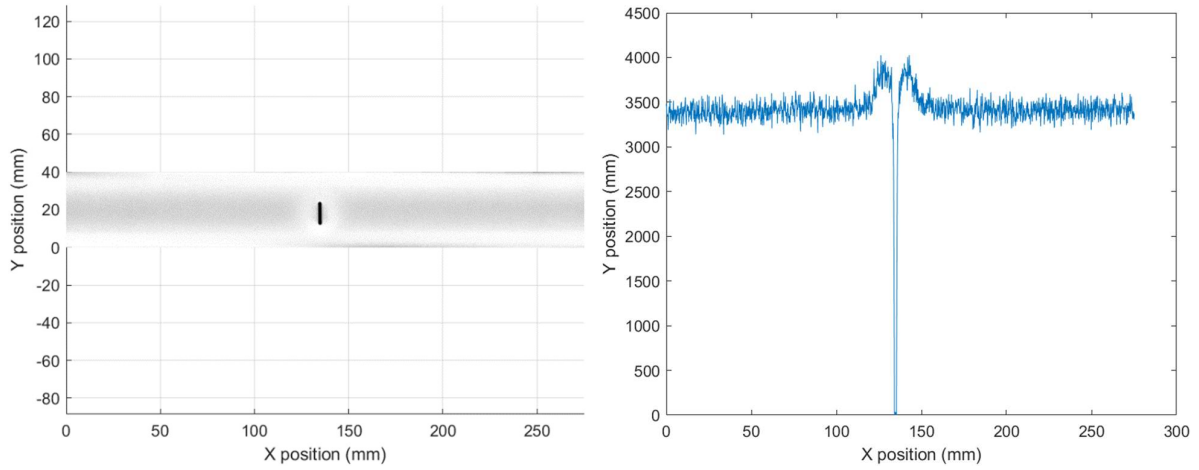


Figure 33 Targeted specimen area (left) and the extracted centreline x-ray constrast data (right)

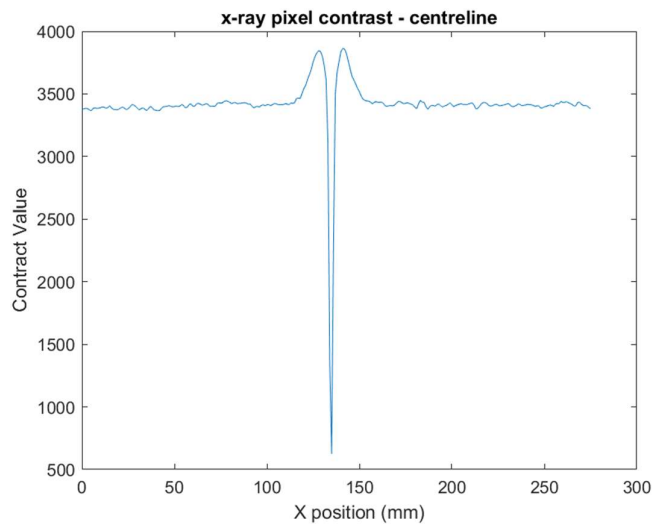


Figure 34 Smoothened constrast values of the x-ray

B. Results Comparison plots [MATLAB Script]

1. Corrosion Specimen

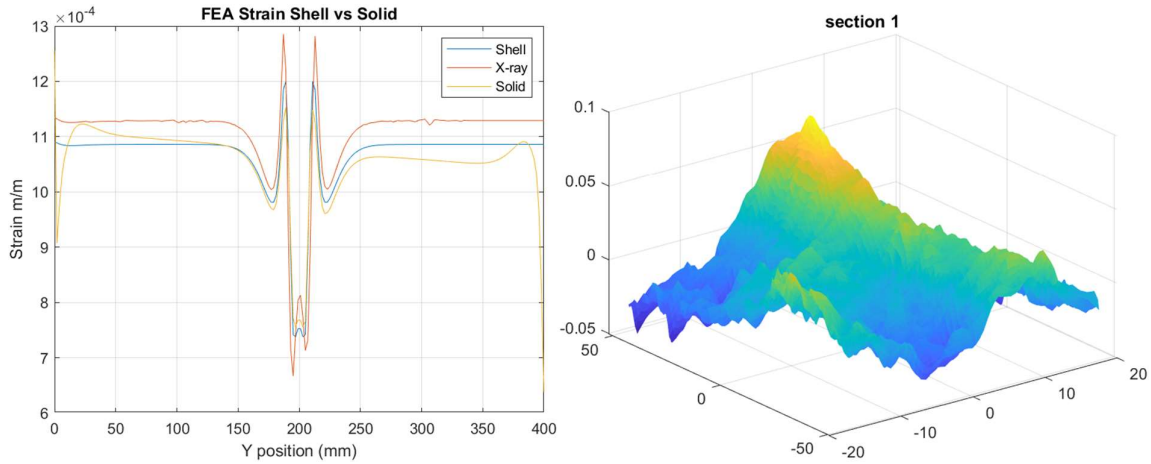


Figure 35 Comparison of shell, solid and X-ray finite element models (left) and the strain plot received from DIC machine (right)

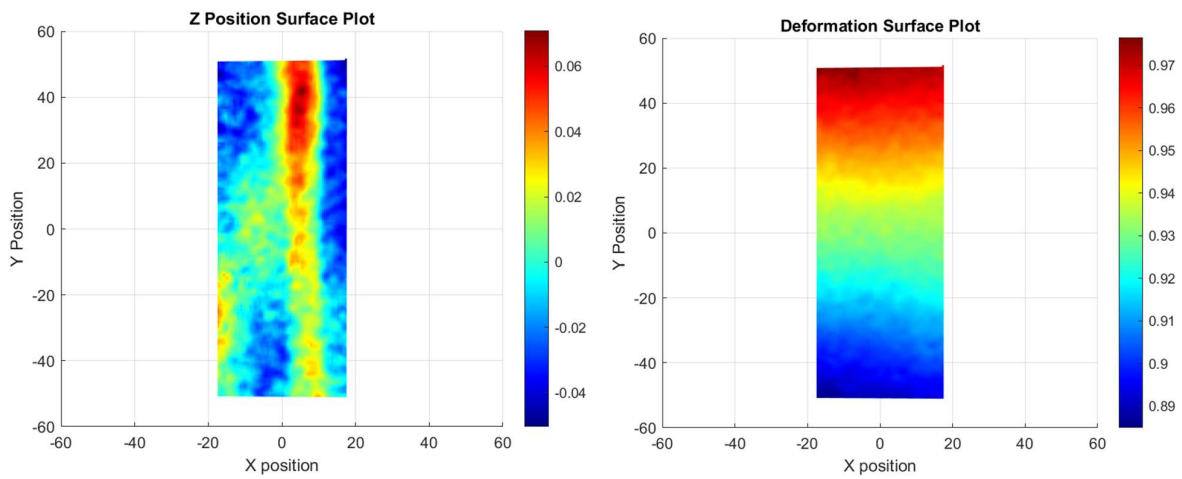


Figure 36 Z position surface plot (left) and the deformation surface plot (right)

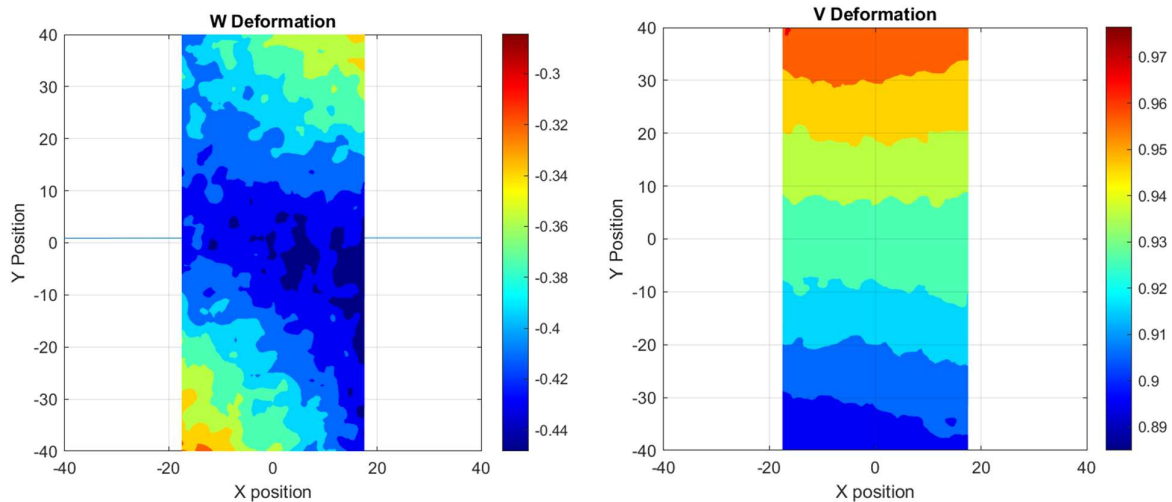


Figure 37 Deformation plots

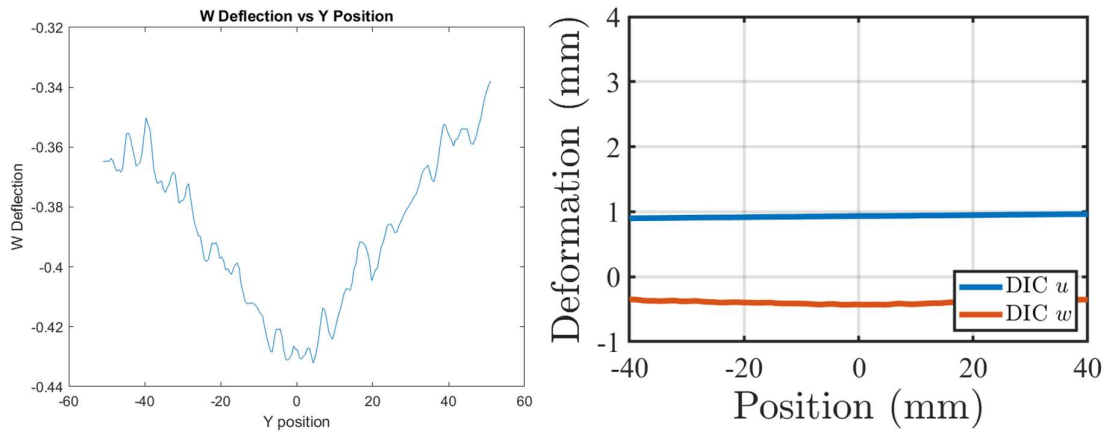


Figure 38 W deformation vs Y position plot (left) and Deformation vs position plot of the initial position before and final position after (right)

2. Notched Specimen

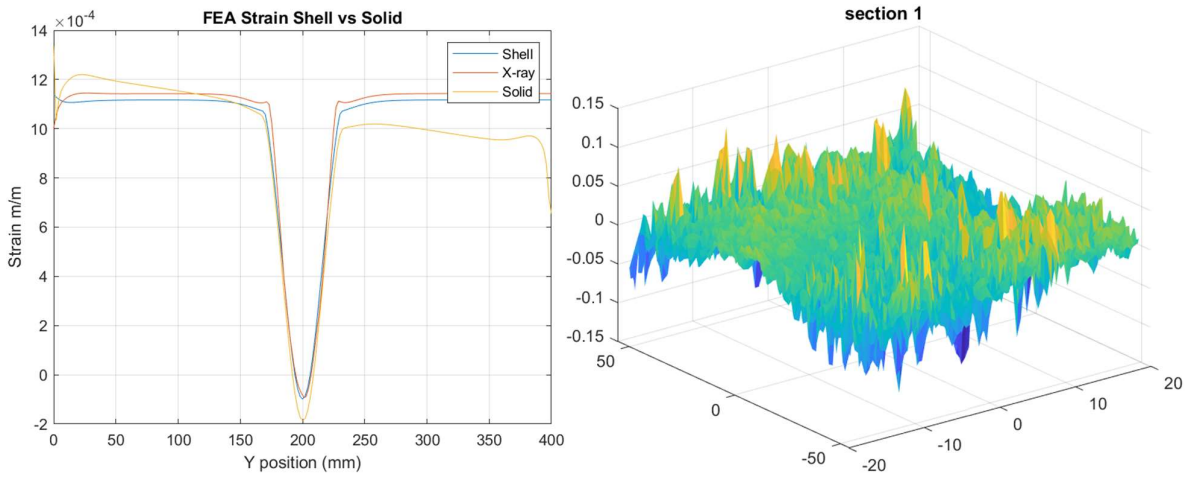


Figure 39 Comparison of shell, solid and X-ray finite element models (left) and the strain plot received from DIC machine (right)

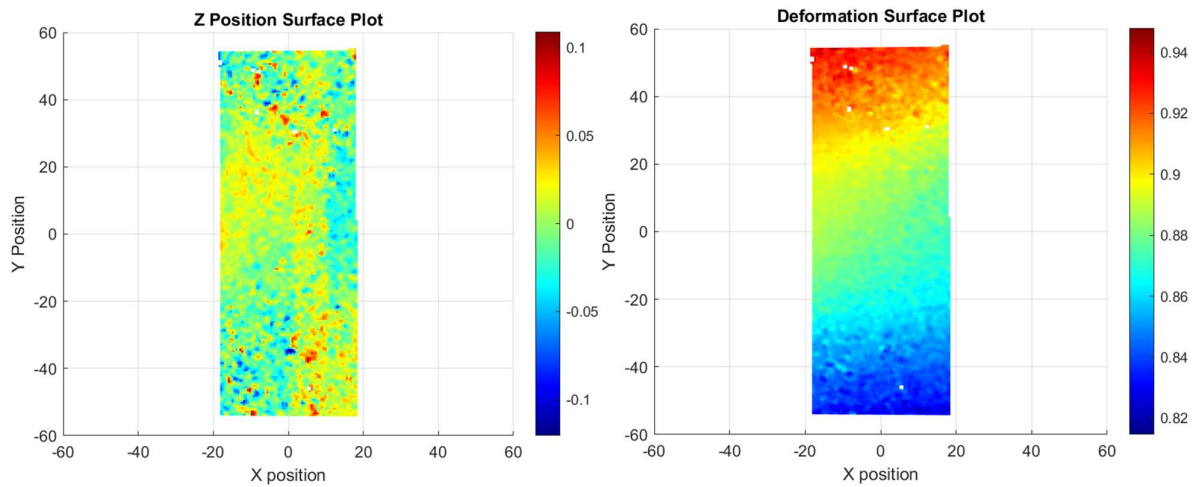


Figure 40 Z position surface plot (left) and the deformation surface plot (right)

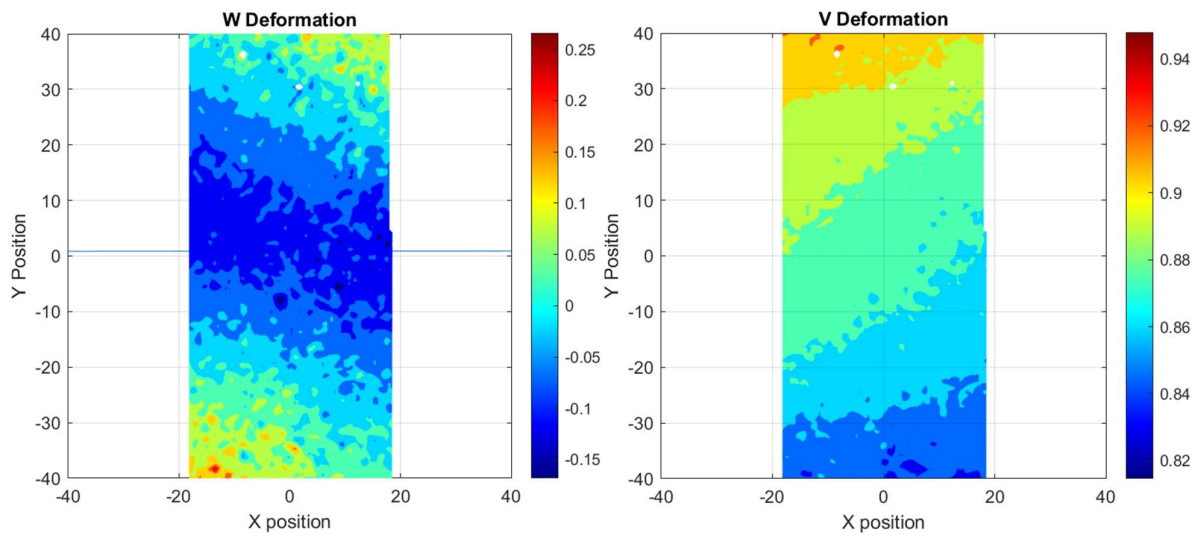


Figure 41 Deformation plots

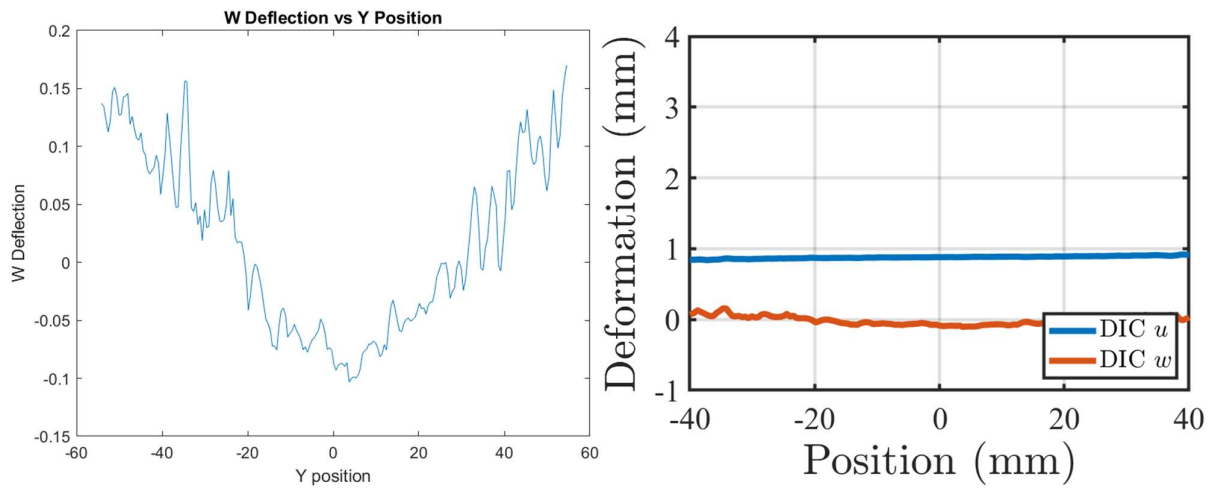


Figure 42 W deflection vs Y position plot (left) and Deformation vs position plot of the initial position before and final position after (right)

C. Risk Assessment



RISK ASSESSMENT FORM



Risk Assessment No.	TPP01
Reference to SWP/SWMS No.	001

List identified hazards and detail measures taken to eliminate / minimise the risks:
(boxes on this form will expand to fit text)

College/Portfolio	Science and Engineering	Area/Unit	Flinders University	Location	Tonsley	Area/Unit Manager	Dr Stuart Wildy
Task/Procedure	X-ray and Tensile Testing of Steel Samples	Workers consulted / involved	Dr Stuart Wildy	Date	30/03/2023	Review Date	31/03/2023

Identified Hazard before controls			Risk Assessment			Risk Controls	Residual risk			Implementation
No.	Description	Consequences	Likelihood	Risk Measure (see matrix)	Control measures	Consequences (see matrix)	Likelihood	Risk Measure (see matrix)	Date controls implemented / reviewed	
1	X-rays exposure may cause DNA modification which may leads to cancer.	Catastrophic	Unlikely	High	X-ray machine should be operated by trained person. Make sure you wear proper PPE when performing the operation and/or leave the room when imaging specimens.	Catastrophic	Highly Unlikely	Medium	30/03/2023	
2	Exposure to X-rays may cause radiation burn.	First Aid	Possible	Medium	X-ray machine should be operated by trained person. Make sure you wear proper PPE when performing the operation and/or leave the room when imaging specimens.	First Aid	Highly Unlikely	Low	30/03/2023	
3	Risks of impact, crushing (between a tester's moving component and its immovable frame).	First Aid	Possible	Medium	Only trained operators to use the machine. Safety glasses much be worn at all time during the experiment.	First Aid	Highly Unlikely	Low	30/03/2023	
4	Flying debris may cause injury.	Major Injury	Highly Unlikely	Medium	Wear clear safety glasses with side shields.	First Aid	Highly Unlikely	Low	30/03/2023	
5	Injury due to slips, trips and falls.	First Aid	Unlikely	Low	Inspect work area, walk around Instron looking for debris and ensure proper lighting.	First Aid	Highly Unlikely	Low	30/03/2023	

Review the risk measured, and the controls implemented are still relevant and effective, then please select one of the following:

- A The assessment reveals that the potential risk to health and safety from the use of the plant/equipment/procedure is not currently significant.
- B The assessment reveals that the potential risk to health and safety from the use of the plant/equipment/procedure is significant. However controls are in place that reduce risk as low as is reasonably practicable.

Note: If the risk level is still Extreme/High after controls are in place, then cease the activity, identify and implement further controls and consult with your manager/supervisor until the risk is reduced as low as reasonably practicable.

To be completed by Supervisor

Review of control measures

I am satisfied that appropriate controls are in place, still relevant and effective and the risk level is as low as reasonably practicable - Yes *No (*if no, you must do another Risk Assessment.)

Supervisor signature: **Stuart Wildy** Digitally signed by Stuart Wildy
Date: 2023.04.01 06:13:07 +10'30'

Date: **01/04/2023**

HOW TO ASSESS THE RISK

Step A - Consider the consequences		Step B - Consider the likelihood	
For each hazard, consider the consequences if something happens. Consider what could reasonably have happened, as well as what actually happened (if there was an accident/incident). Look at the descriptions below and choose the most suitable consequence below.		How likely is it that something will happen as a result of the hazard? Choose the most suitable likelihood below.	
Consequence	Description	Likelihood	Description
Catastrophic	May cause death, or permanent disability, and/or permanent ill health	Very likely	Expected to occur in most circumstances
Major	Severe injury or illness	Likely	Will probably occur in most circumstances
Minor	Minor (usually reversible) injury or illness resulting in days off work	Possible	Might occur occasionally
First Aid	First aid level medical treatment	Unlikely	Could happen at some time
Negligible	No treatment required	Highly unlikely	May happen only in exceptional circumstances

Step C – Calculate the Risk Level

1. Take the Step A rating and select the correct line in the matrix below.
2. Take the Step B rating and select the correct column in the matrix below.
3. Circle the risk level where the two ratings interse in the matrix below.

Risk level =

Risk Matrix

Consequence	Likelihood				
	Very likely	Likely	Possible	Unlikely	Highly unlikely
Catastrophic	Extreme	High	High	High	Medium
Major injury	High	High	High	Medium	Medium
Minor injury	High	Medium	Medium	Medium	Medium
First aid	Medium	Medium	Medium	Low	Low
Negligible	Medium	Medium	Low	Low	Low

Prioritising Hazards		
Risk Level	Priority	Action
Extreme	1	<ul style="list-style-type: none"> * Cease task/activity immediately; * Implement short term safety controls to make the situation safe; * Notify supervisor/manager and assess activity; and * Do not proceed with task/activity until corrective action has been implemented, and reviewed and approved by the relevant Vice-President and Executive Dean of College or Portfolio Head.
High	2	<ul style="list-style-type: none"> * Implement short term safety controls to make the situation safe; * Notify supervisor/manager and assess activity; and * Do not proceed with task/activity until corrective action has been implemented, and reviewed and approved by the relevant Vice-President and Executive Dean of College or Portfolio Head.
Medium	3	<ul style="list-style-type: none"> * Implement short term safety controls. * Notify supervisor/manager and assess activity. * Implement control measures.
Low	4	<ul style="list-style-type: none"> * Notify supervisor/manager and assess activity. * Implement control measures.

Control Hierarchy	
Elimination	<i>Remove hazard</i>
Substitution	<i>Use a less hazardous alternative</i>
Isolation	<i>Eg Restrict access, use in a closed container, fume cabinet</i>
Engineering	<i>Eg Trolleys to move loads, guards on machinery, fume cupboard</i>
Administration	<i>Eg Training, Safe Work Procedure, signage</i>
PPE - Personal Protective Equipment	<i>Eg Gloves, respirator, safety glasses</i>

See [WHS Risk Management Procedure](#) for further details

D. MATLAB Codes

1. Extract pixel RGB Values

```
A = imread('11.jpg');
imshow(A);
imtool(A);
% disp("Pixel values:");
% disp(A);
```

2. Mesh Study

```
clc
close all
clear all

Shell_Mesh = [10 5 2 1.2
1 0.7];
Shell_Elements = [80 320 2000 5120
8000 16555];
Notch_Shell_Strain = [1.0656e-004 -4.6945e-005 -9.2272e-005 -9.6603e-005
-9.887e-005 -1.0029e-004];
Corr_Shell_Strain = [1.0741e-003 6.7107e-004 7.4087e-004 7.5151e-004
7.541e-004 7.5758e-004];

Solid_Mesh = [10 5 2 1.2
1 0.7];
Notch_Solid_Elements = [92 656 6060 28475
48240 149292];
Notch_Solid_Strain = [-1.9508e-004 -1.9344e-004 -1.868e-004 -1.853e-004
-1.8626e-004 -1.8624e-004];
Corr_Solid_Elements = [292 1132 7142 20530
33367 73072];
Corr_Solid_Strain = [9.7118e-004 7.4959e-004 7.6511e-004 7.6994e-004
7.7089e-004 7.7013e-004];

%%

figure
plot(Shell_Elements,Notch_Shell_Strain*10^3,'o-','LineWidth', 2); hold on;

var = axis
for i = 1:length(Shell_Mesh)

text(Shell_Elements(i)+400,Notch_Shell_Strain(i)*10^3+var(4)*0.1,num2str(Shell_Mesh(i))
,'fontsize',20,'FontName','Times New Roman')
end

axis([var(1) 19000 var(3) var(4)*1.15])

ax = gca;
ax.FontName = 'Times New Roman';
ax.FontSize = 20;
ax.LineWidth = 2;
% ax.XTick = [-50,-40,-30,-20,-10,0,10,20];
```

```

xlabel('Element Count','FontName','Times New
Roman','FontSize',28,'Interpreter','Latex')
ylabel('Strain ( $\varepsilon$ )','FontName','Times New
Roman','FontSize',28,'Interpreter','Latex')
legend('Notch Shell','location','northeast','FontName','Times New
Roman','FontSize',16,'Interpreter','Latex')
grid

%%

figure
plot(Shell_Elements,Corr_Shell_Strain*10^3,'o-','LineWidth', 2)

var = axis
for i = 1:length(Shell_Mesh)

text(Shell_Elements(i)+400,Corr_Shell_Strain(i)*10^3+0.05,num2str(Shell_Mesh(i)),'fontsi
ze',20,'FontName','Times New Roman')
end

axis([var(1) 19000 var(3) var(4)+0.05])

ax = gca;
ax.FontName = 'Times New Roman';
ax.FontSize = 20;
ax.LineWidth = 2;
% ax.XTick = [-50,-40,-30,-20,-10,0,10,20];

xlabel('Element Count','FontName','Times New
Roman','FontSize',28,'Interpreter','Latex')
ylabel('Strain ( $\varepsilon$ )','FontName','Times New
Roman','FontSize',28,'Interpreter','Latex')
legend('Corrosion Shell','location','northeast','FontName','Times New
Roman','FontSize',16,'Interpreter','Latex')
grid

%%

figure
plot(Corr_Solid_Elements,Corr_Solid_Strain*10^3,'o-','LineWidth', 2)

var = axis
for i = 1:length(Solid_Mesh)

text(Corr_Solid_Elements(i)+400,Corr_Solid_Strain(i)*10^3+0.02,num2str(Solid_Mesh(i)),'
fontsize',20,'FontName','Times New Roman')
end

axis([var(1) 90000 var(3) var(4)+0.02])

ax = gca;
ax.FontName = 'Times New Roman';
ax.FontSize = 20;
ax.LineWidth = 2;
% ax.XTick = [-50,-40,-30,-20,-10,0,10,20];

xlabel('Element Count','FontName','Times New
Roman','FontSize',28,'Interpreter','Latex')
ylabel('Strain ( $\varepsilon$ )','FontName','Times New
Roman','FontSize',28,'Interpreter','Latex')

```



```

legend('Corrosion Solid','location','northeast','FontName','Times New
Roman','FontSize',16,'Interpreter','Latex')
grid

%%

figure
plot(Notch_Solid_Elements,Notch_Solid_Strain*10^3,'o-','LineWidth', 2); hold on;

var = axis
for i = 1:length(Solid_Mesh)
    text(Notch_Solid_Elements(i)+400,Notch_Solid_Strain(i)*10^3-
0.001,num2str(Solid_Mesh(i)),'fontsize',20,'FontName','Times New Roman')
end

axis([var(1) 170000 var(3)-0.001 var(4)])

ax = gca;
ax.FontName = 'Times New Roman';
ax.FontSize = 20;
ax.LineWidth = 2;
% ax.XTick = [-50,-40,-30,-20,-10,0,10,20];

xlabel('Element Count','FontName','Times New
Roman','FontSize',28,'Interpreter','Latex')
ylabel('Strain ( $\varepsilon$ )','FontName','Times New
Roman','FontSize',28,'Interpreter','Latex')
legend('Notch Solid','location','northeast','FontName','Times New
Roman','FontSize',16,'Interpreter','Latex')
grid

```

3. X-ray thickness extraction

```

% Function to smooth and differentiate measured displacements in two dimensions
%
%
% Date: 17/08/2023
%
% Parameters:
%
%
% Updates:
%

clc
close all
clear all

% User Input
answer = inputdlg({'Test Name','Mesh Size in mm','FEA Model Length in mm','Thickness of
reduced section in mm'},'User input data')
Test = answer{1};
Mesh = str2num(answer{2});
Model = str2num(answer{3});
dip = str2num(answer{4});

Model = 400;

% Selected trf file. Make sure that the

```

```

[file path] = uigetfile('*.');
filename = fullfile(path,file);
fprintf(file)
fprintf('\n')

% Extract the data in stucture
info = dicominfo(filename);
data = double(dicomread(filename));
dicomdisp(filename)

figure
surf(data)
view(2)
shading interp
colormap('gray')
axis equal

%% Select the brightest Location
uiwait(msgbox('Select the brightest location'))
aval = ginput(1); % select 4 points on the figure
caxis([0 data(ceil(aval(2)),ceil(aval(1)))*1.1]);

%% Select Location with No specimen
% Select the 4 point with nothing in it
% uiwait(msgbox('Click 4 in a square with nothing in it'))
% val = ginput(4); % select 4 points on the figure
% val = sort(val); % sort the data
% xmin = ceil(max(val(1:2,1))); % determine the boundaries of selection
% ymin = ceil(max(val(1:2,2)));
% xmax = floor(min(val(3:4,1)));
% ymax = floor(min(val(3:4,2)));
%
% bias = mean(mean(data(ymin:ymax,xmin:xmax))');
% data = data - bias;
%
% surf(data)
% view(2)
% shading interp
% colormap('gray')
% axis equal
% caxis([0 data(ceil(aval(2)),ceil(aval(1)))*1.1]);

%% Image Rotation
% Select 2 points along the length of the beam in the figure
uiwait(msgbox('Image Rotation: Click 2 points along the edge of the specimen of interest'))
val = ginput(2); % select 2 points on the figure
val = sort(val); % sort the data

angle = atan2d(val(2,2)-val(1,2),val(2,1)-val(1,1));
data_rot = imrotate(data,angle);

surf(data_rot/1000)
view(2)
shading interp
colormap('gray')
axis equal
ax = gca;
ax.FontName = 'Times New Roman';
ax.FontSize = 20;

```

```

ax.LineWidth = 2;
xlabel('X position (pixels)')
ylabel('Y position (pixels)')
h = colorbar;
h.Label.String = "Contrast Value ( $\times 10^3$ )";
h.Label.Rotation = 270;
h.Label.VerticalAlignment = "bottom";
h.Label.FontSize = 20;
h.Label.Interpreter = 'latex';
caxis([0 data(ceil(aval(2)),ceil(aval(1)))*1.1]/1000);

Name = [Test, '_Contrast_Image_Rotated.png'];
exportgraphics(gcf,Name, 'Resolution',300);

%% Select Location of Interest
% Select the 4 corners of the beam in the figure to define an area where the
% phase of the specimen is consistent
uiwait(msgbox('Click 4 points that defines an area of interest of the beam'))
val = ginput(4);           % select 4 points on the figure
val = sort(val);          % sort the data
xmin = ceil(max(val(1:2,1))); % determine the boundaries of selection
ymin = ceil(max(val(1:2,2)));
xmax = floor(min(val(3:4,1)));
ymax = floor(min(val(3:4,2)));

data_int = data_rot(ymin:ymax,xmin:xmax);

dy = 40/(ymax-ymin);
x = [0:size(data_int,2)-1]*dy;
y = [0:size(data_int,1)-1]*dy;;

surf(x,y,data_int)
view(2)
shading interp
colormap('gray')
axis equal
xlabel('X position (mm)')
ylabel('Y position (mm)')

figure
plot(x,data_rot(ceil((ymax+ymin)/2),xmin:xmax))
xlabel('X position (mm)')
ylabel('Y position (mm)')

%% Average the data over the mesh size

Nx = floor(x(end))+1
Ny = floor(y(end))+1

for i = 1:Nx-1
    for j = 1:Ny-1
        element(j,i) = mean(data_int(find(y >= j-1 & y <= j),find(x >= i-1 & x <=
i)), 'all');
    end
end

Nodes = zeros(Ny,Nx);

% Corners
Nodes([1 1 Ny Ny],[1 Nx Ny 1]) = element([1 1 Ny-1 Ny-1],[1 Nx-1 Nx-1 1]);

% Edges

```

```

for i = 2:Nx-1
    Nodes(1,i) = mean([element(1,i) element(1,i-1)],"all");
    Nodes(Ny,i) = mean([element(Ny-1,i) element(Ny-1,i-1)],"all");
end
for j = 2:Ny-1
    Nodes(j,1) = mean([element(j,1) element(j-1,1)],"all");
    Nodes(j,Nx) = mean([element(j,Nx-1) element(j-1,Nx-1)],"all");
end

%Centre
for i = 2:Nx-1
    for j = 2:Ny-1
        Nodes(j,i) = mean([element(j,i) element(j-1,i) element(j,i-1) element(j-1,i-1)],"all");
    end
end

x_Nodes = [0:Nx-1];
y_Nodes = [0:Ny-1] - 20;

figure
plot(x_Nodes,Nodes(ceil(Ny/2),:))
title('x-ray pixel contrast - centreline')
xlabel('X position (mm)')
ylabel('Contract Value')

figure
surf(Nodes)
view(2)
shading interp
colormap('gray')
axis equal
xlabel('X position (pixels)')
ylabel('Y position (pixels)')

%% Smoothing the Data

% data_SG = SG_2D(data_int,0,0,20,3,1,1);
%
% figure
% plot(x,data_SG(ceil(size(data_SG,1)/2),:))
% xlabel('X position (mm)')
% ylabel('Y position (mm)')
%
% figure
% surf(data_SG)
% view(2)
% shading interp
% colormap('gray')
% axis equal
% xlabel('X position (mm)')
% ylabel('Y position (mm)')

%% Select Area of constant thickness

% Select the 4 corners of the beam that define the constant thickness
uiwait(msgbox('Click 4 points that defines an area of constant material properties'))
val = ginput(4); % select 4 points on the figure
val = sort(val); % sort the data
xmin = ceil(min(val(1:2,2))); % determine the boundaries of selection

```

```

ymin = ceil(max(val(1:2,2)));
xmax = floor(min(val(3:4,1)));
ymax = floor(min(val(3:4,2)));

%% Calculating Coefficients

z6mm = mean(mean(Nodes(ymin:ymax,xmin:xmax))')
z4mm = min(Nodes(ceil(size(Nodes,1)/2),:))

I0 = info.ExposureInuAs;
syms a_val b_val
equ = [I0-z6mm == I0 * exp(a_val*6+b_val*sqrt(6)),I0-z4mm == I0 *
exp(a_val*dip+b_val*sqrt(dip))];
S = solve(equ, [a_val b_val]);

a = double(S.a_val)
b = double(S.b_val)

% a = -0.1568
% b = 0.2403

%% Correct X-ray Contract Intensity with Thickness

% a = -0.1918;
% b = 0.3167;

% ----- Incorrect I = I_0 * exp(-mu * z) ----- %
% dz = 6/mean(mean(data_SG(ymin:ymax,xmin:xmax))')
% data_z = data_SG*dz;

uiwait(msgbox('Start Thickness Solving'));

syms z_var

% SG_max = max(Nodes,[],'all')
% SG_min = min(Nodes,[],'all')

data_z = zeros(size(Nodes));

for i = 1:size(Nodes,1)
    disp(i)
    for j = 1:size(Nodes,2)
        equ = a*z_var+b*sqrt(z_var)-log((I0-(Nodes(i,j)+i-1))/I0)==0;
        S = max(double(vpasolve(equ,z_var,5)));
        data_z(i,j) = S;
    end
end

% ----- %

% index = find(data_z(ceil(Ny/2),:) < 6);
% align = 200 - (x_Nodes(index(1)) + x_Nodes(index(end)))/2

figure
plot(x_Nodes,data_z(ceil(Ny/2),:))
grid

uiwait(msgbox('Click 2 points that defines the edges of the depression at 6 mm depth'))
val = ginput(2); % select 4 points on the figure

align = 200 - round((x_Nodes(round(val(1,1))) + x_Nodes(round(val(2,1))))/2)

```

```

x_Nodes_r = x_Nodes + align

%%

figure
surf(x_Nodes_r,y_Nodes,data_z)

view(2)
shading interp
colormap('jet')
axis equal
ax = gca;
ax.FontName = 'Times New Roman';
ax.FontSize = 20;
ax.LineWidth = 2;
xlabel('X position (mm)')
ylabel('Y position (mm)')
h = colorbar;
h.Label.String = "Thickness (mm)";
h.Label.Rotation = 270;
h.Label.VerticalAlignment = "bottom";
h.Label.FontSize = 20;

Name = [Test, '_Thickness.png']
exportgraphics(gcf,Name, 'Resolution',300)

figure
plot(x_Nodes,data_z(ceil(Ny/2),:))
title('X-ray Geometry')
xlabel('X position (mm)')
ylabel('Thickness (mm)')

%% Remove Data that overestimate thickness

data_z_r = data_z;
data_z_r(find(data_z_r > 6)) = 6;

figure
surf(x_Nodes,y_Nodes,data_z_r)
view(2)
shading interp
colormap('jet')
axis equal
title('X-ray Geometry > 6mm removed')
xlabel('X position (mm)')
ylabel('Y position (mm)')
colorbar

figure
plot(x_Nodes,data_z_r(ceil(Ny/2),:),'LineWidth', 3)
title('X-ray Geometry > 6mm removed')
xlabel('X position (mm)')
ylabel('Thickness (mm)')

%% Comparison

clear z_Geo variable

span = Model

```

```

x_Geo = 0:0.5:span;
clear z_Geo

list = {'Notch', 'Corrosion'};
[indx,tf] = listdlg('ListString',list,'SelectionMode','single');

% Actual Notch Geometry
if indx == 1

    y_Geo = -20:0.5:20;

    depth = 2;
    radius = 225;
    width = 2*sqrt(2*radius*depth - depth^2);

    for i = 1:length(x_Geo)

        if (x_Geo(i) > span/2-width/2 & x_Geo(i) < span/2+width/2)
            z_Geo(i) = 6 -depth + radius - sqrt(radius^2-(x_Geo(i)-span/2)^2);
        else
            z_Geo(i) = 6;
        end
    end

    for j = 1:length(y_Geo)
        variable(j,:) = z_Geo;
    end
    z_Geo = variable;

% Actual Corrossion Geometry
elseif indx == 2

    y_Geo = [0:0.5:20];

    depth = 3;      % depth of corrosion
    radius = 12.5;  % radius of curvature of fillet
    dip = 8.75      % diameter of dipped section
    diameter = 2*sqrt(2*radius*depth - depth^2) + dip % total diameter of corrosion
    section

    for i = 1:length(x_Geo)
        for j = 1:length(y_Geo)

            if sqrt((x_Geo(i) - span/2)^2 + y_Geo(j)^2) < diameter/2 & sqrt((x_Geo(i) -
span/2)^2 + y_Geo(j)^2) >= dip/2
                r = sqrt((x_Geo(i) - span/2)^2 + y_Geo(j)^2) - dip/2;
                z_Geo(j,i) = 6 - depth + radius - sqrt(radius^2-r^2);
            elseif sqrt((x_Geo(i) - span/2)^2 + y_Geo(j)^2) < dip/2
                z_Geo(j,i) = 3;
            else
                z_Geo(j,i) = 6;
            end
        end
    end
    y_Geo = [-20:0.5:20];
    z_Geo = [flipud(z_Geo);z_Geo(2:end,:)]
end

figure
plot(x_Geo,z_Geo(floor(length(y_Geo)/2),:),'Linewidth', 3); hold on
plot(x_Nodes_r, data_z(ceil(Ny/2),:),'Linewidth', 3)

```

```

legend('Actual geometry','X-ray Geometry','location','southeast')
val = axis
% axis([val(1) val(2) round(min(data_z(ceil(Ny/2),:))-2)
round(max(data_z(ceil(Ny/2),:))+1)])
axis([150 250 round(min(data_z(ceil(Ny/2),:))-2) round(max(data_z(ceil(Ny/2),:))+1)])
ax = gca;
ax.FontName = 'Times New Roman';
ax.FontSize = 20;
ax.LineWidth = 2;
xlabel('X Position (mm)')
ylabel('Thickness (mm)')

Name = [Test, '_Comp_Centreline.png']
exportgraphics(gcf,Name,'Resolution',300)

%% Error Plot

for i = 1:Nx
    for j = 1:Ny
        act = z_Geo(find(y_Geo == y_Nodes(j)),find(x_Geo == x_Nodes_r(i)));
        Error(j,i) = (data_z(j,i)-act)/act*100;
    end
end

figure
surf(x_Nodes_r,y_Nodes,Error)

view(2)
shading interp
colormap('jet')
axis equal
ax = gca;
ax.FontName = 'Times New Roman';
ax.FontSize = 20;
ax.LineWidth = 2;
xlabel('X position (mm)')
ylabel('Y position (mm)')
h = colorbar;
h.Label.String = "Thickness Error (%)";
h.Label.Rotation = 270;
h.Label.VerticalAlignment = "bottom";
h.Label.FontSize = 20;

Name = [Test, '_Error.png']
exportgraphics(gcf,Name,'Resolution',300)

%% Geometry Export

x_Export = [0 x_Nodes_r Model];
data_z_Export = [ones(Ny,1)*6 data_z_r ones(Ny,1)*6];

fileID = fopen('Geometry.csv','w');
k=1;
for i = 1:Nx+2
    for j=1:Ny
        fprintf(fileID, '%3.1f,%1.3f,%1.8f\r\n', x_Export(i), y_Nodes(j),
data_z_Export(j,i));
    end
end
fclose(fileID);

```


4. Results Comparison

```
%% Program to process DIC data files

clear all
close all
clc

%% Extract FEA data file

% Select any of the FEA data files
[FEAfilename,FEApath]=uigetfile('*.txt','Select an FEA Data File');

% Removes the file variable and extension
I = find(FEAfilename=='-');
FEAfile = strcat(FEApath,FEAfilename(1:I(end)));

% Extract in-plane strain on Outside Surface
opts = detectImportOptions(char(strcat(FEAfile, ' Shell.txt')));
opts.SelectedVariableNames = [2 3];
[FEA_Shell_x FEA_Shell_Strain] = readvars(char(strcat(FEAfile, ' Shell.txt')),opts);
if FEA_Shell_x(end)<1
    FEA_Shell_x=FEA_Shell_x*1000;
else
    FEA_Shell_x=FEA_Shell_x
end

opts = detectImportOptions(char(strcat(FEAfile, ' Solid.txt')));
opts.SelectedVariableNames = [2 3];
[FEA_Solid_x FEA_Solid_Strain] = readvars(char(strcat(FEAfile, ' Solid.txt')),opts);
if FEA_Solid_x(end)<1
    FEA_Solid_x=FEA_Solid_x*1000;
else
    FEA_Solid_x=FEA_Solid_x
end

opts = detectImportOptions(char(strcat(FEAfile, ' Xray.txt')));
opts.SelectedVariableNames = [2 3];
[FEA_Xray_x FEA_Xray_Strain] = readvars(char(strcat(FEAfile, ' Xray.txt')),opts);
if FEA_Xray_x(end)<1
    FEA_Xray_x=FEA_Xray_x*1000;
else
    FEA_Xray_x=FEA_Xray_x
end

%% Checking the FEA Extracted Data

% Strain along centreline
figure
plot(FEA_Shell_x,FEA_Shell_Strain); hold on;
plot(FEA_Xray_x,FEA_Xray_Strain); hold on;
plot(FEA_Solid_x,FEA_Solid_Strain); hold on;
legend('Shell','X-ray','Solid')
```

```

xlabel('Y position (mm)')
ylabel('Strain m/m')
title('FEA Strain Shell vs Solid')
grid

%% Extract DIC data files

[datafiles,datapath]=uigetfile('*.csv','Select Data File(s)','MultiSelect','on');
datafile = strcat(datapath,datafiles);

if iscell(datafile)
    nfiles = length(datafile);
    datafile = char(datafile);
    nfiles = size(datafile,2);
else
    nfiles = 1;
    datafile = [datafile;datafile];
end
display(nfiles)

Data.Load = [];
VariableNames = {'X', 'Y', 'Z', 'U', 'V', 'W', 'sigma', 'x', 'y'};

for k = 1:nfiles
    tic;
    opts = detectImportOptions(datafile(k,:));
    for i = 1:length(VariableNames)
        VariableNumbers(i) = find(strcmp(opts.VariableNames,VariableNames{i}));
    end
    opts.SelectedVariableNames = VariableNumbers;
    [X Y Z U V W sigma x y] = readvars(datafile(k,:),opts);

    px = x(2)-x(1);
    Sections = [0; find(isnan(x)); length(x)+1];

    for j = 1:length(Sections)-1
        clear x_m y_m X_m Y_m Z_m YZ_R_m YZ_T_m U_m V_m W_m V_c W_c R_m T_m

        for i = Sections(j)+1:Sections(j+1)-1

            NxMin = min(x(Sections(j)+1:Sections(j+1)-1));
            NyMin = min(y(Sections(j)+1:Sections(j+1)-1));

            NxMax = max(x(Sections(j)+1:Sections(j+1)-1));
            NyMax = max(y(Sections(j)+1:Sections(j+1)-1));

            xval = (x(i)-NxMin)/px+1;
            yval = (y(i)-NyMin)/px+1;
            if (floor(xval)~=xval)
                break
            end
            x_m(xval) = x(i);
            y_m(yval) = y(i);
            if(sigma(i) ~= -1 & ~isnan(sigma(i)))
                % X_m(xval) = X(i);
                % Y_m(yval) = Y(i);
                X_m(yval,xval) = X(i);
                Y_m(yval,xval) = Y(i);
                Z_m(yval,xval) = Z(i);
            end
        end
    end
end

```

```

        YZ_R_m(yval,xval) = sqrt(Z(i)^2 + Y(i)^2);
        YZ_T_m(yval,xval) = atan2(Z(i),Y(i));
        U_m(yval,xval) = U(i);
        V_m(yval,xval) = V(i);
        W_m(yval,xval) = W(i);
        R_m(yval,xval) = sqrt(V(i)^2 + W(i)^2);
        T_m(yval,xval) = atan2(W(i),V(i));
    else
        %           X_m(xval) = NaN;
        %           Y_m(yval) = NaN;
        X_m(yval,xval) = NaN;
        Y_m(yval,xval) = NaN;
        Z_m(yval,xval) = NaN;
        YZ_R_m(yval,xval) = NaN;
        YZ_T_m(yval,xval) = NaN;
        U_m(yval,xval) = NaN;
        V_m(yval,xval) = NaN;
        W_m(yval,xval) = NaN;
        R_m(yval,xval) = NaN;
        T_m(yval,xval) = NaN;
    end
    Data.Load(k).Section(j).X_m = X_m;
    Data.Load(k).Section(j).Y_m = Y_m;
    Data.Load(k).Section(j).Z_m = Z_m;
    Data.Load(k).Section(j).YZ_R_m = YZ_R_m;
    Data.Load(k).Section(j).YZ_T_m = YZ_T_m;
    Data.Load(k).Section(j).V_m = V_m;
    Data.Load(k).Section(j).W_m = W_m;
    Data.Load(k).Section(j).R_m = R_m;
    Data.Load(k).Section(j).T_m = T_m;

end
end

    display(['file ',num2str(k),' of ',num2str(nfiles),' complete (' ,
num2str(round(toc,1)), ' sec']])

end

figure
set(gcf,'Visible','on')
for j = 1:length(Data.Load(1).Section)
    subplot(length(Data.Load(1).Section),1,j)
    surf(Data.Load(k).Section(j).X_m, ...
        Data.Load(k).Section(j).Y_m, ...
        Data.Load(k).Section(j).Z_m, ...
        'EdgeColor','none'); hold on
    title(['section ',num2str(j)])
end

prompt = {'Select section number that contains the data'};
dlg_title = 'Select section number';
num_lines = 1;
answer = inputdlg(prompt,dlg_title,num_lines);
secNumber = str2num(answer{1});

%% SG Parameters

var = find(Data.Load(k).Section(secNumber).X_m(10,:)>0);
pt = var(1);
var_x = find(Data.Load(k).Section(secNumber).Y_m(:,10)<0);

```

```

pt_x = var_x(1);

k = nfiles; % file to use
m = 30; % filter length = 2m+1
n = 3; % order of polynomial
dy = nanmean(Data.Load(k).Section(secNumber).Y_m(1:end-1,pt)'-
Data.Load(k).Section(secNumber).Y_m(2:end,pt)');
dx = nanmean(Data.Load(k).Section(secNumber).X_m(pt_x,2:end)'-
Data.Load(k).Section(secNumber).X_m(pt_x,1:end-1)');

```

```

%% Position Surface Plot

```

```

k = 1;

figure
for j = 1:length(Data.Load(1).Section)
    surf(Data.Load(k).Section(j).X_m, ...
        Data.Load(k).Section(j).Y_m, ...
        Data.Load(k).Section(j).Z_m, ...
        'EdgeColor','none'); hold on
end
hold off
colorbar
colormap jet

    view(0,90)
    val = axis;
    valy = val(4)-val(3);
    valx = (valy - (val(2)-val(1)))/2;
    axis([val(1)-valx val(2)+valx val(3) val(4)]);

xlabel('X position')
ylabel('Y Position')
title('Z Position Surface Plot')

```

```

%% W Deformation Surface Plot

```

```

h1 = figure;

k = nfiles;

for j = 1:length(Data.Load(k).Section)
    surf(Data.Load(k).Section(j).X_m, ...
        Data.Load(k).Section(j).Y_m, ...
        Data.Load(k).Section(j).V_m, ...
        'EdgeColor','none'); hold on
end

colorbar
colormap jet

view(0,90)
val = axis;
valy = val(4)-val(3);
valx = (valy - (val(2)-val(1)))/2;
axis([val(1)-valx val(2)+valx val(3) val(4)]);
hold off

xlabel('X position')

```

```

ylabel('Y Position')
title('Deformation Surface Plot')

% uiwait(msgbox('Click centre location of test specimen','Image
Calibration','CreateMode','modal'))
% [xi,yi,but] = ginput(1);
%
% for k = 1:nfiles
%     for j = 1:length(Data.Load(k).Section)
%         Data.Load(k).Section(j).X_m = Data.Load(k).Section(j).X_m - xi;
%         Data.Load(k).Section(j).Y_m = Data.Load(k).Section(j).Y_m - yi;
%     end
% end
%
% figure(h1)

%% Deformation Line Plot

figure
for k = 1:nfiles
    Yvar = [Data.Load(k).Section(secNumber).Y_m(:,pt)']';
    Wvar = [Data.Load(k).Section(secNumber).W_m(:,pt)']';
    plot(Yvar,Wvar)
    hold on
end
title('Out of Plane Deformation')
xlabel('Y position')
ylabel('W Deflection')
title('W Deflection vs Y Position')

Yvar = [Data.Load(k).Section(secNumber).Y_m(:,pt)']';
Vvar = [Data.Load(k).Section(secNumber).V_m(:,pt)']';

figure
plot(Yvar,Vvar); hold on
xlabel('Y position')
ylabel('V Deflection')
title('V Deflection vs Y Position')

%% W Deformation Surface Plot

figure
k = nfiles;

for j = 1:length(Data.Load(k).Section)
    contourf(Data.Load(k).Section(j).X_m, ...
        Data.Load(k).Section(j).Y_m, ...
        Data.Load(k).Section(j).W_m,8, ...
        'EdgeColor','none'); hold on
end

view(2)
shading interp
colormap('jet')
axis equal
ax = gca;
ax.FontName = 'Times New Roman';

```

```

ax.FontSize = 20;
ax.LineWidth = 2;
% title('W Deformation')
xlabel('X position (mm)')
ylabel('Y position (mm)')
h = colorbar;
h.Label.Interpreter = 'latex';
h.Label.String = "W Deformation (mm)";
h.Label.Rotation = 270;
h.Label.VerticalAlignment = "bottom";
h.Label.FontSize = 20;

axis([-40 40 -40 40]);    % 1.5 Shear
grid

figure
k = nfiles;

for j = 1:length(Data.Load(k).Section)
    contourf(Data.Load(k).Section(j).X_m, ...
            Data.Load(k).Section(j).Y_m, ...
            Data.Load(k).Section(j).V_m,8, ...
            'EdgeColor','none'); hold on
end

view(2)
shading interp
colormap('jet')
axis equal
ax = gca;
ax.FontName = 'Times New Roman';
ax.FontSize = 20;
ax.LineWidth = 2;
% title('V Deformation')
xlabel('X position (mm)')
ylabel('Y position (mm)')
h = colorbar;
h.Label.Interpreter = 'latex';
h.Label.String = "V Deformation (mm)";
h.Label.Rotation = 270;
h.Label.VerticalAlignment = "bottom";
h.Label.FontSize = 20;

axis([-40 40 -40 40]);    % 1.5 Shear
grid

%% Deformation Plot

Yvar = [Data.Load(k).Section(secNumber).Y_m(:,pt)']';
Vvar = [Data.Load(k).Section(secNumber).V_m(:,pt)']';
Wvar = [Data.Load(k).Section(secNumber).W_m(:,pt)']';

figure

plot(Yvar,Vvar,'LineWidth',4); hold on
plot(Yvar,Wvar,'LineWidth',4);

axis([-40 40 -1 4]);    % 1.5 Shear

```

```

ax = gca;
ax.FontName = 'Times New Roman';
ax.FontSize = 20;
ax.LineWidth = 2;
% ax.XTick = [-50,-40,-30,-20,-10,0,10,20];

xlabel('Position (mm)','FontName','Times New
Roman','FontSize',28,'Interpreter','Latex')
ylabel('Deformation (mm)','FontName','Times New
Roman','FontSize',28,'Interpreter','Latex')
legend('DIC $u$', 'DIC $w$', 'location', 'southeast', 'FontName', 'Times New
Roman', 'FontSize', 16, 'Interpreter', 'Latex')
grid

set(gcf, 'Visible', 'on')

Name = [FEAfilename(19:end-4), '_Deformation.png']
exportgraphics(gcf,Name, 'Resolution', 300)

%% Surface Strain
%
% Data.Load(k).Section(secNumber).S_range =
find(~isnan(Data.Load(k).Section(secNumber).W_m(:,1)));
% Data.Load(k).Section(secNumber).S_X_e =
Data.Load(k).Section(secNumber).X_m(ceil(size(Data.Load(k).Section(secNumber).X_m,2)/2)
,:);
% Data.Load(k).Section(secNumber).S_Y_e =
Data.Load(k).Section(secNumber).Y_m(Data.Load(k).Section(secNumber).S_range,pt)';
%
%
% for k = 1:nfiles
%     Data.Load(k).Section(secNumber).S_e_T = -
SG_2D(Data.Load(k).Section(secNumber).V_m',0,1,m,n,dx,dy)'...
%
%     +
0.5*((SG_2D(Data.Load(k).Section(secNumber).W_m',0,1,m,n,dx,dy).^2)');
%     Data.Load(k).Section(secNumber).S_e_B = -
0.006/2*SG_2D(Data.Load(k).Section(secNumber).W_m',0,2,m,n,dx,dy)';
%     Data.Load(k).Section(secNumber).S_e_Y = Data.Load(k).Section(secNumber).S_e_T -
Data.Load(k).Section(secNumber).S_e_B;
% end
%
%
% figure
% k = nfiles;
% surf(Data.Load(k).Section(secNumber).S_X_e, ...
%     Data.Load(k).Section(secNumber).S_Y_e, ...
%     Data.Load(k).Section(j).S_e_T); hold on
%
% view(2)
% shading interp
% colormap('jet')
% axis equal
% ax = gca;
% ax.FontName = 'Times New Roman';
% ax.FontSize = 20;
% ax.LineWidth = 2;
% title('Y Strain')
% xlabel('X position (mm)')
% ylabel('Y position (mm)')
% h = colorbar;
% h.Label.Interpreter = 'latex';

```

```

% h.Label.String = "Strain ( $\varepsilon$ )";
% h.Label.Rotation = 270;
% h.Label.VerticalAlignment = "bottom";
% h.Label.FontSize = 20;

Data.Load(k).Section(secNumber).S_X_e =
Data.Load(k).Section(secNumber).X_m(ceil(size(Data.Load(k).Section(secNumber).X_m,2)/2)
,:);
Data.Load(k).Section(secNumber).S_Y_e = Data.Load(k).Section(secNumber).Y_m(:,pt)';

clear Data.Load(k).Section(secNumber).S_e_T Data.Load(k).Section(secNumber).S_e_B
Data.Load(k).Section(secNumber).S_e_Y

for l = 1:size(Data.Load(k).Section(secNumber).Y_m,2)
    for k = 1:nfiles
        Data.Load(k).Section(secNumber).S_range =
find(~isnan(Data.Load(k).Section(secNumber).W_m(:,1)));
% Data.Load(k).Section(secNumber).e_T = -
SG_1D(Data.Load(k).Section(secNumber).V_m(Data.Load(k).Section(secNumber).range,pt)',1,
m,n,dy)';

Data.Load(k).Section(secNumber).S_e_T(Data.Load(k).Section(secNumber).S_range,l) = -
SG_1D(Data.Load(k).Section(secNumber).V_m(Data.Load(k).Section(secNumber).S_range,l)',1
,m,n,dy)'. . .
+
0.5.*((SG_1D(Data.Load(k).Section(secNumber).W_m(Data.Load(k).Section(secNumber).S_ran
ge,l)',1,m,n,dy).^2)');

Data.Load(k).Section(secNumber).S_e_B(Data.Load(k).Section(secNumber).S_range,l) = -
0.006/2*SG_1D(Data.Load(k).Section(secNumber).W_m(Data.Load(k).Section(secNumber).S_ran
ge,l)',2,m,n,dy)';
    end
end

Data.Load(k).Section(secNumber).S_e_Y = Data.Load(k).Section(secNumber).S_e_T -
Data.Load(k).Section(secNumber).S_e_B;

figure
k = nfiles;
surf(Data.Load(k).Section(secNumber).S_X_e, ...
Data.Load(k).Section(secNumber).S_Y_e, ...
Data.Load(k).Section(j).S_e_T); hold on

view(2)
shading interp
colormap('jet')
axis equal
ax = gca;
ax.FontName = 'Times New Roman';
ax.FontSize = 20;
ax.LineWidth = 2;
% title('Y Strain')
xlabel('X position (mm)')
ylabel('Y position (mm)')
h = colorbar;
h.Label.Interpreter = 'latex';
h.Label.String = "Strain ( $\varepsilon$ )";
h.Label.Rotation = 270;
h.Label.VerticalAlignment = "bottom";

```



```

h.Label.FontSize = 20;

% Name = ['Strain.png'];
% exportgraphics(gcf,Name,'Resolution',300);

% figure
% k = nfiles;
% surf(Data.Load(k).Section(j).X_m, ...
%       Data.Load(k).Section(j).Y_m, ...
%       Data.Load(k).Section(j).S_e_Y); hold on
%
% view(2)
% shading interp
% colormap('jet')
% axis equal
% ax = gca;
% ax.FontName = 'Times New Roman';
% ax.FontSize = 20;
% ax.LineWidth = 2;
% title('Membrane Strain')
% xlabel('X position (mm)')
% ylabel('Y position (mm)')
% h = colorbar;
% h.Label.Interpreter = 'latex';
% h.Label.String = "Strain ( $\mu\text{varepsilon}$ )";
% h.Label.Rotation = 270;
% h.Label.VerticalAlignment = "bottom";
% h.Label.FontSize = 20;
%
% % Name = ['Strain.png'];
% % exportgraphics(gcf,Name,'Resolution',300);
%
%
% figure
% k = nfiles;
% surf(Data.Load(k).Section(j).X_m, ...
%       Data.Load(k).Section(j).Y_m, ...
%       Data.Load(k).Section(j).S_e_B); hold on
%
% view(2)
% shading interp
% colormap('jet')
% axis equal
% ax = gca;
% ax.FontName = 'Times New Roman';
% ax.FontSize = 20;
% ax.LineWidth = 2;
% title('Membrane Strain')
% xlabel('X position (mm)')
% ylabel('Y position (mm)')
% h = colorbar;
% h.Label.Interpreter = 'latex';
% h.Label.String = "Strain ( $\mu\text{varepsilon}$ )";
% h.Label.Rotation = 270;
% h.Label.VerticalAlignment = "bottom";
% h.Label.FontSize = 20;
%
% % Name = ['Strain.png'];
% % exportgraphics(gcf,Name,'Resolution',300);

```

```

%% Centreline Strain Calculations

clear Vvar Wvar

for k = 1:nfiles
    Data.Load(k).Section(secNumber).range =
    find(~isnan(Data.Load(k).Section(secNumber).W_m(:,pt)));
    Data.Load(k).Section(secNumber).Y_e =
    Data.Load(k).Section(secNumber).Y_m(Data.Load(k).Section(secNumber).range,pt)';
    % Data.Load(k).Section(secNumber).e_T = -
    SG_1D(Data.Load(k).Section(secNumber).V_m(Data.Load(k).Section(secNumber).range,pt)',1,
    m,n,dy)';
    Data.Load(k).Section(secNumber).e_T = -
    SG_1D(Data.Load(k).Section(secNumber).V_m(Data.Load(k).Section(secNumber).range,pt)',1,
    m,n,dy)'...
    +
    0.5.*((SG_1D(Data.Load(k).Section(secNumber).W_m(Data.Load(k).Section(secNumber).range,
    pt)',1,m,n,dy).^2)');
    Data.Load(k).Section(secNumber).e_B = -
    0.006/2*SG_1D(Data.Load(k).Section(secNumber).W_m(Data.Load(k).Section(secNumber).range
    ,pt)',2,m,n,dy)';
    Data.Load(k).Section(secNumber).e_Y = Data.Load(k).Section(secNumber).e_T -
    Data.Load(k).Section(secNumber).e_B;
end

Yvar = Data.Load(k).Section(secNumber).Y_e;
Wvar = Data.Load(k).Section(secNumber).e_B; % Bending
Vvar = Data.Load(k).Section(secNumber).e_Y; % Membrane
Tvar = Data.Load(k).Section(secNumber).e_T; % In-plane

figure
plot(Yvar,-
(SG_1D(Data.Load(k).Section(secNumber).W_m(Data.Load(k).Section(secNumber).range,pt)',1
,m,n,dy)))
var = axis
axis([-40 40 var(3) var(4)]);

figure

plot(FEA_Solid_x-200,FEA_Solid_Strain*10^3,'LineWidth', 2); hold on;
plot(FEA_Shell_x-200,FEA_Shell_Strain*10^3,'LineWidth', 2);
plot(FEA_Xray_x-200,FEA_Xray_Strain*10^3,'LineWidth', 2);
% plot(Yvar, Tvar*10^3,'LineWidth', 2);
plot(Yvar(m:end-m), Tvar(m:end-m)*10^3,'LineWidth', 2);

var = axis

axis([-40 40 var(3)-0.1 var(4)+0.8])

ax = gca;
ax.FontName = 'Times New Roman';
ax.FontSize = 20;
ax.LineWidth = 2;
% ax.XTick = [-50,-40,-30,-20,-10,0,10,20];

xlabel('Position (mm)','FontName','Times New
Roman','FontSize',28,'Interpreter','Latex')
ylabel('Strain ( $\varepsilon$ )','FontName','Times New
Roman','FontSize',28,'Interpreter','Latex')

```

```

legend('FEA Solid','FEA Shell','FEA X-ray
Shell','DIC','location','northeast','FontName','Times New
Roman','FontSize',16,'Interpreter','Latex')
grid

```

```

Name = [FEAfilename(19:end-4),' - Strain Graph.png']
exportgraphics(gcf,Name,'Resolution',300)

```

```

%% Bar Graph

```

```

% figure
% x = categorical({'Single-Shear','1.5 Single-Shear','Honeycomb'});
% x = reordercats(x,{'Single-Shear','1.5 Single-Shear','Honeycomb'});
% y = [0.551 0.550 0.510; 0.4250 0.427 0.399; 0.337 0.216 0.171];
% bar(x,y);
%
% ax = gca;
% ax.FontName = 'Times New Roman';
% ax.FontSize = 14;
% ax.LineWidth = 1;
% ax.YLim = [0 0.7];
%
%
% ylabel('Bending Factor','FontName','Times New Roman','FontSize',20)
% legend('DIC Strain','FEA Strain','FEA Stress','FontName','Times New
Roman','FontSize',16)
% grid;
%
% set(gcf,'Visible','on');
%

```

```

% Name = ['Bending_Factor.png'];
% exportgraphics(gcf,Name,'Resolution',300);
%
%
%

```

```

% figure
% x = categorical({'Single-Shear','1.5 Single-Shear','Honeycomb'});
% x = reordercats(x,{'Single-Shear','1.5 Single-Shear','Honeycomb'});
% y = [1.824 1.8226 1.8241; 0.440 0.438 0.399; 0.3100 0.216 0.1708];
% bar(x,y)
%
% ax = gca;
% ax.FontName = 'Times New Roman';
% ax.FontSize = 14;
% ax.LineWidth = 1;
% ax.YLim = [0 0.7];
%
%
% ylabel('Stress Concentration','FontName','Times New Roman','FontSize',20);
% legend('DIC Strain','FEA Strain','FEA Stress','FontName','Times New
Roman','FontSize',14);
% grid
%
% set(gcf,'Visible','on');
%
% Name = ['Stress Concentration.png'];
% exportgraphics(gcf,Name,'Resolution',300);

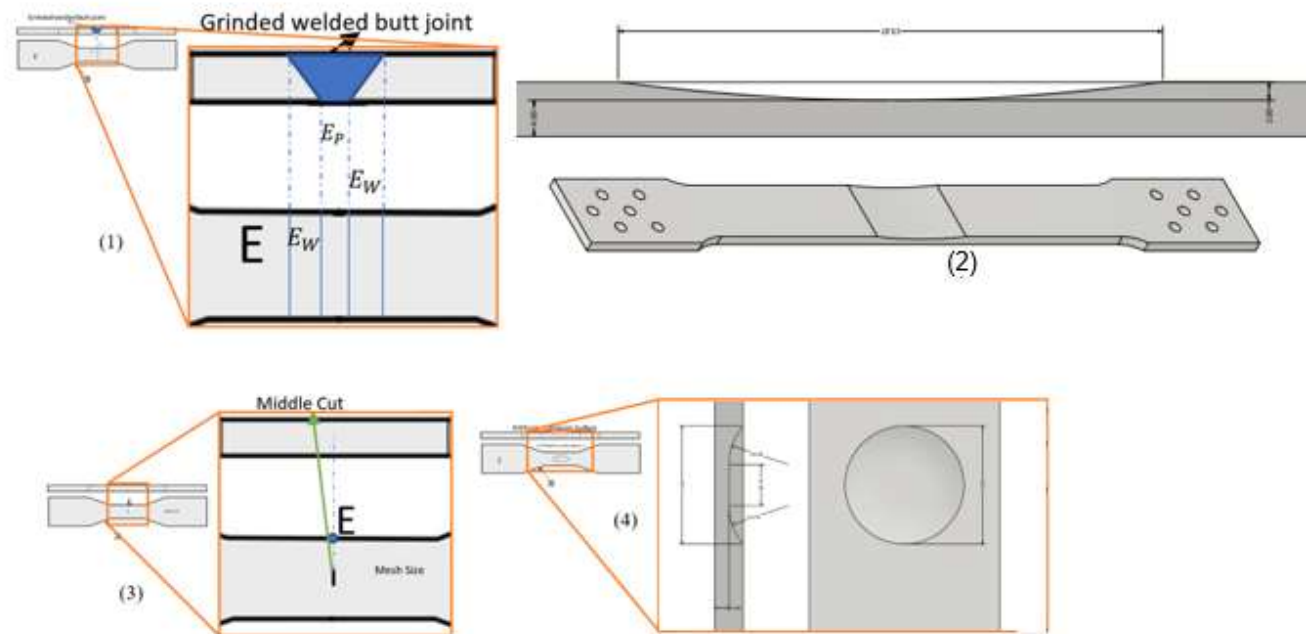
```

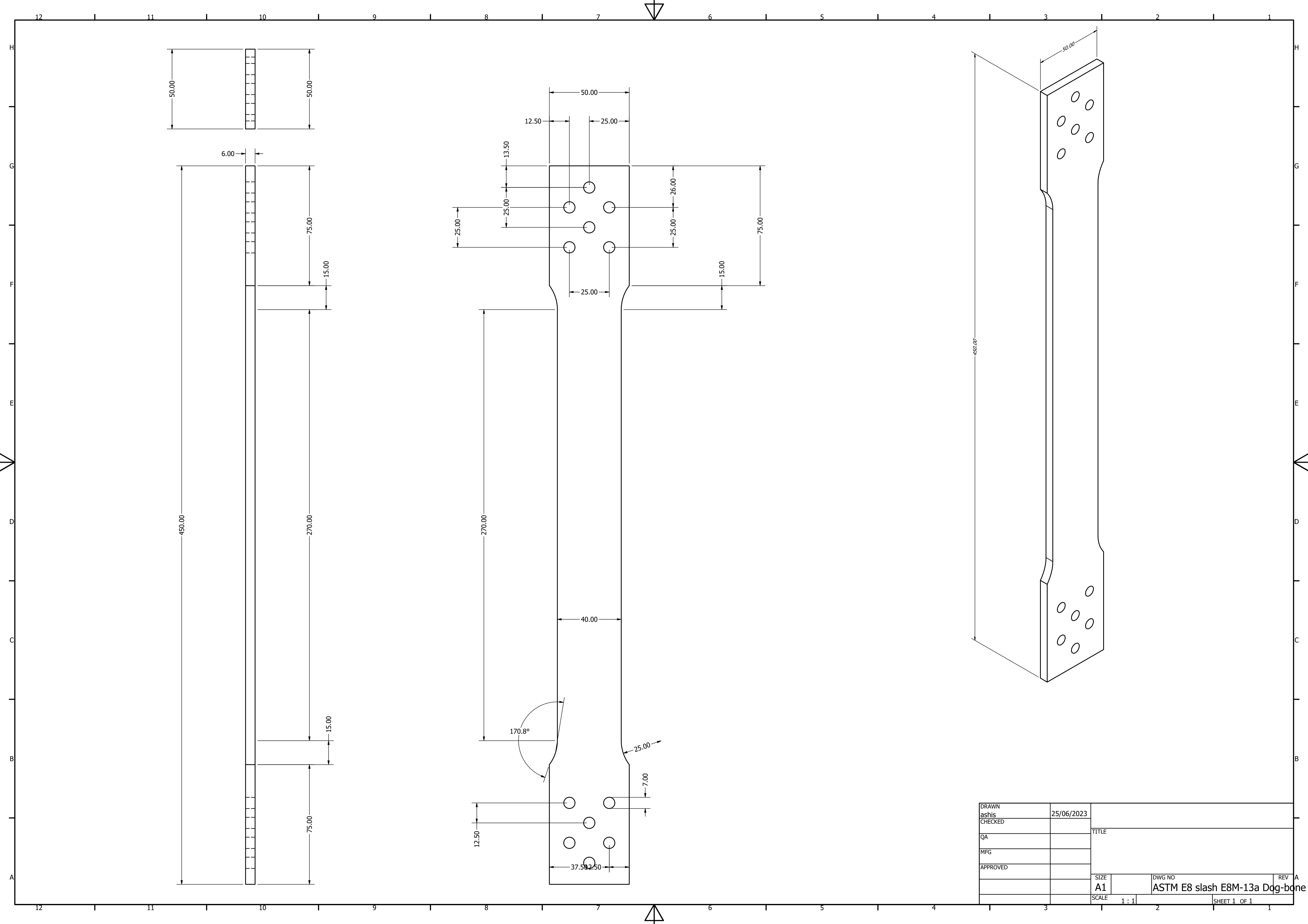
E. Specimens Details & Engineering Drawings

Different Specimens' Surfaces

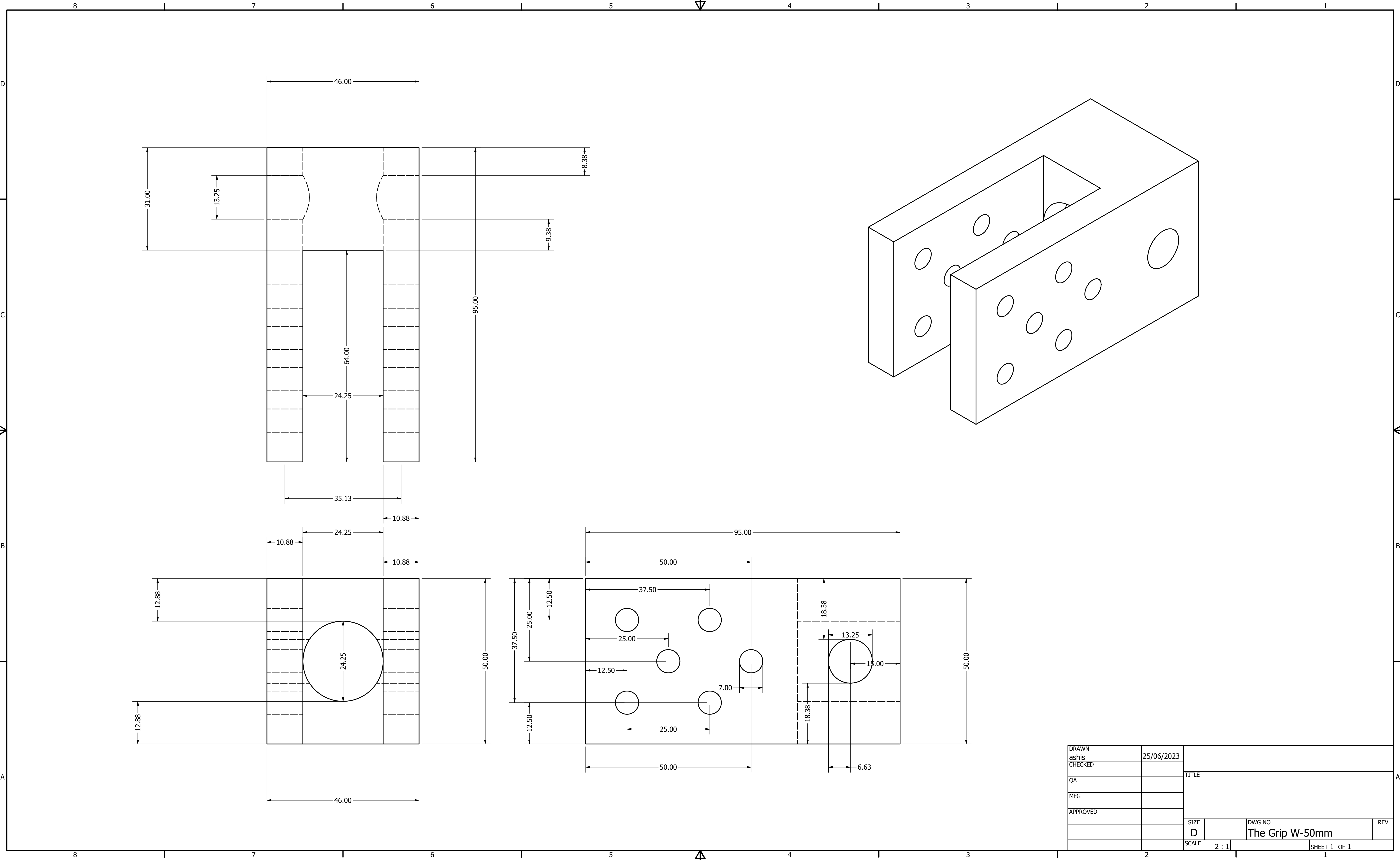
Four different types of Surfaces are:

- 1. Welded
- 2. Notched
- 3. Mild cut
- 4. Artificially corroded surface

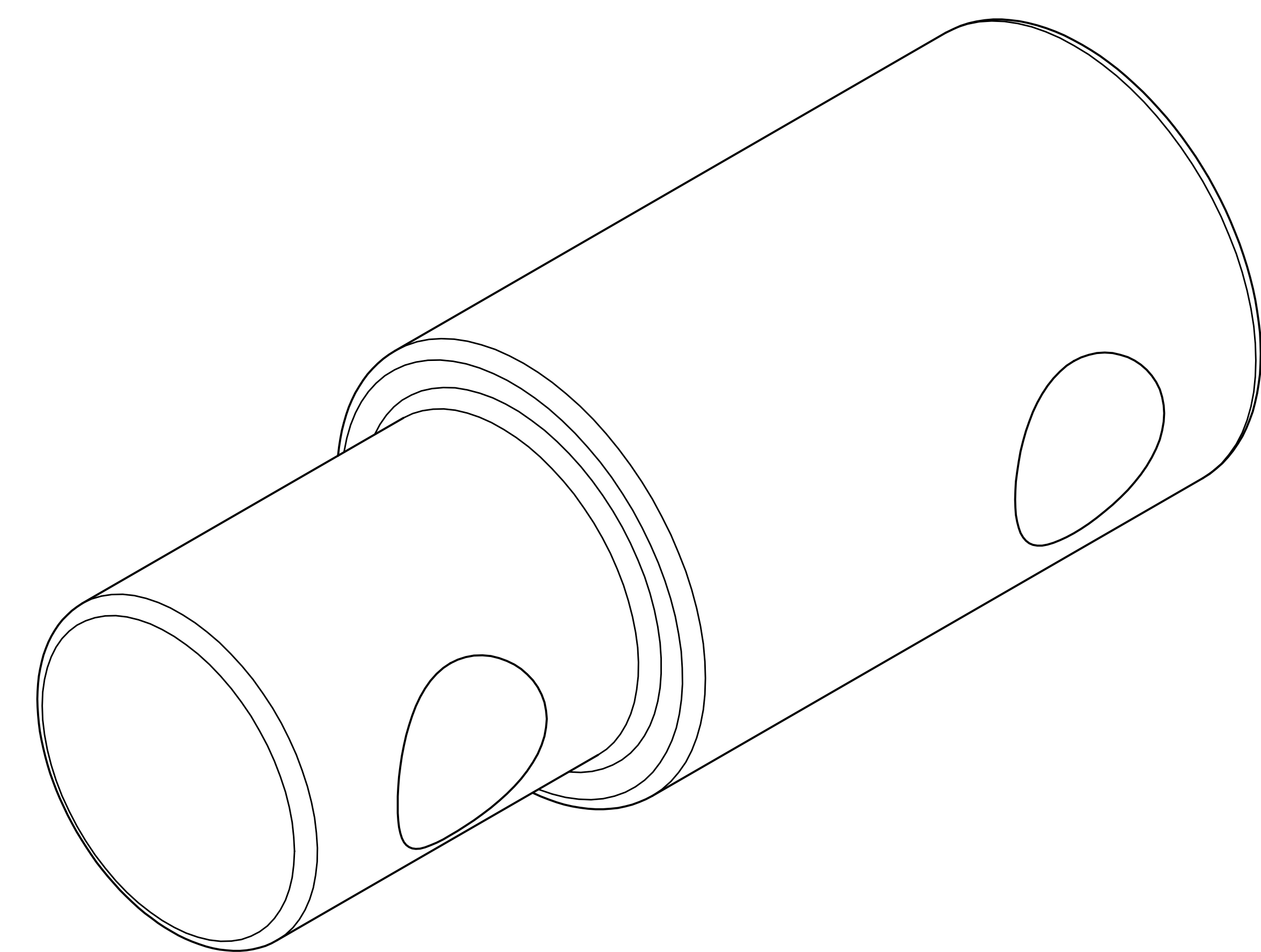
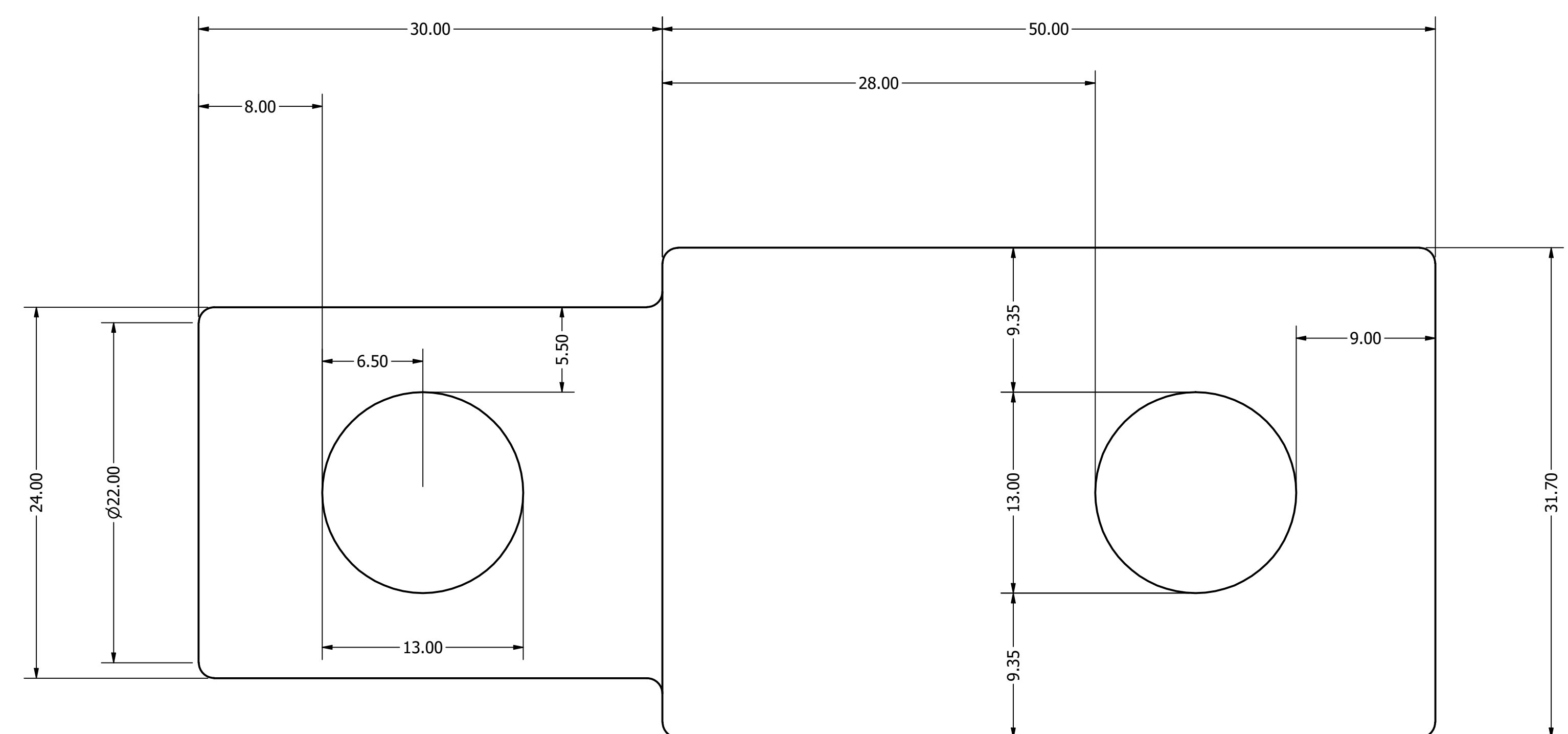
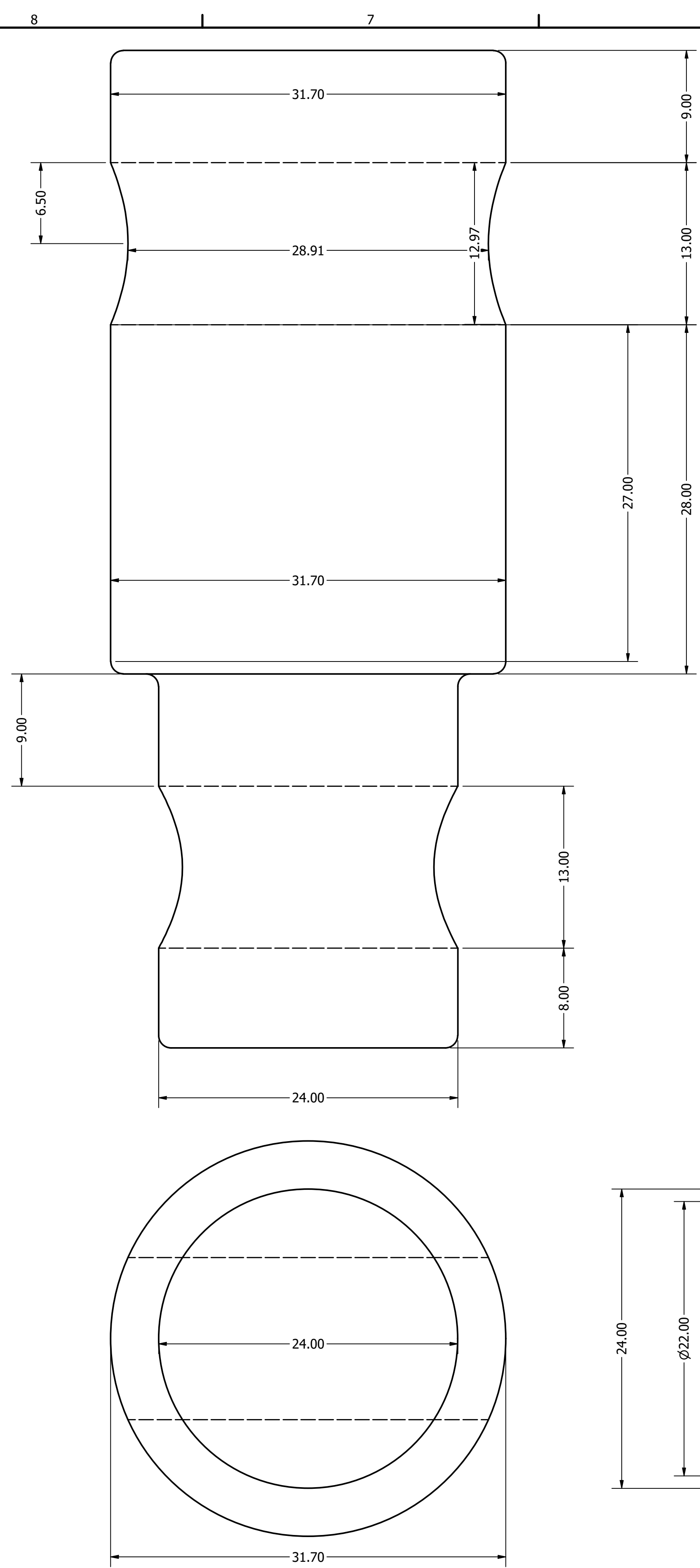




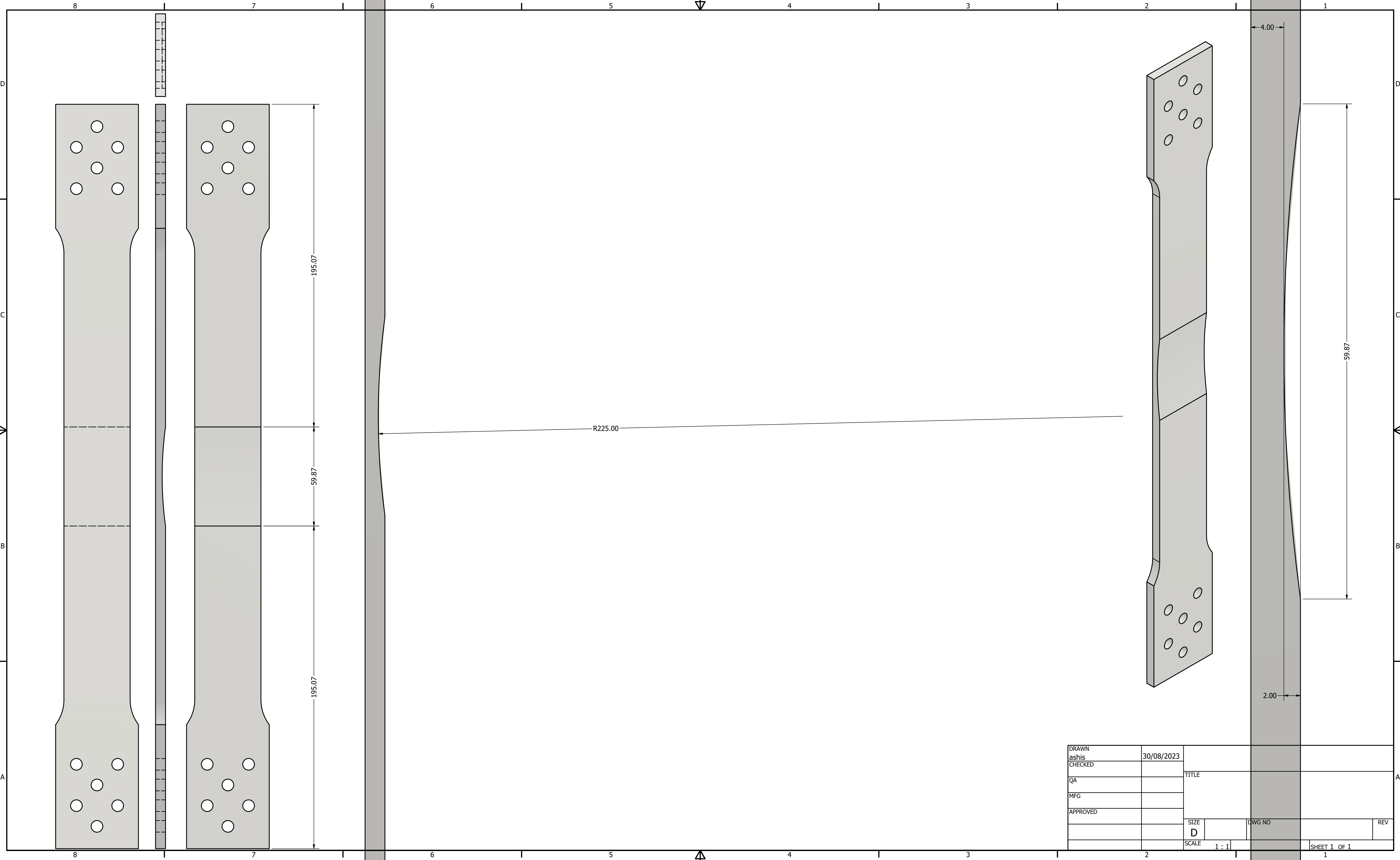
DRAWN	ashis		25/06/2023	
CHECKED				TITLE
QA				
MFG				
APPROVED				
	SIZE	DWG NO	REV A	
	A1	ASTM E8 slash E8M-13a Dog-bone 450		
	SCALE	1 : 1	SHEET 1 OF 1	



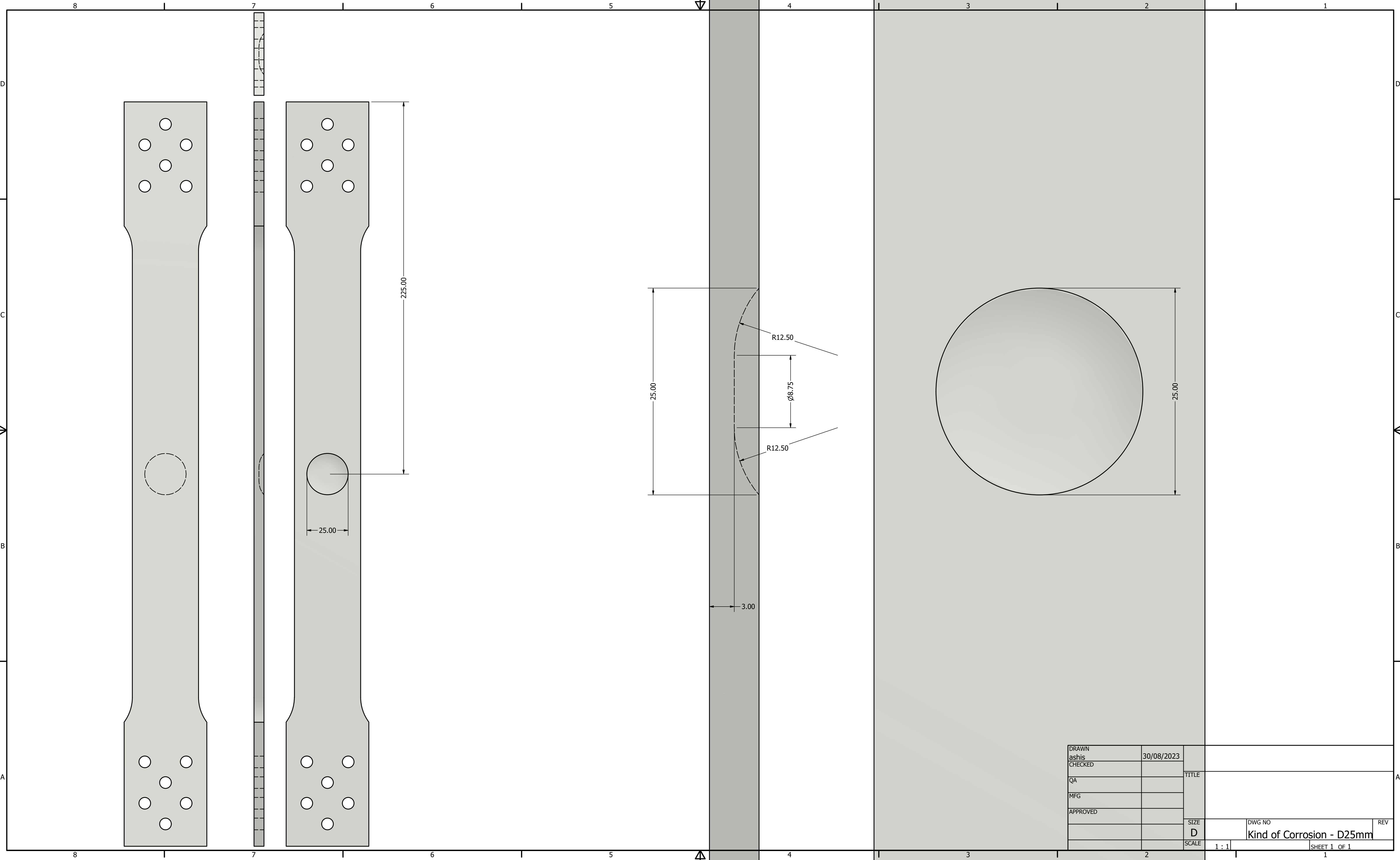
DRAWN	ashis	25/06/2023		
CHECKED			TITLE	
QA				
MFG				
APPROVED				
			SIZE	DWG NO
			D	The Grip W-50mm
			SCALE	REV
			2 : 1	
			SHEET 1 OF 1	



DRAWN	ashis	25/06/2023	TITLE		
CHECKED			TITLE		
QA			TITLE		
MFG			TITLE		
APPROVED			TITLE		
			SIZE	DWG NO	REV
			D		
			SCALE	SHEET 1 OF 1	
			4 : 1		



DRAWN	ashis	30/08/2023		
CHECKED			TITLE	
QA				
MFG				
APPROVED				
			SIZE	D
			SCALE	1 : 1
			DWG NO	
			REV	
			SHEET 1 OF 1	



DRAWN	ashis	30/08/2023		
CHECKED			TITLE	
QA				
MFG				
APPROVED				
			SIZE	D
			SCALE	1 : 1
			DWG NO	Kind of Corrosion - D25mm
			REV	
			SHEET 1 OF 1	